INFORMATION TO USERS

This manuscript has been reproduced from the microfilm master. UMI films the text directly from the original or copy submitted. Thus, some thesis and dissertation copies are in typewriter face, while others may be from any type of computer printer.

The quality of this reproduction is dependent upon the quality of the copy submitted. Broken or indistinct print, colored or poor quality illustrations and photographs, print bleedthrough, substandard margins, and improper alignment can adversely affect reproduction.

In the unlikely event that the author did not send UMI a complete manuscript and there are missing pages, these will be noted. Also, if unauthorized copyright material had to be removed, a note will indicate the deletion.

Oversize materials (e.g., maps, drawings, charts) are reproduced by sectioning the original, beginning at the upper left-hand corner and continuing from left to right in equal sections with small overlaps.

Photographs included in the original manuscript have been reproduced xerographically in this copy. Higher quality 6" x 9" black and white photographic prints are available for any photographs or illustrations appearing in this copy for an additional charge. Contact UMI directly to order.

ProQuest Information and Learning
300 North Zeeb Road, Ann Arbor, MI 48106-1346 USA
800-521-0600

CONDUCTION AND NON-CONDUCTION LIMITED LASER HEATING PROCESS- MATHEMATICAL SIMULATION.

BY

IFTEKHAR ZAHEER NAQAVI

A Thesis Presented to the

DEANSHIP OF GRADUATE STUDIES

KING FAHD UNIVERSITY OF PETROLEUM & MINERALS

DHAHRAN, SAUDI ARABIA

In Partial Fulfillment of the
Requirements for the Degree of

MASTER OF SCIENCE

In

MECHANICAL ENGINEERING

SHABAN 1422 H

NOVEMBER 2001

KING FAHD UNIVERSITY OF PETROLEUM AND MINERALS
DHAHRAN 31261, SAUDI ARABIA

DEANSHIP OF GRADUATE STUDIES

This Thesis, written by **IFTEKHAR ZAHEER NAQAVI** under the direction of his Thesis Advisor and approved by his Thesis Committee, has been presented to and accepted by the Dean, College of Graduate Studies, in partial fulfillment of the requirements for the degree of **MASTER OF SCIENCE IN MECHANICAL ENGINEERING** .

Thesis Committee

13 Jan 2002
Dr. Bekir Sami Yilbas (Chairman)

Dec 5/2001
Dr. Ibrahim Dincer (Member)

Dr. AbdulGhani Al-Farayedhi
(Department Chairman)

13/Jan/2002
Dr. Shahzada Z. Shuja (Member)

Prof. Osama A. Jannadi
(Dean, College of Graduate Studies)

30/1/2002
Date

Dedicated to
my Parents

ACKNOWLEDGEMENTS

First and foremost, all praise to the Almighty Allah Who gave me the courage and patience to carry out this work. I am happy to have had a chance to glorify His name in the sincerest way through this small accomplishment and ask Him to accept my efforts. May He guide us and the whole humanity to the right path *(Aameen)*.

Acknowledgment is due to King Fahd University of Petroleum and Minerals for providing support to this work.

My deep appreciation goes to my thesis advisor Dr. Bekir Sami Yilbas, does not arise from convention rather, from my heart-felt gratitude for his constant counsel, matchless patience and extraordinary attentiveness throughout this work. Working with him was indeed a wonderful and learning experience which I thoroughly enjoyed.

Thanks are also due to my thesis committee members Dr. Ibrahim Dincer and Dr. Shahzada Zaman Shuja for their interest, cooperation, advice and constructive criticism. I would also like to thank the department of Mechanical Engineering for providing every thing necessary to made this work possible.

Thanks are due to my parents for their prayers and moral support throughout my academic career. This work is dedicated to them for taking pains for my academic pursuits and my personality.

Thanks are due to my brothers Kamran, Ehtisham and Abbas for their love, my cousin Nasreen and her husband Ata-Abbas for their love, care and hospitality, and

my friends on campus, especially Ovais, Mofazzal, Zamin, Murshid, Zeshan and Zafar Haider, who provided some joyful moments in long work hours.

Last but not least I would like to mention my mentor Prof. Dr. Muzaffar Mahmood (NED Univ. Dept. of Mechanical Engg., Karachi), whose appreciation, encouragement and guidance helped me to choose career in academics.

Contents

List of Figures viii

List of Tables xi

Abstract (English) xii

Abstract (Arabic) xiii

1 INTRODUCTION 1

1.1 Laser 1

1.1.1 Gas Lasers 2

1.1.1.1 Neutral Gas Lasers 2

1.1.1.2 Ionized Gas Lasers 2

1.1.1.3 Molecular Lasers 3

1.1.2 Solid State Lasers 3

1.1.3 Semiconductor Lasers 4

1.1.4 Organic Dye Laser 4

1.2 Interaction of Laser with Materials 4

1.2.1 Advantages of Laser Machining 6

1.2.2 Disadvantages of Laser Machining 7

1.2.3 Classification of Laser Heating 8

1.2.3.1 Conduction Limited Heating 8

1.2.3.2 Non-Conduction Limited Heating 9

1.3 Scope of Work 11

2 LITERATURE REVIEW 12

3 MATHEMATICAL MODELING 52

3.1 Mathematical Analysis of Heating Process 52

3.1.1 Analysis of Conduction Limited Heating Process 52

3.1.2 Analysis of Non-Conduction Limited Heating Process 57

3.2 Enthalpy Method 66

3.3 Analysis of Thermal Stress 68

4 NUMERICAL METHOD and ALGORITHM 73

4.1 Introduction 73

4.2 Numerical Method 74

4.3 Finite Volume Approach 75

4.3.1 Discretization 75

4.3.2 Boundary Conditions 80

4.3.3 Stability 82

4.4 Stress Analysis 83

4.5 Solution Algorithm 85

4.5.1 Conduction Limited Heating Algorithm 85
4.5.2 Non-Conduction Limited Heating Algorithm 87

5 RESULTS and DISCUSSIONS **92**
5.1 Conduction Limited Heating 92
5.1.1 Temperature Field for Conduction Limited Heating 92
5.1.2 Stress Field for Conduction Limited Heating 101
5.2 Non-Conduction Limited Heating Step-Input Pulse Case 114
5.2.1 Temperature Field for Non-Conduction Limited Heating . . . 116
5.2.2 Stress Field for Non-Conduction Limited Heating 123
5.3 Non-Conduction Limited Heating Time Exponentially Varying Pulse Case 133
5.3.1 Temperature Field for Conduction Limited Heating with Time Varying Pulse 134
5.3.2 Stress Field for Non-Conduction Limited Heating with Time Varying Pulse 142
5.4 Validation 152

6 CONCLUSIONS **157**
6.1 Conduction Limited Heating 157
6.2 Non-Conduction Limited Heating 159

BIBLIOGRAPHY **169**

List of Figures

3.1 Schematic view of laser heating of substrate material. 54
3.2 Schematic view of a mushy cell. 61

4.1 Control Volume 77
4.2 Computational grid and boundary cells. 81
4.3 Nomenclature for stress calculation. 84
4.4 Flowchart for conduction limited heating algorithm. 86
4.5 Schematic view of laser beam profile and mesh points (n=80,m=100 for conduction limited heating, n = 480 and m = 500 for non-conduction limited heating). 88
4.6 Flowchart for non-conduction limited heating algorithm. 90

5.1 Temperature Contours. 93
5.2 Variation of dimensionless temperature along dimensionless axial distance for different heating periods. 94
5.3 Variation of dimensionless temperature gradient along dimensionless axial distance for different heating periods. 97
5.4 Temporal Variation of dimensionless temperature at different z-axis locations. 98
5.5 Temporal variation of dimensionless time derivative of dimensionless temperature at different z-axis locations. 99
5.6 Variation of dimensionless temperature along dimensionless radial distance at different z-axis locations. 100
5.7 Variation of dimensionless temperature gradient along dimensionless radial distance for different z-axis locations. 102
5.8 Radial stress contours. 103
5.9 Variation of dimensionless radial stress component along dimensionless radial distance at different z-axis locations. 104
5.10 Variation of dimensionless radial stress component along dimensionless radial distance at different heating periods. 105
5.11 Tangential stress contours. 107
5.12 Variation of dimensionless tangential stress component along dimensionless radial distance at different z-axis locations. 108
5.13 Variation of dimensionless tangential stress component along dimensionless radial distance at different heating periods. 109
5.14 Equivalent stress contours. 111
5.15 Variation of dimensionless equivalent stress along dimensionless radial distance at different z-axis locations. 112
5.16 Variation of dimensionless equivalent stress along dimensionless radial distance at different heating periods. 113
5.17 Variation of dimensionless equivalent stress along dimensionless axial distance at different heating periods. 115
5.18 Temperature Contours for different heating periods. 117

5.19 Variation of dimensionless temperature along dimensionless axial distance at different heating periods. 118
5.20 Variation of dimensionless temperature gradient along dimensionless axial distance for different heating periods. 119
5.21 Variation of dimensionless temperature along dimensionless radial distance for different heating periods. 121
5.22 Temporal variation of dimensionless surface temperature obtained from energy and enthalpy methods for constant and variable properties. . . 122
5.23 Variation of dimensionless tangential stress along dimensionless axial distance for different heating periods. 124
5.24 Variation of dimensionless tangential stress along dimensionless radial distance for different heating periods. 126
5.25 Variation of dimensionless radial stress along dimensionless axial distance for different heating periods. 127
5.26 Variation of dimensionless radial stress along dimensionless radial distance for different heating periods. 128
5.27 Equivalent stress contours for step input pulse at different heating periods. 130
5.28 Variation of dimensionless equivalent stress along dimensionless axial distance for different heating periods. 131
5.29 Variation of dimensionless equivalent stress along dimensionless radial distance for different heating periods. 132
5.30 Temperature contours at Time (t^*) = 6.1 135
5.31 Power intensity distribution with time for time exponentially varying pulse. 136
5.32 Variation of dimensionless temperature along dimensionless axial distance for different heating periods. 137
5.33 Variation of dimensionless temperature gradient along dimnsionless axial distance for different heating periods. 138
5.34 Variation of dimensionless temperature along dimensionless radial distance for different heating periods. 140
5.35 Variation of dimensionless temperature gradient along dimensionless radial distance for different heating periods. 141
5.36 Temporal variation of dimensionless surface temperature obtained for enthalpy and energy methods. 143
5.37 Variation of dimensionless tangential stress along dimensionless axial distance for different heating periods. 144
5.38 Variation of dimensionless tangential stress along dimensionless radial distance for different heating periods. 146
5.39 Variation of dimensionless radial stress along dimensionless radial distance for different heating periods. 147
5.40 Equivalent stress surface plot for time exponential pulse at different heating periods. 149
5.41 Variation of dimensionless equivalent stress along dimensionless radial distance for different heating periods. 150

5.42 Variation of dimensionless equivalent stress along dimensionless axial distance for different heating periods. 151
5.43 Comparision of dimensionless surface temperature along dimensionless time for numerical and analytical solutions. 155

List of Tables

5.1 Thermophysical properties of the substrate material and beam properties used in simulation for conduction limited heating. 156
5.2 Properties of substrate material used in computation. 156
5.3 Pulse properties for step input pulse. 156
5.4 Pulse properties for time exponentially varying pulse. 156

Abstract

Name: IFTEKHAR ZAHEER NAQAVI
Title: Conduction and Non-Conduction Limited Laser Heating Process - Mathematical Simulation.
Major Field: Mechanical Engineering
Date of Degree: November 2001

Laser heating finds wide application in industry due to its precision of operation and local treatment. Since the laser machining is involved in complex physical processes, the modeling of laser induced heating gives insight into the physical processes involved. Moreover, model studies reduce experimental cost and provided parametric data for heating optimization.

Laser non-conduction limited heating is involved with phase change processes, i.e. melting and subsequent evaporation. Depending upon the laser pulse intensity and the profile, partial melting or partial evaporation can take place in the substrate material irradiated by a laser beam. The region where partial phase change occur can be identified as a mushy zone in the substrate material. When modeling the non-conduction heating process, mushy zone should be taken into account. In the present study, pulse laser heating of metallic substrate is considered. The governing equations of heat transport pertinent to conduction and phase change processes are presented. Since, the heating model is involved with a two-dimensional axisymmetric heating, analytical solution to the problem is almost impossible; consequently, a numerical scheme employing a control volume approach is introduced to solve the governing equations of heat transfer. The thermal stress fields in the region irradiated by a laser beam is modeled and transient behavior of stresses are obtained.

Master of Science Degree
King Fahd University of Petroleum and Minerals
November 2001

خلاصة الرسالة

الاسم	افتخار ظهير نقوى
عنوان الرسالة	التسخين التوصيلي وغير التوصيلي المحدود بواسطة الليزر ٠ نموذج تمثيلي رياضي
التخصص	هندسة ميكانيكية
تاريخ الشهادة	نوفمبر ٢٠٠١ م ، شعبان ١٤٢٢ هـ

نظرا لدقة عملية التسخين بواسطة الليزر فإن لها تطبيقات واسعه في الصناعة٠ وبما أن عملية التصنيع بواسطة الليزر تتضمن تعقيدات عملية فإن نمذجة التسخين بواسطة الليزر تعطي مدخل إلى عملية التصنيع ٠ بالأضافة لذلك فإن دراسات النمذجة تقلل من التكلفة المخبرية وتزود معلومات لتحسين أداء عملية التسخين بواسطة الليزر٠

التسخين غير التوصيلي المحدود بواسطة الليزر يشتمل على تغير شكل المادة مثل الذوبان والتبخر اللاحق ٠ اعتمادا على كثافة الأشعاع الموجة ونمطة فإن ذوبان جزئي أو تبخر جزئي قد يحصل في طبقات المادة المتعرضة لأشعاع الليزر٠ المنطقة التي تتعرض لتغير فى شكل المادة يمكن تميزها بوضعها اللاسائل واللاصلب . عندما يتم نمذجة التسخين الغير توصيلي فإن هذه المنطقة ولابد أن تدخل في عملية الحسابات المعادلات المتحكمة في عملية النقل الحراري ذات الصلة بالتوصيل الحراري وعمليات تغير شكل المادة يتم تقديمها في هذه الدراسه ٠ وبما أن النموذج التمثيلي يتضمن تسخين ثنائي الأبعاد متماثل محورياً فإن حل تمثيلي لهذه المسألة غير ممكن تقريباً٠ونتيجة لذلك فإن نموذج رقمي يحتوي على طريقة تحكم حجمي يتم استخدامها لحل المعادلات المتحكمة بعملية النقل الحراري . حقول الاجهادات الحرارية في المنطقة المتعرضة لشعاع الليزر يتم نمذجتها تمثيليا والتطور المرحلي في الاجهادات الحرارية يتم حلها.

درجة الماجستير في العلوم

جامعة الملك فهد للبترول والمعادن

الظهران المملكة العربية السعودية

نوفمبر ٢٠٠١ م ، شعبان ١٤٢٢ هـ

NOMENCLATURE

a : Gaussian parameter (m)

a^* : Dimensionless Gaussian parameter $(a\delta)$

a_E, a_W, a_N, a_S, a_P : Coefficient in equation (4.2)

b_P : Coefficient in equation (4.3)

c_p : Specific heat capacity $\left(\frac{J}{kgK}\right)$

E : Elastic modulus $\left(\frac{N}{m^2}\right)$

I_o : Laser peak power intensity $\left(\frac{W}{m^2}\right)$

k : Thermal conductivity $\left(\frac{W}{mK}\right)$

k_s : Thermal conductivity for solid region $\left(\frac{W}{mK}\right)$

k_l : Thermal conductivity for solid-liquid mushy zone $\left(\frac{W}{mK}\right)$

k_b : Thermal conductivity for liquid-gas mushy zone $\left(\frac{W}{mK}\right)$

L_b : Latent heat of evaporation $\left(\frac{J}{kg}\right)$

L_m : Latent heat of melting $\left(\frac{J}{kg}\right)$

r : Radial distance (m)

r_b : Radial location of evaporating front

r_g :Distance of solid-liquid interface from axis of symmetry (m)

r_g^* :Dimensionless distance of solid-liquid interface from axis of symmetry $(r_g\delta)$

r^* : Dimensionless radial distance $(r\delta)$

r_f : Reflection coefficient

Δr : Control volume cell size in r-direction

S_o : Source term (W)

T : Temperature (^oC)

T^* : Dimensionless temperature $\left(\frac{Tk\delta}{I_o(1-r_f)}\right)$

T_b : Boiling temperature (^oC)

T_m : Melting temperature (^oC)

T_o : Initial temperature (^oC)

$T_i^o, i = P, E, W, N, S$: Intial temperature in discretized equation(4.2) and (4.3)

t : Time (s)

t^* : Dimensionless time $(\alpha\delta^2 t)$

ΔU : Energy content of differential volume (J)

Δu : Energy content per unit volume $\left(\frac{J}{m^3}\right)$

dV : Differential volume (m^3)

x : Axial distance in one-dimensional analysis (m)

x^* : Non-dimensional axial distance in one-dimensional analysis.

x_b : Mass fraction of vapor

x_m : Mass fraction of melt phase

z : Axial distance (m)

z_b : Axial location of evaporating front

z^* : Dimensionless axial distance $(z\delta)$

Δz : Control volume cell size in z-direction

Greek Symbols:

α : Thermal diffusivity $\left(\frac{m^2}{s}\right)$

α_T : Coefficient of thermal expansion (K^{-1})

δ : Absorption depth(m^{-1})

$\delta_e, \delta_w, \delta_n, \delta_s, \delta_g$: Distance between the nodal points

ε_r : Radial strain

ε_z : Axial strain

ε_θ : Tangential strain

ν : Poisson's ratio

σ_e : Equivalent stress $\left(\frac{N}{m^2}\right)$

σ_r : Radial stress $\left(\frac{N}{m^2}\right)$

σ_z : Axial stress $\left(\frac{N}{m^2}\right)$

σ_θ : Tangential stress $\left(\frac{N}{m^2}\right)$

σ_e^* : Dimensionless equivalent stress $\left(\sigma_e \left[\frac{1-\nu}{\alpha_T E}\right] \left[\frac{k\delta}{I_o(1-r_f)}\right]\right)$

σ_r^* : Dimensionless radial stress $\left(\sigma_r \left[\frac{1-\nu}{\alpha_T E}\right] \left[\frac{k\delta}{I_o(1-r_f)}\right]\right)$

σ_z^* : Dimensionless axial stress $\left(\sigma_z \left[\frac{1-\nu}{\alpha_T E}\right] \left[\frac{k\delta}{I_o(1-r_f)}\right]\right)$

σ_θ^* : Dimensionless tangential stress $\left(\sigma_\theta \left[\frac{1-\nu}{\alpha_T E}\right] \left[\frac{k\delta}{I_o(1-r_f)}\right]\right)$

φ : Stress function$\left(\frac{N}{m^3}\right)$

Subscripts:

P : The nodal point

$E, W, N, S,$: Values at east,west, north and south node points

b : evaporation related values

e, w, n, s : Values at east, west, north and south edges of the cell

g : reference from axis of symmetry to solid/mushy zone interface

Chapter 1

INTRODUCTION

1.1 Laser

The word laser is an acronym for "Light Amplification by Stimulated Emission of Radiation'. Albert Einstein in 1917 showed the process of stimulated emission must exist but it was not until 1960 that T.H. Maiman first achieved laser action at optical frequencies in ruby. The basic principles and construction of a laser are relatively straight forward and somewhat surprising that the invention of the laser was so long delayed.

Laser has three distinct properties from ordinary light sources:

- Monochromaticity
- Spatial coherence
- Time coherence

Monochromaticity defines that laser consists of only single wavelength or color of light. Spatial coherence means that light may be propagated in the form of an almost plane wave whose divergence does not exceed greatly the minimum divergence due to the diffraction. Time coherence describes the property that at any point in space laser exhibit same wave pattern at different instants of time.

There are four broad classes of lasers available classified on the basis of lasing medium:

1. Gas Lasers
2. Solid State Lasers
3. Semiconductor Lasers
4. Organic Dye Lasers.

1.1.1 Gas Lasers

Gas lasers utilize a gaseous material as the active laser medium. They can provide continuous beam of laser in some cases. There are three subcategories of gas lasers:

1.1.1.1 Neutral Gas Lasers

- Helium-Neon Lasers
- Argon Laser
- Krypton Laser
- Xenon Laser

1.1.1.2 Ionized Gas Lasers

- Argon Ion Lasers
- Krypton Ion Lasers

- Helium-Cadmium Laser

1.1.1.3 Molecular Lasers

- Carbon Dioxide Lasers
- Fast Gas Transport CO_2 Lasers
- Gas Dynamic Lasers
- Nitrogen Lasers
- Carbon Monoxide Lasers

1.1.2 Solid State Lasers

The solid state laser is characterized by active media involving ions of an impurity in some solid host material. The laser material is in the form of a cylinderical rod with the ends polished flat and parallel. The ions that are commonly employed are either ions of the transition metals, such as chromium, manganese, cobalt and nickle or of rare earth element. The host material in which these impurity elements are embedded tend to be hard, gemlike crystalline materials, or alternatively glasses. Typical examples are:

- Ruby Lasers
- Nd:YAG Lasers
- Nd: Glass Lasers

1.1.3 Semiconductor Lasers

A semiconductor laser uses a small ship of semiconductiong material. In size and appearence, it is similar to transistor. Examples are:

- GaAs Lasers
- ZnS Lasers
- ZnO Lasers
- CdS Lasers, etc.

1.1.4 Organic Dye Laser

These lasers employ liquid solutions of certain dye materials. The dye materials are relatively complex organic molecules, with molecular weights of several hundred. These materials are dissolved in organic solvents, commonly methyl alcohol. Thus, the active material for dye lasers is a liquid.

Lasers are used in many types of industrial processing, engineering, meteorology, scientific research, communications, holography, medicine, for military purposes etc. For present study our interest is in one of such application namely laser machining of materials or interaction of high power laser radiation with materials.

1.2 Interaction of Laser with Materials

The ability of lasers to produce intense pulses of radiation means that there are many potential applications involving heating, melting, and vaporization. The feature

of the laser that allows it to be used in metalworking is, of course, its ability to deliver very high power per unit area to localized regions on a workpiece. A conventional thermal source such as a welding torch delivers much lower power per unit area, and it cannot be localized so well. Only an electron beam can compare with a laser in this respect. The total power is not necessarily so important as the ability to focus to a small spot, producing a high power per unit area. A 200-W light bulb does not melt metal; a 200-W continuous laser can do so.

When laser radiation falls on a target surface, part of it absorbed and part is reflected. The energy that is absorbed begins to heat the surface. There are several regimes that should be considered, depending on the time scale and the laser power per unit area. For example, losses due to thermal conduction are small if the pulse duration is very short, but they can be important for longer pulses. There can be important effects due to absorption of the radiation in the plasma formed by vaporized material above the target surface. The losses due to radiation from the target surface are usually insignificant.

The heating due to absorption of high-power laser beams can occur very rapidly. The surface rises quickly to its melting temperature. Laser induced melting is of interest because of welding applications. One often desires maximum melting under conditions where surface vaporization does not occur. Melting without vaporization is produced only within a narrow range of laser parameters. If the laser power per unit area is too high, the surface begins to vaporize before a significant depth of molten material is produced. This means that there is a maximum power per unit area suitable for melting applications. Alternatively, for a given total energy in the

laser pulse, it is often desireable to stretch the pulse length.

Melting of a material by laser radiation depends on heat flow in the material. Heat flow is dependent on the thermal conductivity (k). But conductivity is not the only factor that influences the heat flow, since the rate of change of temperature also depends on the specific heat (c) of the meterial. In fact, the heating rate is inversely proportional to the specific heat per unit volume, which is equal to ρc, where ρ is the material density. The important factor for heat flow is thermal diffusivity i.e.$\left(\frac{k}{\rho c}\right)$.

For all unsteady-state heat flow problems, thermal diffusivity determines how repidly a material will accept and conduct thermal energy. Thus, for welding, high thermal diffusivity normally allows larger penetration of the fusion front with no thermal shock or cracking.

1.2.1 Advantages of Laser Machining

Lasers offer the following advantages in material processing:

1. No vacuum is required. For most applications the work can be done in any atmosphere, although for some reactive metals a shielding atmosphere may be desireable.

2. There is no mechanical contact with the workpiece material and contamination problems are reduced.

3. The heat-affected zone surrounding the work area is small.

4. The laser works well with hard, brittle materials or refractory materials, and it

can sometimes work for joining dissimilar metals, which are difficult to weld by conventional techniques.

5. Small hole diameters can be achieved.

6. The operation is very fast, occuring in approximately $1 \times 10^{-12} - 1 \times 10^{-3} s$ with pulse lasers.

7. The processing is readily adapted to automation.

8. No welding electrodes are required.

9. Extremely small welds may be accomplished on delicate materials.

10. Inaccessible areas or even encapsulated materials can easily be reached with the laser beam.

11. Higher power per unit area can be delivered than with any other thermal source.

1.2.2 Disadvantages of Laser Machining

There are also some disadvantages including:

1. The depth of penetration for laser-produced holes is limited, although repeated shots can increase the depth.

2. Recondensation of vaporized material occurs on the walls and on the lip of the hole, forming a raised rim around the entrance.

3. The walls of the holes are sometimes rough.

4. The cross sections of laser-produced holes are not completely round, and the holes taper from the entrance to the exit sides.

5. The control of size and tolerances on laser-produced holes is not perfect.

6. In laser welding, careful control of the pulse parameters is required to prevent vaporization of the surfaces.

7. The sizes of the pieces that can be welded are relatively small and the depth of penetration is limited, except for multikilowatt lasers.

8. In some case the costs are high.

1.2.3 Classification of Laser Heating

There are various kinds of laser material processes available and can be classified into two groups or type of processes for the case of laser heating:

1. Conduction limited

2. Non-Conduction limited

1.2.3.1 Conduction Limited Heating

If the substrate material remains solid and no phase change occurs during laser heating then the heating process can be identified as conduction limited heating. Typical examples of such processes are:

- Laser heat treating

- Laser hardening
- Laser fracturing
- Laser sheet bending

1.2.3.2 Non-Conduction Limited Heating

Heating process in which phase change of substrate material is involved is called non-conduction limited heating. There could be a simple phase change from solid to liquid or solid to liquid and subsequently liquid to gas i.e. vaporization. In case of very high input pulse of very short time period ablation process could also occur. Some examples of processes involving with non-conduction limited heating are:

- Laser welding
- Laser drilling
- Laser cutting
- Laser grooving
- Laser scribing
- Laser marking
- Laser shock processing
- Laser surface alloying

Laser machining of engineering materials requires deep investigation into laser-workpiece interaction mechanism, which is generally complicated and depends on the laser and workpiece properties. When the laser beam with sufficient power interacts with the metallic substrate, the electrons gain energy from the irradiation field. Through the successive collisions between the electrons and lattice sites, some of extra electron energy transfers to the lattice sites, which in turn result in rise of lattice site energy. The lattice sites energy, is then, conducted through phonon relaxation. This process defines the conduction in solids subjected to laser irradiation. However, depending on the time scale of interaction and energy deposition rate, the energy transport process can be non-equilibrium. In this case, the duration of interaction is on the order of pico-second and the energy transfer rate is on the order of $10^{11}\mathrm{W/m^2}$ or more. Consequently, when modeling the energy transport process in solids, care should be taken and the energy transport process should be identified.

The laser gas assisted processing is highly demanding in industry. This is due to the fact that assisting inert gas shields the surface from the high temperature oxidation reaction, which is the case when cutting non-metallic substrate by a laser beam. Alternatively, the assisting gas can be oxygen, which triggers high temperature oxidation during laser processing of metals. This application is seen in laser cutting, welding and drilling processes. Consequently when modeling the laser heating process, the gas assisting conditions should be incorporated. Introducing convective boundary conditions at the surface can fulfill this.

1.3 Scope of Work

Laser surface melting and subsequent evaporation finds wide application in industry. The laser processing of engineering materials is highly dependent on the melting and evaporation rates; therefore, improving the end product from laser processing requires investigation into the melting and subsequent evaporation processes. Moreover, the modeling of the laser interaction process reduces the experimental cost and improves the understanding of physical processes involved.

In the present work, laser heating of metallic surface is considered. The melting and subsequent evaporation processes are modeled using an energy method. The equations governing the conduction heating and phase change,(solid-liquid and liquid-vapor) are derived. Since, the governing equations are in two-dimensional axisymmetric form, a numerical method employing a control volume approach is introduced to solve the governing equations of energy. Because laser induced heating generate a very high temperature gradient in the vicinity of surface a high level of thermal stress is developed; consequently, we are also modeling the stress field using plain strain conditions.

Chapter 2

LITERATURE REVIEW

Laser heating is involved with complicated physical processes. The modeling of the heating process reduces the experimental cost and gives insight into the physical processes involved. Considerable research studies were carried out in the past to explore the conduction and non-conduction limited heating process. The previous studies pertinent to conduction and non-conduction limited laser heating are given as follows.

Conduction Limited Laser Heating

Analytical Solutions

Modest and Abakians [1] studied heat conduction in a moving semi-infinite medium subject to laser irradiation. They expanded the conduction solutions to include the cases of scanning CW and pulsed Gaussian lasers, whose energy penetrates into a sami-infinite body with exponential decay. They developed a one-dimensional conduction model with solution in integral form, which would be applicable in more complicated cases of laser induced melting and evaporation ,and determine the conditions of its validity. For continuous source their model agreed well with exact solution for higher scanning speeds.

Blackwell [2] obtained analytical solution using Laplace transforms for the tem-

perature profile in a sami-infinite body with an exponentially decaying source and convective boundary condition. He developed a model for determining the location of maximum temperature prior to the initiation of phase change. He found that the maximum temperature occured at an interior point and its location relative to the exposed surface increased with increased dimensionless convective cooling and time.

Maier etal. [3] calculated three-dimensional time-dependent temperature profile, using Green's function method, of laser treated metallic samples. From these temperature fields they attempted to determine the structure and phase composition of the irradiated samples. Using temperature profiles from sample calculations for crystalline Fe-B-Si foils they calculated the cooling rate at different depths for an interval of 10 ns after the pulse. These calculations yielded a cooling rate higher than $10^6 Ks^{-1}$ down to depth of $0.4\mu m$. The necessary cooling rate for the formation of amorphous layers is $10^6 Ks^{-1}$. Therefore the calculations leaded them to the conclusion that the crystalline foil became amorphous down to a depth of $0.4\mu m$ by laser treatment. Experimental results indicated that amorphous layer formed by laser treatment for similar material was thinner than $1\mu m$.

Zubair and Chaudhry [5] discussed an analytical solution of a semi-infinite solid when subjected to an instantaneous laser source. they pointed out that the instantaneous source was identified by the Dirac delta function; therefore, the temperature solution might be considered as a fundamental solution to the continuously operating heat source problem.

Romer and Meijer [7] discussed the analytical models of the maximum surface temperature induced by a stationary laser beam. They also investigated the maximum

surface temperature induced by a moving laser beam. They compared the predictions with experimental results.

The two-step model involved two coupled energy equations governing the heat transfer in the electron gas and the metal lattice. Al-Nimr and Masoud [8] used a perturbation technique to eliminate the coupling between the two energy equations. The elimination of this coupling produced two uncoupled partial differential equations which had the same order as the original coupled partial differential eqution and which did not contain any mixed derivatives terms.

Al-Nimr and Arpaci [14] introduced a simplified approach which described the thermal behavior of a thin film exposed to picosecond thermal pulses. It was assumed that the metal film thermal behavior occured in two successive stages. In the first stage, electron gas transmited its energy to the solid lattie, and at the end of this stage, both electron gas and solid lttice reach the state of thermal equilibrium. In the second stage, the energy transfer through electron-phonon coupling was negligible and the thermal diffusion became important. They proposed the approach which eliminated the coupling between the energy equation of both solid lattice and electron gas and as a result, it was much easier to solve the reduced partial differential equations.

Ramos [16] developed a closed form solution, using the known Green's function method, for the time dependent temperature evolution inside an infinitely extended solid medium of finite thickness induced by a moving cylinderical laser beam with gaussian energy distribution. Physical properties were taken to be temperature independent and no phase changes were considered in this model. The domain geometry consisted of a semi-infinite sheet of finite thickness. The laser was coupled to the

surface by pure conductive heat transfer mechanism taken as a uniaxially moving non-linear boundary condition; heat loss by convection mechanism wass also included at the latter boundary. At the bottom of the sheet total insulation was applied as the boundary condition. This model allowed the estimation of process parameters (i.e. Fourier and Peclet numbers) during laser heat treatment of metal alloys such as laser annealing, bending and surface hardening. Due to the fact that the coordinate system was fixed to the laser beam axis and the time dependence was short lived, the model could be considered to behave in a quasi-static manner for practical purposes. He presented numerical results for a 1mm thick Al-Cu alloy sheet scanned at different velocities with a 250 W continuous wave CO_2 laser.

Yilbas and Shuja [9] carried out a study to predict the temperature rise at the surface and inside the material using a Fourier heat transfer model for a step pulse input. They obtained an analytical solution to determine the heating and cooling rates and , later, developed non-dimensional emperical equations in this regard. To validate the theoretical predictions they conducted an experiment to measure the surface temperature rise due to Nd:YAG laser irradiation of steel substrate. Since the Nd:YAG laser output pulse length was limited, three pulse lengths were considered and these were introduced in the theoratical predictions. The predicted and eperimentally measured surface temperatures were found to be in a good agreement.

Yilbas and Kalyon [24] considered repetitive laser pulse heating of steel with a convective boundary condition at the surface. A closed form solution for the laser heating process was obtained using a Laplace transformation method. The conditions for constant temperature heating at the surface were investigated and the pulse

parameter resulting in the possible steady temperature attainment at the surface was discussed.

Yilbas etal. [10] introduced the heat transfer mechanism that initiated the surface heat treatment and developed analytical approaches governing the conduction and non-conduction limited processes. They predicted temperature profiles corresponding to laser output pulses of varying duration, but having the same energy content. They derived and computed the thermal effeciencies of the laser surface treatment process using these temperature profiles. In this way, the optimal pulse shape giving the highest thermal effeciency of the surface treatment was obtained. For conduction limited heating they distinguished three regions in heating cycle. In first region absorption dominated the conduction losses; internal energy of the treated solid and hence its surface temperature increased rapidly. In second region an energy balance existed between absorption, internal energy and conduction losses giving rise to a constant rate of change of temperature. In third region the rate of change of temperature started to fall off, resulting in high conduction losses. Effeciency analysis for laser heat treatment indicated that shorter laser pulse lengths resulted in higher thermal effeciency, provided that the energy content of the pulse was constant. In addition, the governing equation for thermal efeciency predicted higher effeciency at lower induced temperatures. They showed that the effeciency of non-conduction limited model was higher than that of conduction limited model.

Numerical Simulations

Non-Fourier Heating Models

Qiu and Tien [4] analyzed the microscopic processes in radiation-metal interac-

tions and explored their effects on the spetial and temporal responses of the metal lattice temperature to short pulse laser irradiation. They compared the conventional one-step heating model with two-step heating model for non-equilibrium heating. According to two step model electrons absorbed the photon energy and then heat up the metal lattice through electron-phonon collisions. They found that in long-pulse laser heating, the one-step model was valid; in short-pulse laser heating, the two-step radiation heating model should be applied. They defined a critical number to separate these two regimes quantitatively. They concluded that in a fast heating regime (pulse duration of the order of pico-seconds or shorter), The microscopic energy transfer among photons, electrons and phonons became very important. It enlarged the heat-affected region and lowered the peak temperature rise of the metal lattice significantly. The conventional one-step radiation heating model overpredicted the peak surface temperature and underpredicted the heat-affected region. In a slow heating regime (pulse duration of the order of nanoseconds), the two-step radiation heating model reduced to the conventional radiation heating model. The transient reflectivity changes predicted from the two-step model agreed with sub-picosecond laser heating experiment.

Phinney and Tien [13] examined the removal of undesireable surface species from metals using short-pulse lasers. They presented the two-temperature model for laser short pulse heating process. They identified the regimes of thermal and electronic desorption and presented the implications for optimum laser surface contaminant removal. They concluded that in short pulse laser heating of materials, a non-equilibrium occured between the electron and lattice temperatures for laser pulse

durations on the order of or less than the electron lattice relaxation time. The high electron temperatures were conducive to electronically induced desorption as well as desorption due to thermal heating. A scalling analysis comparing the expected nonequilibrium in temperatures and increase in the lattice temperature indicated the dependence of the relative desorption yields on three ratios: the lattice and electron specific heats, the electron-lattice relaxation time and laser pulse duration, and the heat and radiation penetration depths. For very short laser pulse durations, fluence levels below those required to significantly heat the material could be used to remove contaminants, which was important for processes with constraints on the amount of temperature increase. Calculations of laser induced desorption indicated that significant desorption could result from electronic excitations.

Yilbas and Sami [17] carried out a study to develop a three-dimensional model for a pulsed heating process using an electron kinetic theory approach. The heating model introduced relied on successive electron-phonon collisions; therefore, it was this process that described the heat conduction mechanism. This study was limited to heat conduction only. Consequentl, the phase change process was not taken into account. To validate the theoratical predictions, an experiment was conducted to measure the surface temperature using an optical method. They also considered a one-dimensional model and compared the predictions from one and three-dimensional model with experimental results. They concluded that the energy gain by electrons via laser beam radiation dominated the conduction losses through electron-phonon collisions in the early stage of the heating process. This might result in a rapid increase in temperature in the surface region. When the heating pulse ends, the cooling cycle

started and electrons gave their excess energies to phonons without gaining energy from the external field. Since only a fraction of excess energy was transferred to a phonon for a single colision, the decay of the cooling rate became slow in the three dimensional case. When comparing the temperature profiles obtained from one-dimensional and three-dimensional models for radial heat conduction, the three-dimensional model resulted in lower temperature profile than that corresponding to the one-dimensional model. However, the experimental results agreed well with the surface temperature profile predited from the three-dimensional model.

Yilbas and Shuja [19] made comparisions of the electron kinetic theory approach, two-equation and one-equation models for a pulse laser heating process. The temperature field due to each model was predicted for step intensity as well as exponentially decaying intensity pulses. Since an analytical solution did not exist for the two-equation model, a numerical scheme was introduced to solve the governing equations. Moreover, the study was extended to include the analytical solution of the electron kinetic theory approach for intensity exponentially decaying pulses. To validate the closed form solutions of the electron kinetic and Fourier theories, a numerical solution of the equations was also introduced. They concluded that the numerical solutions obtained from all models employed resulted in similar temperature profiles inside and at the surface of the substrate for heating time upto that of $10^{-9}s$. This finding was also observed in a comparision of the analytical results for step input intensity pulses. As the pulse length decreased while the intensity increases, the two-equation and electron kinetic theory approaches results deviated from the one-equatin model results. In this case, nonequilibrium heating dominated the energy exchange mecha-

nism. Moreover, for short pulse heating the electron kinetic theory predicted slightly lower surface temperatures than those predicted by the two-equation model. This might be due to the fact that the rate of collision between the electrons and lattice site atoms in the surface vicinity resulted in less energy transfer from the excited electrons to lattice site atoms in the electron kinetic theory approach.

Yilbas [23] considered laser heating of gold with a moving heat source and convective boundary conditions. Three-dimensional electron kinetic theory approach was introduced when modeling the non-equilibrium heating process. The governing energy equation and the boundary conditions were non-dimensionalized with the appropriate laser and workpiece parameters. In the analysis, the heat transfer coefficient across the heated surface was assumed to be uniform and constant. The laser beam was considered to scan the workpiece surface with a constant speed. In addition, he compared the predictions with the one- and two-equation model findings. He concluded that the electron kinetic theory predictions agreed well with the two-equation model findings for a short heating duration. As the laser scanning speed increased, the location of the peak surface temperature changed. The rate of decay of the temperature profiles inside the substrate reduced as the scanning speed increased.

Fourier Heating Model

Ehrhard etal. [6] predicted for the penatration depth for a specific temperature and the peak temperature. They considered a brick-type workpiece of infinite length but finite thickness and width, while in general a three-dimensional heat flow was presented. They particularly investigated the heat flux through the bottom plane into the table and envisioned a process control by means of the control of the thermal con-

tact of the workpiece and table. They used Finite Element Method (FEM) numerical simulation for predictions. Adjustable parameters for this study were scanning speed and power density. For high scanning velocities penetration depth was independent of thermal contact. Penetration depth increased linearly with net heat input. Slope of these linear curves varied inversely with scanning velocities.

Zhong and Wu [11] developed a numerical model to analyze the temperature distribution in the sheet during laser scanning and to apply it to the laser forming process, so that the effects on the process of parameters such as the laser power, the scanning velocity and sheet thickness could be studied. They found that the peak temperature value and temperature gradient were increased with increasing of laser power, but the relationship between them was non-linear. They also found that peak temperature decreased with increase in scanning velocity and sheet thickness, but temperature gradient did not change identically.

Manca etal. [15] solved numerically a simplified three-dimensional quasi-steady state thermal conductive model in a solid with finite depth and width but with infinite length under a moving heat source. The proposed model allowed for both convective and radiative surface heat losses, and variable prperties. The convective heat transfer was due to an impinging jet. They concluded that for certain scanning velocity, the axial diffusive heat transfer along the motion direction could be neglected, even for solids with finite thickness. This approximation made the three-dimensional elliptic partial differential equation a parabolic one along the motion direction. They observed a maximum deviation between the proposed numerical solution and the analytical was about 0.1 percent.

A new approach, developed at the National Research Council of Canada's Integrated Manufacturing Technologies Institute, used discrete pulses to create a series of hardened "spots". Woodard and Dryden [18] presented a solution to the heat conduction equation for axisymmetric flow under a Gaussian beam distribution, which modeled the thermal process from the initial stages of heating. This solution was used to create several useful relations for obtaining initial size estimates of the size of a transformation hardened spot. They applied these tools to the dot matrix hardening process, and compared the results to a commercially available finite element analysis package.

Laser Heating With Gas Jet Impingement

Shuja and Yilbas [12] carried out the study of two-dimensional axisymmetric laser repetitive pulse heating of a steel surface. The assisting gas jet effect was included, with the gas jet consideed to impinge coaxially with the laser beam and orthogonally to the workpiece surface. The $k - \epsilon$ low-Reynolds number turbulence model was employed to account for the turbulence effect. The governing flow and heat conduction equations were solved numerically using control volume approach in which variable properties were used for assist gas and solid substrate. The study was extended to include two gas jet velocities and three pulse types. In addition, to investigate the influence of the heat transfer coefficient on the temperature profiles due to convective boundary conditions at the surface, the analytical solution was employed. They concluded that the temperature at the surface pulsated in a similar manner to consecutive laser pulses and the amplitude of this pulsing decreased with the intensity ratio. The surface temperature, in general, showed an increasing trend

with time at high intesity ratios. However, the gas side temperature was not influenced considerably by the convective and diffusive heat transfer from the irradiated surface because of the size of the heated spot and resulting low heat transfer coefficient. The pulsing in temperature decayed as the distance from the surface increased towards the solid bulk and the influence of the pulse intensity ratio on the resulting temperatures on the solid side became considerable. In this case, the internal energy gain by the substrate owing to the incident laser beam was substantial compared with conduction and convection losses.

Shuja and Yilbas [20] performed numerical investigation into a laser-assisted heating process. The laser source was assumed to be stationary while the workpiece, which was stainless steel, moved with a constant speed. The assisting gas, which was air, impinged at the workpiece surface coaxially with the laser beam. Three-dimensional model was taken into account for the impinging gas jet and the transient conjugate heating process. The low Reynolds number $k-\epsilon$ model was considered to account for the turbulence. The resulting flow and conduction equations were discretized using a control volume approach. The simulations were repeated for three work-piece speeds and one assisting gas jet velocity. They found that the surface temperature rise was influenced significantly by the workpiece speed. The cooling of the surface due to gas jet impingement was more pronounced towards the edge of the heated spot. The peak values of the surface temperature moved towards the direction of workpiece motion as the workpiece speed increased. The influence of laser power intensity distribution across the heated spot on the surface temperature was significant. Moreover, the convective cooling of the surface close to the heated spot edge was evident because

of the flow development in the transversal direction. Attainment of high-pressure gradient in the region close to the workpiece surface resulted in almost symmetric velocity vectors in the $x - z$ plane.

Yilbas etal. [21] carried out numerical simulation of nano-second laser pulse heating of steel. Air was considered as an assisting gas, emerging from a nozzle and impinging co-axially with the laser beam onto the workpiece. Two-dimensional axisymmetric flow equations and an energy equation were solved numerically using a control volume approach, which in turn enabled computation of the flow and temperature fields in the laser heated region. A low Reynolds number $k - \epsilon$ model was considered to account for the turbulence. To validate the theoratical predictions, an analytical solution was employed using the same conditions as the numerical simulation. They concluded that the surface temperature rises at a fast rate in the laser pulse beginning, in which case the internal energy gain dominated the conduction and convection losses. As the heating progresses, internal energy increased at a constant rate, which in turn resulted in the attainment of equilibrium heating. The temperature profiles inside the substrate, which were predicted numerically and analytically, were in good agreement.

Shuja and Yilbas [22] examined the gas-assisted single-pulse laser heating process. Air was considered as the impinging gas and stainless steel was selected as the workpiece material. When modeling the conjugate heating process, the workpiece was considered to move with a constant velocity while the laser beam profile was assumed to be Gaussian. The three-dimensional governing flow and heat equations were solved numerically using the control volume approach. The flow properties were

considered to be variable and low Reynolds number $k - \epsilon$ model was considered to account for the turbulence. They concluded that the resulting temperature profiles in the solid were symmetrical at early heating times, and they were not affected by the impinging gas jet velocity during the heating cycle. The maximum surface temperature occured some distance away from the initially heated spot center owing to the workpiece movement.

Non-Conduction Limited Laser Heating

Gonsalves and Duley [25] presented the results of a quantitative investigation into the interdependence of the parameters, the incident power, the radius of the focused spot on the target, the cutting speed, the cut width and the sheet thickness. They also showed how these results could be generalized to provide a prediction of the power required to achieve a certain cutting velocity or cut width with predetermined focal area on thin sheets of arbitrary composition.

Simulations of Laser Cutting

Modest and Abakians [26] considered partial vaporization of a semi-infinite medium caused by a moving Gaussian laser irradiation (across the vaporization surface). They used a simple integral method for the evaluation of temperature distribution, assuming relatively minor thermal losses due to convection, conduction and radiation. They solved the relevant nonlinear partial differential equation numerically and presented the results for the groove depth, width and shape for variety of laser and solid parameters. Their results clearly indicated that surface heat losses were nearly always negligible. It was seen that, for a Gaussian beam, the bottom of the groove might have a sharp apex. The model was also able to predict quantitatively groove depths

accurately for a few situations.

Multiple reflection and beam guiding effects become important for highly reflective materials or for deep grooves with aspect ratios greater than one. Bang and Modest [30] analyzed numerically multiple reflection and beam guiding effects during laser machining. They considered that the surface of the treated material reflected the laser irradiation in a fully diffuse fashion, limiting the analysis to bodies that had a rough surface during laser evaporation (e.g. micro-explosive removal, violent surface boiling). For local irradiation calculations the material surface was divided into a number of triangular elements with linear interpolation functions. The net radiative flux for these elements was obtained from standard view factor theory. The irradiation calculations were combined with a simple integral method governing conduction losses into the medium, and the resulting groove shape and depth were found through an iterative procedure. They concluded that beam guiding played an important role in forming the fully developed groove, resulting in an increased effective absorptivity. Due to channeling from the upstream wall as well as the side walls, the evaporation zone extended farther down-stream and the fully developed groove cross sections had steeper groove walls with a flatter center region as compared to that predicted by the previous model without reflection effects. For materials with relatively large reflectivity, the material removal rate was increased significantly, resulting in an increased effective absorptivity. Generally, the beam guiding effects became significant for high reflectivity materials and/or deep groove cases.The groove depth could be increased by using lenses with larger focal lengths focused slightly inside the material. Larger focal length lenses had larger minimum beam radii at the focal plane, but with a

lower beam divergence focused near the surface. On the other hand, flatter grooves with steeper walls could be obtained by using lenses with shorter focal lengths.

Roy and Modest [31] developed a three dimensional conduction model to predict the temperature distribution inside the solid and the shape of a groove formed by partial evaporation of a semi-infinite body using a moving CW laser with a Gaussian beam profile. This had application in laser machining where material was removed by repeated scanning of a focussed beam on the workpiece surface. They solved the governing equation using a finite difference method on an algebrically-generated boundary-fitted coordinate system. They presented the groove shape and temperature distribution in the solid for both constant properties and variable properties, for different speeds, for various laser power levels and for different beam profiles. The groove shapes for constant thermal properties were compared with three-dimensional boundary element conduction model solution and a quasi-one-dimensional conduction model solution, in which the conduction losses were approximated using a simple integral method. Their model compared well with the three-dimensional boundary element model for all ranges of laser parameters, and, when thermal losses due to conduction were minor, the one-dimensional results were also in good agreement with the three-dimensional boundary element predictions. They concluded that heat loss by conduction could be between 25 to 45% of absorbed laser power, at higher power losses were lower. They obtained experimental results for material removal rates and groove shapes on silicon nitride, which were found to agree well with theoratical predictions for shallow grooves.

Bang etal. [32] analyzed theoratically the beam guiding effects during laser ma-

chining for ceramics due to multiple reflections in the groove for two extreme cases – purely specular and purely diffuse reflections. Specular reflections were valid for materials that had a smooth surface during laser evaporation (small optical roughness as compared to the laser wavelength). For such cases the material surface was divided into a number of rectangular patches using a bicubic surface representation method. The net radiative flux for these patch elements was obtained by ray tracing methods. The resulting radiative flux due to specular reflections was combined with the three dimensional conduction equation governing conduction losses into the medium, and the resulting groove shape and depth were found through an iterative procedure. Diffuse reflections were valid for materials that had a very rough surface during material removal. To address beam coupling due to diffuse reflections, irradiation calculations employing view factor were combined with three-dimensional conduction model. Considering multiple reflections resulted in an increased absorptivity and deeper grooves, accompanied by a flatter profile near the centerline and steeper slopes in the other parts of the groove cross-section. They predicted for the tested set of parameters, material removal rates were increased by up to 40% by specular reflections and up to 70% by diffuse reflections. They compared their results with experiments, hot-pressed silicon nitride ceramic showed increased beam coupling for deeper grooves (high power and/or slow scanning speeds) as predicted by considering multiple reflections. The agreement between theoratical calculations and experimental data for material removal rate and groove shape was good, if multiple reflections were assumed to be diffuse.

Modest [39] developed a three-dimensional conduction model to predict the tran-

sient temperature distribution inside a thick solid that was irradiated by a moving laser source, and the changing shape of a groove carved into it by evaporation of material. The laser might operate in CW or in pulsed mode with arbitrary temporal as well as spatial intensity distribution. He solved the governing equations using a finite-difference method on an algebrically-generated boundary-fitted coordinate system. He varified this transient model with three-dimensional codes that were limited to quasi-steady CW operation. He presented the groove shapes and temperature distribution, as well as their transient development, for various machining conditions, demonstrating the differences in the ablation process between CW, pulsed and Q-switched (or other pulses of extremely short duration) laser operation. The results showed that during short-pulsed laser ablation conduction losses were essentially negligible, resulting in substantially larger removal rates than for CW operation. Ablation with normally pulsed lasers, on the other hand, resulted in removal rates, which approached those of a Q-switched laser, but the thickness of the heat-affected layer was much larger, approaching that of the CW laser. The calculation further indicated that, during short-pulsed laser ablation, the material cooled off rapidly after the end of the pulse, returning to ambient conditions well before the beginning of the subsequent pulse.

Modest [51] developed a model of full three dimensional transient through-cutting in thin sheets. He also developed a two-dimensional axisymmetric version to model and predict results for drilling. He solved three-dimensional conduction equation numerically using boundary fitted coordinates. Using his model he found that under all circumstances even the maximum possible convection and radiation losses could

have only a negligible effect on temperature and groove development.

Beam Vapor Interaction

Yilbas and Yilbas [27] studied the interaction mechanism of vapor generated by laser beam over the surface of workpiece. The vapor heated the workpiece surface and absorbed some fraction of incident energy. They developed a computer program to model gas dynamic equations in one-dimension with additional terms for absorption of laser beam, radiation losses and conduction. They assumed that vapor was comprise of heavy particles and free electrons, each species behaving as a perfect gas. They found that the evalution of the expansion of vapor plug was sensitive to variations in initial conditions. The vapor temperature increasd from initial value to $10000K$ in $10^{-7} - 10^{-6}$ *sec* after which further increament occured relatively slowly. The leading edge of the vapor had velocity of the order of $4000 - 7000\ m/s$.

Yilbas etal. [28] examined the absorption of a laser beam at different wavelengths by a partially ionized vapor during the interaction mechanism.They distinguished the interaction of the high and low power laser beam with plasma. They showed that different metal vapors at similar temperatures and densities had absorption depths which might differ by an order of magnitude. They also showed that the free electron temperature became significantly different from the heavy particle temperature for power intensities above the critical level which was typically greater than $10^{14}\ W/m^2$.

Simulations With Enthalpy Method

Wei and Ho [29] determined energy transfers and penetration velocity during a high-energy drilling or welding process. The beam energy of a Gaussian distribution incident on the free surface of a liquid layer that separated unmelted solid and vapour

was balanced with the heat conduction and latent heats for melting and evaporation. They examined the effects of the beam power and the energy distribution on the high-energy beam drilling. The normal pressure condition at the vapour-liquid interface was used to determine the shape of the vapour-liquid interface. The heat conduction in both the axial and the radial directions, heat of evaporation and melting were taken into account. The fusion line, however, was calculated by using the enthalpy method. They developed a quasi-stead, axisymmetric heat conduction model to investigate the penetrating process of the cavity produced by high energy beam. The shape of the fusion zone and the penetration velocity were determined as a function of energy distribution parameters and the beam power, rather than specified a priori. They showed that the energy distribution parameter had stronger effects than the beam power on the high-energy beam drilling or welding process. The penetration velocity increased with increasing beam power or decreasing energy distribution parameter. Increasing the energy flux resulted in a slight increase in radial conduction loss. Since the sensible heat of raising the liquid from the melting temperature to the base temperature was small, the energy transfered to the liquid-solid interface became larger for a higher energy flux. This resulted in a non-linear and significant increase in the penetration velocity at a high beam power or a small energy distribution parameter. High temperature gradients occured near the cavity base.

Faghri etal [48] [49]developed a comprehensive model to study the laser drilling process and used volume of flow technique to track the position of moving vapor front and recession of surface.

Zhang and Faghri [56] investigated the melting and vaporization phenomena dur-

ing the laser drilling process. The locations of the solid-liquid and liquid-vapor interfaces were obtained by solving energy conservation equations at interfaces. The dependence of saturation temperature on the back pressure was taken into account by using the Clausius/Clapeyron equation. They also included the conduction heat loss to the workpiece and solved it using an integral approximation method. The predicted material removal rate agreed well with the experimental data. The amount of heat lost through conduction was found to be very small and its effect on the vaporization was not significant. However, the locations of melting front was significantly affected by conduction heat loss specially for lower laser intensity and longer pulse. The existance of subcooling in the solid was helpful in reducing the thickness of recast layer.

Rostami and Raisi [61] used the modified enthalpy method to solve for the temperature distribution and melt pool shape in a semi-infinite body. The target material was melting as a result of energy absorption from a moving laser beam. The beam profile could be elliptic or circular, but its intensity was limited, so that no vaporization occured at the surface of the workpiece. The problem was unsteady and involved three-dimensional conduction including a moving heat source and a moving boundary. They used an explicit finite difference method with two different homogeneous grid patterns.They found that the depth of the pool did not change significantly as the nondimensional target speed, which was in the $x-$direction, changed from 0 to 0.45. The melt pool size decreased slightly as the speed increased.

Solana and Ocana [62] constructed a detailed model in order to determine the three-dimensional weld pool and keyhole geometry by setting the appropriate energy

and pressure balances. The energy balance took into account heat conduction, ablation losses and evaporation efects at the keyhole open surfaces, as well as the most relevant energy-absorption mechanism, namely Fersnel and inverse Bremsstrahlung. The pressure balance ensured mechanical stability of the keyhole by including ablation pressure against surface tension pressure. The moving boundary was obtained as a result of the solution of the problem, without any shape or location being prescribed for it in advance. It was found that, for medium welding speeds, the keyhole boundary could be successfully fitted with a family of ovoids at each depth, reducing the computational time substantially.

Kim and Sim [63] simulated the transient and steady state laser melting problems numerically for steel and $Al-4.5\%Cu$. They considered the melting of alloys for which there was a range of melting temperature and a mushy zone appear. They included the flow in mushy zone in modeling. They compared the geometry of the pool, the free surface velocity and the surface temperature with and without convection in mushy zone. They concluded that the surface-tension driven convection played an important role in the total heat transfer. The distortion of the isotherm from a pure conduction isotherm showed the dominance of convective heat transfer.

Analytical solutions for laser cutting and heating assumed a cylinderical heat source and did not regard the effect of cutting kerf. Schultz etal. [33] solved the heat conduction problem numerically to overcome this restriction and made allowance for the influence of the cuuting kerf. They discussed the influences of temperature-dependent material properties, heat transfer from the workpiece into the cutting gas and heat release into the workpiece owing to adherent dross. They approximated the

numerically determined conductive power by a formula in form of power law. In order to prove the applicability of this power law, they determined the power losses into the metal sheet experimentally.

Gas Assisted Cutting

Yilbas and Sahin [34] investigated the laser gas-assisting cutting process allowing the momentum effects and chemical contribution of the assisting gas. In modelling the gas-assisting cutting process, they assumed a turbulent boundary layer within the gas-liquid interface. Fluid equations governing the the flow field in one dimension were considered. Consequently, the effects of chemical reactions on the skin friction coefficient and heat transfer coefficient for the reacting turbulent gas boundary layer was derived and calculated. Later, mass difusion in the interface zone is allowed to determine the effect of the mass diffusion process on the heat transfer coefficient. They extended the study to include an experimental investigation of cutting speed at various combinations of cutting parameters. In addition, emission from the initial surface plume generated during the laser cutting process was monitored using a fast recording video camera and fibre-optic probe. This provided an understanding of the oxygen effect and initiation of the cutting process. They employed oxygen as the assisting gas at levels in the range $75 - 175kPa$ and used mild steel within the range of 0.8 and $2mm$ thicknesses as workpiece. They concluded that an increase in power intensity over the cut surface initially gave rise to a substantial increment in cutting speed. Subsequently, the rise continues at a slow rate until a point was reached where the cutting speed saturated for the given jet velocity. Insufficient oxygen flow prevented the oxidation of molten matel at high speed or the removal of

the molten metal from the cutting zone. As the gas jet velocity increased the laser power requirement became less for a given cutting speed and material thickness.

Yilbas and Sahin [36] examined the combined effects of chemical reactions taking place between a gas jet and molten matel, the cooling effect of the jet and the evaporation of metal, during a CO_2 laser cutting process. They used a laminar boundary layer approach to develop a theoratical model for the oxygen gas jet laser cutting mechanism. They also carried out an experiment to monitor the keyhole formation using a video recorder and detect the light emitted from the entrance and exit surfaces of the workpiece using a fibre-optic probe during the cutting process. They found that the heat transfer rate to the liquid metal decreased with increasing material thickness resulting in an increased chemical reaction effect. The total chemical reaction contribution over the cut width increased with increasing jet velocity. The laminar boundary layer approach held for a cutting speed upto about 30 $mm\ s^{-1}$ and all jet velocities upto sonic. Brighter surface plasma existed for stainless steel samples than was the case for mild steel samples. This might indicate that the contribution of the chemical reaction to the cutting process was higher in the case of stainless steel workpiece.

Chen [53] examined systematically the effects of gas composition on the CO_2 laser cutting of mild steel through experimental study. He tried to identified the dominant factors for which variation could lead to large effects on cut quality. He selected gas composition and gas pressure as dominant factors. Their effects on the cut quality was investigated, with particular refrence to small variations in gas composition. He used gas mixture composed of oxygen, argon, nitrogen, Helium. He concluded that

minute impurity levels (1.25%) reduced the cut quality and also caused oxide layer on cut surface, dross adhesion and reduced cutting speed. In cutting 3 mm mild steel using pure oxygen with a laser power of 1500 W, a good cut region existed. For good cut pressure range should be 0.75 to 2 bar and cut speed should be 20 to 40 $mm\ s^{-1}$.

Keyhole and Kerf Modeling

Almost all laser assisted materials processing involves melting, vaporization and plasma formation which affect the utilization of laser energy for materials processing. To account for the effect of these phases, a definition of effective absorptivity is required. Kar etal. [46] developed a simple mathematical model for the cutting of thick-section stainless steel using a high power chemical oxygen iodine laser. The model was based on an overall energy balance, and it related the cutting depth with various process parameters that could be used to predictively scale the laser materials processing performance to very thick sections. They examined the effects of absorptivity and the velocity of the cutting gas jet on the kerf depth and width. The study indicated that thick metal cutting performance might be improved by producing narrow kerf widths. The scaling law for cut depth per unit power closely agreed with the experimental data. However, the scaling law kerf width closely compared with the experimental data at low cutting speeds since it was obtained by assuming a large conduction heat loss that held good at low cutting speeds. The laser-plume interaction and effective absorptivity played an important role in the cutting performance of a laser beam.

Solana etal. [57] provided a model for laser drilling capable of taking into account the effect of laser-light absorption within the metal vapor generated as the hole de-

veloped, as well as to analyse the drilling speeds and hole profiles for various types of laser sources, namely a constant laser source, a square-wave source and a cosine-wave source. The model for the complete analysis of the drilling speed was one-dimensional in character. They predicted a limiting penetration depth, depending both on the laser intensity and on material properties. They obtained the hole profiles by extending the one-dimensional model to axisymmetrical one. The model took into account the formation and further evolution of an evaporation front, giving a full account of heat transfer mechanisms inside the workpiece. In the energy balance at the evaporation front the attenuated laser intensity was used effectively for evaporating material and for heat conduction inside the target material.

Yilbas [58] investigated the effect of fluctuations of laser and workpiece parameters on the size of striation formation. These parameters included the laser power, energy coupling factor and cutting speed. A mathematical model based on a scaling law was employed to formulate the size of the kerf width. The predictions of the model were compared with experimental results. He also discussed some cutting deficiencies due to high temperature oxidation reaction. He concluded that increasing the energy coupling factor increases the kerf width. This was more pronounced at low cutting speed and high laser power. In ths case, energy available at the workpiece surface increased, which in turn increased the size of the melt zone in the kerf. Increasing cutting speed reduced the kerf width provided that it did not exceed the maximum cutting speed possible for the laser cutting process. The effect of laser power on the kerf width was highly significant, since a small variation in laser power altered the kerf size considerably.

Kroos etal. [59] studied the dynamic behaviour of a keyhole in laser welding theoretically. Starting from the stationary state, where the recoil pressure from ablating particles was in equlibrium with surface tension at keyhole wall, the collapse time due to a sudden laser shut down was calculated. They also studied the stability behavior of a key hole under cw conditions. In the first case, the balance between the surface tension and inertia of the melt was identified as the phenomenon which determineed the closing time. Typical values for Al, Fe and Cu are of the order of 0.1 ms. If the spacing between two successive pulses exceeds the closing time of key hole, the resulting weld would not be continuous.

Matsunawa and Semak [60] described a physical model of keyhole support and propagation during high-translation-speed laser welding. They developed a numerical code for the simulation of the front keyhole wall behaviour on the basis of a 'hydrodynamic' physical model assuming that: (i) only the front part of the keyhole wall was to the high-intensity laser beam; and (ii) recoil pressure exceeded surface tension and propagation of the keyhole wall inside the sample was due to melt expulsion similar to that in laser drilling. They calculated the front keyhole wall profile, distribution of absorbed laser intensity and phase velocity of the solid/liquid and liquid/vapor boundary for various processing parameters. Their calculation showed that, depending on the processing conditions, the absolute value of the keyhole wall velocity component parallel to the translation velocity vector could be higher or equal to the beam translation speed. When the component of the keyhole velocity vector parallel to the sample surface was higher than the beam translation speed, the formation of the humps on the keyhole wall was observed numerically.

Semak and Matsunawa [41] carried out a theoratical analysis of the energy balance in the laser-metal interaction zone. They considered the heat transfer due to the recoil-pressure-induced melt flow. The results of numerical simulations showed that the recoil pressure could play a significant role in ejection of the melt from the interaction zone even for low melt surface temperatures close to the melting point. High-velocity melt flow was generated in the interaction zone for beam intensities typically used in laser cutting/welding; thus, the melt-flow pattern could not be considered as the motion of a cylinder in an infinite liquid pool. Under typical industrial cutting/welding conditions about $70 - 90\%$ of laser intensity absorbed in the beam interaction zone was carried away from the interaction zone by the metal flow; thus, the convection-related terms could not be ignored neither in calculations of the energy balance in the interaction zone nor in calculations of the thermal field in the weld pool or in the vicinity of the cutting front. The velocity of the keyhole-wall front or cutting front was determined by the absorbed laser intensity and could be either smaller or higher than the beam's translation velocity.

Yilbas etal. [35] examined the laser heating mechanism initiatig the drilling process. The study included conduction and convection effects and assumed a steady-state evaporation process. This enabled estimation of the limits of the Fourier theory in laser drilling process. Using the model maximum temperature attained inside the material, nucleation, explosion process and drilling effeciency were predicted. Results obtained from this study for vapor front velocity were compared with experiment.

Yilbas and Al-Garni [37] developed a heat transfer model to cover some aspects of the interaction mechanism excluding liquid expulsion, nucleation and plasma ef-

fects. The development of the evaporation model provided basic information on the interaction process. Damage threshold intensities were predicted with the effects of the surface reflection process. They considered a steady-state condition first and obtained relationships between the absorbed power intensity, and the temperature and recession velocity.They extended this approach to time dependent case which proved extremely difficult to solve analytically. However, appropriate assumptions yielded estimates of the time for the surface temperature to reach 90% of its steady state value. They also made the measurement of surface temperature using an optical method. This provided the basis for comparision of the predicted and measured temperatures. They concluded that when using pulsed lasers in the laser drilling process, the spikes appearing in the pulse had frequencies of the order of $1 - 5\ MHz$, which allowed the thermal integration of the pulsed laser heating process. As the pulse heating progresses, the drilling velocity rised while the liquid depth and time to reach steady state fall; in this case, a greater proportion of the input energy went into evaporation as compared to conduction losses.

Yilbas [38] designed experiment to investigate the cutting parameters, which in turn provided improved cut quality, and to study the formation of strias through monitoring the light emission from the upper surface of the workpiece during the laser cutting process. To determine the critical cutting speed - at which cutting ceased - a variable-speed milling table was employed. This enabled the recording of power requirements at different cutting speeds and assisting gas velocities. To monitor the light emitted from the upper surface of the workpiece, a fiber-optic cable and a fast-response photodetector were used. He concluded that self-burning resulted

below a specific cutting speed and it increased with increasing oxygen pressure. Heat-spred from the cutting zone decreased at high cutting speeds, which in turn increased the temperature gradients in the kerf and diminished the tendency for oxidation to become locally self-sustaining. The critical cutting speed increased rapidly with oxygen pressure, providing that a further increase in oxygen pressure did not enhance the oxidation process, but increased the removal rate of molten matel from the cut. At the critical gas pressure (giving the maximum useful jet velocity), the cutting speed was almost independent of the workpiece thickness at high power intensities, which in turn indicated that only a relatively small part of the total laser power incident on the cut region was absorbed usefully.

Afanasiev etal. [40] studied the applicability of hydrodynamic models for the theoratical description of UV laser ablation of polymers. They considered the plume formation as a first-order like phase transition. This phase transition occured for strongly absorbing polymers as a bulk evaporation. The vapor plume was assumed to be transparent to laser radiation, and its expansion was described by the isoentropic hydrodynamic equations. They showed that for strongly absorbing polymers a good agreement with the available experimental data could be obtained if the adiabatic constant γ was assumed to be close to 1. This meant that the main energy of the ablation products was located in internal degrees of freedom. In this case a phase transition occured from the exited molecular states. This was a specific feature of cold UV laser ablation of strongly absorbing polymers. In this regime the etch depth per pulse had an approximately linear dependence on the laser fluence.They considered the UV laser ablation of weakly absorbing polymers as a result of bond breaking

because of a high thermal pressure in the absorbing layer.

Liu etal. [42] discussed the physics of ultrashort-pulse laser-matter interaction that lead to material breakdown and ablation. They emphasized the differences in ablation mechanisms between short and long pulses. They illustrated the generation, amplification and manipulation of subpicosecond pulses.

Pecharapa and Kar [43] developed a mathematical model to relate the weld depth and width to the laser parameters. The model was based on the Stefan condition for quasi-steady state laser welding. Simple experessions were obtained for the shapes of solid-liquid and liquid-vapour interfaces. They were found as functions of the laser irradiance, welding speed, absorptivity and thermal diffusivity. They also presented simple expressions for the temperature distributions in the liquid and solid phases. They gave the results for the weld depths and widths and the temperature distributions in the workpiece for various laser intensities and welding speeds. They found that the liquid-vapour and solid-liquid interfaces exhibited Gaussian like shapes. Their leading walls, which were in front of the laser beam in the welding direction, were steeper than their trailing walls. The maximum depths of these interfaces were slightly behind the laser beam center due to advection arising from the motion of the workpiece in the opposite direction to the scanning laser beam.The penetration depth and weld width were proportional to the powers of 0.67 and 0.33 of the laser power respectively and inversely proportional to the powers of 0.67 and 0.33 of the welding speed respectively.

Tahmouch etal. [44] investigated dismantling process with power lasers. They developed a new laser method and called it the laser dismantling process. The cutting

method used a high power laser at a long distance, without an assist gas, and with a focal length of the system of $1m$ to $10m$. Precision and accuracy in the process were not the same as for laser cutting for production and assembly. They indicated that cutting steel with a Nd:YAG laser beam at a long distance ($1m$), was possibl;e without an assist gas for thickness upto 2 cm. They also proved that, contrary to classical laser processing, much reduced power densities were necessary at the laser focal area for cutting. A much lower power density in the focal spot gave excellent results in laser dismantling.

Yilbas [45] investigated the mechanism that initiated the striation and developed a methematical model for this purpose. To achieve this goal, he intoduced the heat transfer equation employing a moving heat source and allowing a high temperature exothermic reaction due to an assisting gas jet. This made it possible to predict the maximum cut width, penetration speed and length of striation. The kerf width expansion due to melting and sideways burning were predicted for the area ratio of melted zone to focused spot. This also permitted the striation frequency to be computed. He also included experimental investigation into a striation process. He concluded that the predicted kerf width agreed well with the experimentally obtained results and the model developed for the area ratio produced realistic values for the striation width. Sideways burning, liquid layer oscillation at the surface and variation in the absorbed power due to surface plasma were the main reasons for the striation.

Dimensional variation in laser cutting of sheet metals depends on two factors: the accuracy and repeatability of the positioning system and the thermal effects of the laser beam on workpiece material. Molian etal. [47] formulated a physical

model to estimate the dimensional accuracy of holes produced with laser cutting. They included the assumption in their model that the layer adjacent to the hole was plastically deformed and contained residual stresses up to the yield strength. The model was used to calculate the size of the hole and cut-out disk of varying radii in steel plates with thicknesses of 3.2 mm and 6.4 mm. They verified the predictions with experimental data abtained using a 1 kW continuous wave CO_2 laser. Results indicated that there was an excellent correlation between the model and the experimental data especially for smaller diameter holes. The kerf width was found to be a major factor in achieving high dimensional accuracy compared with thermal deformation, and any effects leading to a smaller kerf would substantially improve the accuracy. The results also indicated that for thicker metals a model that considered heat flow in all three directions would provide better results.

Liu etal. [50] described a combined theoratical and experimental effort to model various physical process during laser ablation of solids using a variety of computational techniques. They focused their modeling on following areas: (a) rapid transformations through the liquid and vapor phase under possibly nonequilibrium thermodynamic conditions induced by laser solid interactions; (b) breakdown of the vapor into a plasma in the early stages of ablation through both electronic and photoionization processes; (c) hydrodynamic behavior of the vapor/plasma during and after ablation; and (d) the efects of initial conditions in the vapor, in particular, the nature of the initial velocity distribution, on the characteristics of subsequent vapor expansion They found that laser annealing phenomena could be modeled by1-D and 2-D thermal models with realistic treatments of nonequilibrium thermodynamic phase transforma-

tions. Electronic and photoelectric processes might be necessary for modeling of vapor breakdown. Breakdown time predicted based on simple kinetic model was qualitatively consistent with experimental observation. Their modeling of vapor expansion and transport revealed the following phenomena: formation and propagation of shock waves, shock heating and ionization, confinement of plasma by a background gas.

Black etal. [52] studied the cutting of commercially-available ceramic tiles using a CO_2 laser cutting machine, with the object of producing a laser beam machining (LBM) database that contained the essential parameter information for their successful processing. They investigated various cutting parameters that would generate a cut in a ceramic tile which required minimal post-treatment. They also examined the effects of various sheild gases, of multi-pass cutting and of underwater cutting.

Yilbas etal. [54] carried out a study to investigate the material response to the repetitive laser pulsed heating process. A three-dimensional heating model was developed using an electron kinetic theory approach. The phase change processes were included and the laser beam was considered to scan the workpiece surface with a constant speed. They introduced a numerical method using an explicit scheme to solve the governing equations. Semi-infinite steel was considered as the workpiece material. The repetitive pulses with constant intensity ratio, which was the ratio of repetitive pulse intensity to the first pulse intensity, and constant repetition rate were considered. To examine the influence of intensity ratio on the resulting temperature profiles, they employed three intensity ratios. They concluded that the temperature profiles at the surface and in the vicinity were influenced considerably by the laser intensity distribution. The rate of evaporation increased in the surface vicinity while

the internal energy gain of the evaporating molecules increased at the surface. In this case, the energy transferred to the substrate, due to mlecular collisions, was not substantiated as resulting in less depth of evaporting zone. The depth of heated liquid zone increased as the local power intensity available at the surface reduced. The point of initiation of liquid heating in the substrate did not strongly depend on the power intensity distribution across the irradiated spot. As the repetitive pulse heating progresses, the point of initiation of liquid heating moved close to the surface while the depth of the heated liquid zone reduced.

Yilbas [55] performed experimental study to describe the characteristics of liquid ejection through a trapping mechanism in a way that preserved their ejection form. To achieve this, the experiment was conducted in such a manner as to monitor the material ejected in the form of discrete particles and where possible to relate these characteristics to the basic parameters of the interaction, namely target material, pulse energy, and beam waist position relative to the target. He extended the study to include a streak photography of ejected particles. He concluded that three distinguishable type of ejected material could be identified. The large slab particles, which were not ejected frequently, had a size of about 250 μm. The reason for slab ejection was not clearly known. The medium size particles, such as granules were ejected from all the workpiece materials. The third type of particles ejected was whiskers with a nominal diameter of $15 - 20$ μm. The source of whiskers might be be the liquid material swept from the cavity walls due to the flushing action of high-pressure gradients and rapidly expanding vapors.

Thermal Stress Development in Laser Heating

Analytical Solution

Paek and Gagliano [64] developed a model that used a continuous, distributed and moving heat source to describe the temperature profile and thermal stress propagation for laser drilled holes. Thermal stress could be induced in the material due to the temperature distribution and would be menifested when an element of the body was not allowed to expand freely. Specifically, in the case of a large temperature gradient, one could expect high stresses, which might exceed the fracture limit of the material. They used plain strain case to model the stresses. Their theory indicated that shorter pulse lengths generally resulted in lower stresses. Longer pulses generated higher stresses simply because the heat penetrated or diffused further into the material. Since the magnitude of the stress was governed essentially by the temperature profile, it was seen that the desireable condition for hole drilling was to maintain a suffeciently high beam intensity for a minimum time to remove (theoratically by sublimation) a given mass of material.

Elperin and Rudin [67] determined an analytical solution of a two-dimensional thermoelasticity problem for a thin coating attached to a substrate. They treated the coating as a statified multilayer structure composed of layers with varying thermophysical and optical characteristics. They developed a mathematical procedure of solution based on expansion of Laplace and Hankel transforms of temperature, displacement and strain distributions in series of small parameter which was equal to the ratio of a coating thickness to a laser beam radius. Expressions for determination of the two-dimensional nonstationary temperature, strain and stress distributions in

a multilayer assembly were derived in a closed analytical form.

Yilbas etal. [70] computed the temperature field and the resulting thermal stress developed in the direction normal to the workpiece surface. To investigate the effect of laser pulse length on the resulting thermal stresses, three pulse lengths were introduced. The closed-form solution for a step input pulse heating was introduced to compute the temperature profiles. To validate the theoratical predictions an experiment was conducted to measure the surface temperature. Moreover, microscopic study of laser-heated surfacees was conducted and the possible microcracks due to thermal stresses were identified. The temperature profiles predicted from the different pulses indicated that the short pulse length results in high temperature rise in the surface vicinity. In this case, considerable thermal stress developed in this region. Moreover, the thermal stress increased further in magnotude as the heating progressed. This might be due to attainment of the high temperature gradient at high heating times. It was evident from experimental study that very fine-grained structure occured, which was of essentially fine autenite contributing to high hardness. It was observed that martensite structure became gradually coarser due to austenite grain growth as the distance from the surface increased. Due to high degree of thermal stress formation, microcracks appeared on the surface of the heated region. The direction of the cracks formed was arbitrary, therefore, non-uniform heating resulted in non-uniform thermal stress formation on the workpiece surface.

Numerical Simulations

Wang etal. [68] proposed a new costitutive equation considering the effects of phase transformation and the complex coupling action between temperature, phase

transformation. The stress field was analyzed, introducing the elastoplastic theory and phase transformation. Under the circumstances of temperature and yield condition given, the results of numerical calculations showed that residual stresses were formed on the surface of a laser quenched workpiece.

Dain etal. [71] evaluated the stresses along the weld direction and the distortion of the unwelded open end resulting from the welding process using a Mellin-transformation technique. The final result for an infinte plate was expressed in terms of a convolution integral. The effect of the transient change in gap was analysed both analytically and numerically. The result showed that the welding procedure had a large influence on the formation of the thermoelastic mismatch of the unwelded edges. The analytical expression for the gap width was compared with FEM simulations of finite rectangular plates with various forms of clamping. The theoretically calculated mismatch of the unwelded edges fall within the range between values of the mismatch for free and rigidly fixed rectangular plates.

Yilbas etal. [72] investigated the thermal stresses formed during the gas-assisted pulsed laser heating process. The gas-assisted laser heating of a steel substrate was modeled by considering a two-dimensional axisymmetric case with gas jet impengement. In the analysis, conjugate heat transfer conditions were employed and a low Reynolds number $k-\epsilon$ model was introduced to account for the turbulence. Thermal stresses developed during the laser heating and cooling cycles were predicted with axisymmetric stress model. They concluded that the impinging gas jet presure in the surface vicinity of the workpiece had no effect on the thermal stresses developed in substrate. The radial stress distribution extended inside the substrate as the heating

progressed. This was more pronounced in cooling cycle provided that the magnitude of the stress reduced considerably as the cooling period progressed. The axial stress was tensile and its value was zero at the free surface. It was highly concentrated in the region close to the surface in the early heating times. The magnitude of the axial stress was smaller than that of the radial stress. As the heating progressed, the axial stress extended inside the workpiece similarly to the radial stress behavior. The von-Mises stress attained its maximum value below the surface. The location of the maximum von-Mises stress remained the same in the substrate during the heating cycle. This changed in the cooling cycle, so that the location of the maximum stress moved away from the surface as the cooling period increased.

Experimental Investigations

Arnet and Vollertsen [65] studied laser bending mechanism in which thermal residual stresses generated by a laser beam was used to bend the sheet metal. Previously bending was only possible towards the beam, they showed that one could also achieve bending away from the beam. Based on thier experimental results they explained the instability in bending process and outlined the factors influncing the bending in any predominant direction.

Li and Sheng [66] presented an experimental and numerical study of fracture initiation in thin aluminium oxide ceramics during laser cutting. Fracture criteria was based on the maximum tensile and maimum compressive stress. In the experiments, alumina plates with thickness of 0.8 mm were cut at cutting speeds of $1.3 - 152$ mm/sec by continuous-wave CO_2 laser with power rating from 200 to 700 W. Criteria for fracture initiation were correlated with laser power and cutting speed. A hybrid

method for modeling fracture initiation was introduced whereby the kerf width was determined through an analytical solution and the temperature and stress distribution were found through a numerical plane stress model. Temperature dependence of material properties was incorporated in the model. Effect of cutting speed and laser power on the fracture initiation was analyzed quantatively and good agreement was obtained between experiment and the numerical simulation. The results showed that avoidance of fracture initiation resulted from a high energy density cutting condition (high laser power and low cutting speed).

Yau etal. [69] investigated the laser bending of thin sheets using low power laser beams. They used a machine vision system to measure bending angles. The result showed that the final bending angle in a multiple irradiation laser bending process was related strongly to the laser power, the processing velocity, the number of irradiations and the holding time between each laser irradiation.

Chapter 3

MATHEMATICAL MODELING

3.1 Mathematical Analysis of Heating Process

When a laser workpiece interaction time is comparable to the thermalization time of the substrate material ($\sim 10^{-12}$ s), the non-equilibrium energy transport dominates the heating process. In this case, electron temperature well excess of lattice site temperature occurs [73]. The Fourier heating model over estimates the lattice site temperature rise during the short interaction period. However, as the duration of heating extends to nanoseconds, the equilibrium energy transport occurs inside the metallic substrates during the heating period. Consequently, electron and lattice site temperatures become identical [19]. Therefore, the Fourier heating model becomes appropriate to describe the physical process that takes place during the nanosecond heating durations.

3.1.1 Analysis of Conduction Limited Heating Process

In conduction limited heating laser intensity is kept within certain limits so that the temperature of the substrate material remains below melting point. The following assumptions are made to model the conduction limited heating:

- Substrate material and laser both are stationary this gives rise to axisymmetric

heating, as shown schematically in Figure 3.1.

- Solid is isotropic therefore constant material properties could be considered. However, temperature dependent thermal properties are also considered in some cases simulated.
- Material has certain absorption depth for the laser radiation.
- Laser beam is absorbed in the solid and acted as a heat source.
- There is no heat losses from surface due to convection or radiation i.e. insulated surface boundary condition is assumed.
- Laser beam intensity has Gaussian distribution.
- Substrate material is assumed to be semi-infinite.

The transient diffusion equation governing the conduction limited heating process for constant property case can be written in the axisymmetric coordinates in the light of the above assumptions as:

$$\rho c_p \frac{\partial T}{\partial t} = k \left[\frac{1}{r} \frac{\partial}{\partial r} \left(\frac{\partial T}{\partial r} \right) + \frac{\partial^2 T}{\partial z^2} \right] + S_o \tag{3.1}$$

Where S_o is:

$$S_o = I_o \delta \left(1 - r_f\right) \exp\left(-\delta z\right) \exp\left(-\frac{r^2}{a^2}\right)$$

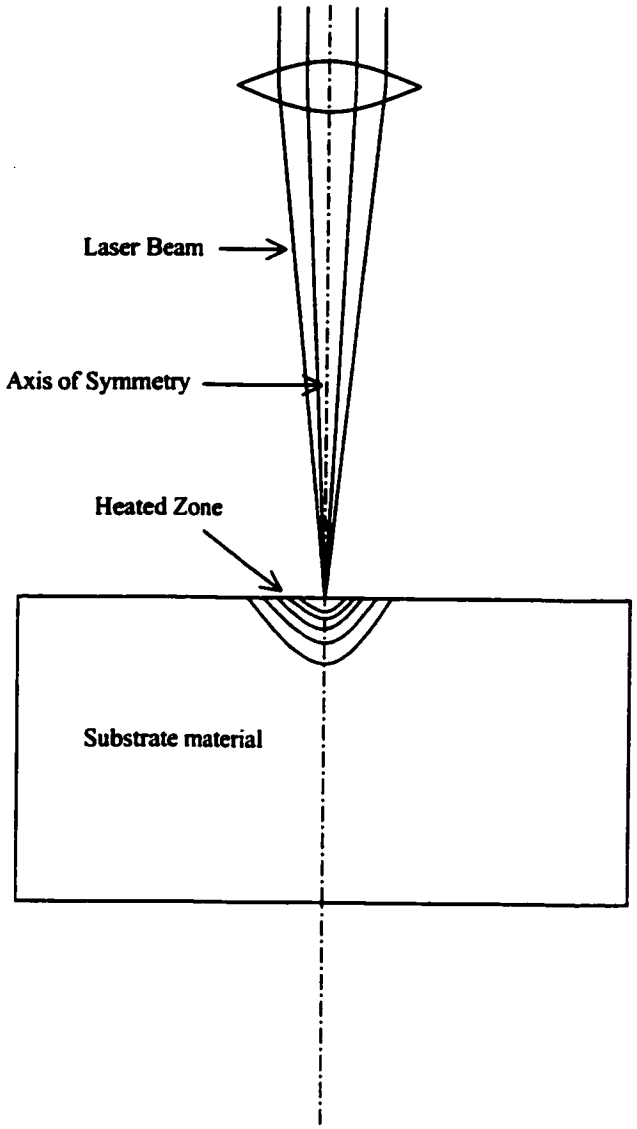

Figure 3.1: Schematic view of laser heating of substrate material.

Where

r_f = surface reflectivity

I_o = peak laser intensity

δ = Absorption depth

a = Gaussian parameter

The corresponding boundary conditions are,

$$\begin{aligned} \frac{\partial T}{\partial z} &= 0 \quad at \;\; z = 0 \quad \text{(surface)} \\ \frac{\partial T}{\partial r} &= 0 \quad at \;\; r = 0 \quad \text{(axis of symmetry)} \\ T &= T_o \quad \text{(Specified)} \quad at \;\; r, z \rightarrow \infty \quad \text{(faraway)} \end{aligned}$$

Also initial condition is

$$T = T_o \quad \text{(Specified)} \quad at \;\; t = 0 \;\; \text{(initially)}$$

Equation (3.1) can be non-dimensionlized through introducing the following dimensionless parameters:

$$\begin{aligned} r^* &= r\delta \\ z^* &= z\delta \\ a^* &= a\delta \\ t^* &= \alpha\delta^2 t \\ T^* &= \frac{Tk\delta}{I_o(1-r_f)} \end{aligned}$$

After introducing the dimensionless parameters, equation (3.1) for constant properties yield:

$$\frac{\partial T^*}{\partial t^*} = \frac{1}{r^*}\frac{\partial}{\partial r^*}\left(r^*\frac{\partial T^*}{\partial r^*}\right) + \frac{\partial^2 T^*}{\partial z^{*2}} + \exp(-z^*)\exp\left(-\frac{r^{*2}}{a^{*2}}\right) \tag{3.2}$$

Non-dimensional boundary conditions take the form as:

$$\begin{aligned}
\frac{\partial T^*}{\partial z^*} &= 0 \quad at \;\; z^* = 0 \;\; \text{(surface)} \\
\frac{\partial T^*}{\partial r^*} &= 0 \quad at \;\; r^* = 0 \;\; \text{(axis of symmetry)} \\
T^* &= \frac{T_o k\delta}{I_o(1-r_f)} \quad \text{(Specified)} \quad at \;\; r^*, z^* \to \infty \;\; \text{(faraway)}
\end{aligned}$$

Non-dimensional initial condition is,

$$T^* = \frac{T_o k\delta}{I_o(1-r_f)} \quad \text{(Specified)} \quad at \;\; t^* = 0 \;\; \text{(initially)}$$

By solving equation (3.2) with the boundary conditions, we can obtain temperature field at any instant of time. Since analytical solution of this equation is almost impossible, therefore, we apply a numerical solution using the control volume approach.

In case of variable properties, equation(3.1) yields:

$$\frac{\partial}{\partial t}(\rho c_p T) = \frac{1}{r}\frac{\partial}{\partial r}\left(k\frac{\partial T}{\partial r}\right) + \frac{\partial}{\partial z}\left(k\frac{\partial T}{\partial z}\right) + S_o \tag{3.3}$$

It should be noted that in the case of variable properties equation (3.3) is non-dimensionalized using a reference values of thermal properties i.e. thermal properties

at 25^oC.

3.1.2 Analysis of Non-Conduction Limited Heating Process

The case of non-conduction limited heating process involve phase change i.e. melting of substrate material, and if enough energy is being supplied then subsequent evaporation. The modeling of phase change problem is inherently difficult because the interface between the solid and liquid or liquid and gas phase is moving as the energy equivalent to the latent heat is absorbed; as a result, the location of the solid-liquid or liquid-gas interface is not known a priori. Standard models to describe the phase change problem are Stefan problem and Enthalpy method [74]. To model this problem we are using a third method which is a slight variation of enthalpy method. Following assumptions are made in the modeling of phase change process in addition to those mentioned for the conduction limited case;

- For solid and liquid phases have same absorption coefficient during phase change process.
- Laser beam is absorbed by liquid or solid phasees and generating a heat source.
- When solid start vaporizing the resulting gas does not interact with laser beam and liquid-gas interface start moving inside the material with a recession velocity creating a cavity.
- There is no ionization of emerging gas front.
- Inside the cavity formed there is no multiple reflection phenomena, and we are

assuming negligible or zero reflectance from surface of cavity.

- Radiation/Convection losses from the cavity is omitted, since it is negligibly smaller as compared to internal energy gain of the substrate material.
- Substrate material is a pure substance with single melting and evaporation temperature.
- Prior to evaporation there is no heat loss from surface due to convection or radiation thus we can take insulated boundary condition, at the surface.
- At the points where temeperature reaches to evaporation we set a boundary with fixed temperature equal to the evaporation temperature of the substrate material and this boundry moves with gas-liquid interface.
- Vapor region has no interaction with substrate material.
- There is no recondensation of vapors in cavity and vapor temperature is kept at the boiling temperature of the substrate material.
- Pulse could be both step input or time exponentially varying.

In the analysis, a Gaussian power intensity distribution of a laser beam with its spot center at the center of the co-ordinate system is considered. When the temperature reaches the phase change temperatures of the substrate material (melting and evaporation temperatures) during the heating process, the phase change is considered i.e. melting and subsequent evaporation of solid substrate are introduced in the governing equation of heat transport with appropriate boundary conditions. The

conduction heating of the solid substrate with insulated boundary condition at the surface is considered. The transient heat transfer equation for a solid substrate at constant properties irradiated by a laser beam with a Gaussian intensity profile can be written as:

$$\rho_s c_{p_s} \frac{\partial T}{\partial t} = \frac{k_s}{r} \frac{\partial}{\partial r} \left(r \frac{\partial T}{\partial r} \right) + k_s \frac{\partial^2 T}{\partial z^2} + S_o \tag{3.4}$$

where for step-input pulse,

$$S_o = I_o \delta \left(1 - r_f\right) \exp\left(-\delta z\right) \exp\left(-\frac{r^2}{a^2}\right)$$

Here, I_o, δ, r_f, and a are the power intensity, absorption depth and the Gaussian parameter, respectively. For the case of exponentially time decaying pulse

$$S_o = I_o \delta \left(1 - r_f\right) \left[\exp(-\beta t) - \exp(-\gamma t)\right] \exp\left(-\delta z\right) \exp\left(-\frac{r^2}{a^2}\right)$$

β and γ are time exponentially varying pulse parameters.

The initial condition is:

$$T = T_o \quad \text{(Specified)} \quad at \;\; t = 0 \;\; \text{(initially)}$$

The boundary conditions are:

$$\frac{\partial T}{\partial z} = 0 \quad at \ z = 0 \quad \text{(surface)}$$
$$\frac{\partial T}{\partial r} = 0 \quad at \ r = 0 \quad \text{(axis of symmetry)}$$
$$T = T_o \quad \text{(Specified)} \quad at \ r, z \rightarrow \infty \quad \text{(faraway)}$$

In case of variable properties equation (3.4) becomes similar to equation (3.3).

When the phase change process take place, it is assumed that the substrate material has single melting and evaporation temperatures, i.e., when the substrate material reaches the melting or evaporation temperatures, the phase change takes place at a constant temperature. To describe the energy transfer during a phase change process,enthalpy method can be used. In the case of enthalpy method, the governing equation of energy transport can be written in terms of enthalpy equation [74]. Moreover, once the phase change occurs, a mushy zone (partially solid and partially liquid or partially liquid and partially vapor) is generated across the region where the phase change takes place (Figure 3.2). Consequently, when formulating the phase change problem, the consideration is given for the generation of a mushy zone. In this case, during the phase change process, temperature of the substrate material remains same, but it's enthalpy changes. In order to formulate the problem the following approach is introduced, namely energy method. Consider a differential element in a substrate material (Figure 3.2), which is subjected to a melting process and let x_m is the mass fraction of liquid present in the element, then the energy content (ΔU) of the differential element with volume ΔV at melting temperature T_m can be written

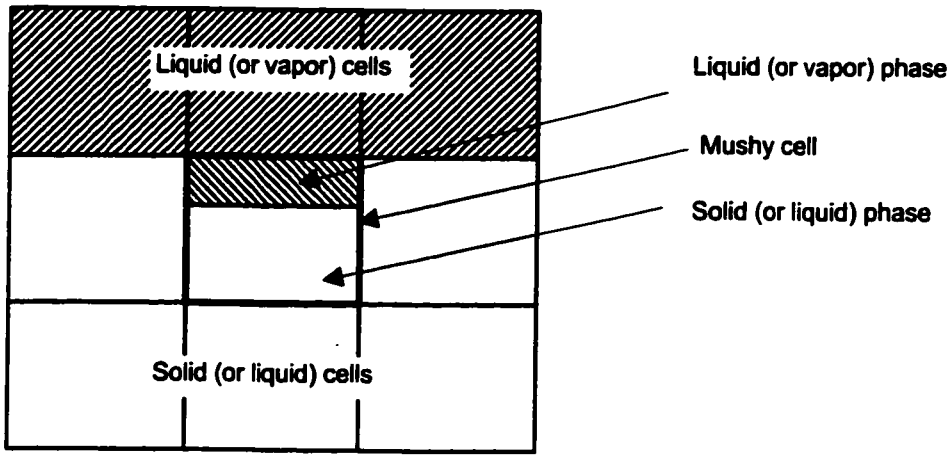

Figure 3.2: Schematic view of a mushy cell.

as:

$$\Delta U = \rho_m \Delta V \left[x_m \left(L_m + c_{p_m} \left(T_m - T_{ref} \right) \right) + c_{p_s} \left(1 - x_m \right) \left(T_m - T_{ref} \right) \right]$$

where

$$x_m = \frac{m_m}{m_m + m_s}$$

Here, T_{ref}, x_m, m_m, m_s are reference temperature for enthalpy, quality of liquid, mass of liquid and mass of solid in the element, respectively. After assuming that specific heat of melt is the same as solid at melting temperature ($Cp_s = Cp_m$ at $T = T_m$), then above equation reduces to:

$$\Delta U = \rho_m \Delta V \left[x_m L_m + c_{p_m} \left(T_m - T_{ref} \right) \right]$$

For a unit volume, it reduces to:

$$\frac{\Delta U}{\Delta V} = \Delta u = \rho_m \left[x_m L_m + c_{p_m} \left(T_m - T_{ref} \right) \right]$$

Differentiation with time yields:

$$\frac{\partial u}{\partial t} = \rho_m L_m \frac{\partial x_m}{\partial t} \tag{3.5}$$

since $c_{p_m} \left(T_m - T_{ref} \right) = \text{const.}$

It is important to note that in conduction equation (3.4) $\rho_s c_{p_s} T$ is also the enthalpy per unit volume i.e.

$$\rho_s c_{p_s} \frac{\partial T}{\partial t} = \frac{\partial u}{\partial t}$$

Substituting equation (3.5) into equation (3.4) gives the energy equation for the differential element subjected to the phase change process (melting):

$$\rho_m L_m \frac{\partial x_m}{\partial t} = \frac{k_m}{r} \frac{\partial}{\partial r} \left(r \frac{\partial T}{\partial r} \right) + k_m \frac{\partial^2 T}{\partial z^2} + S_o \tag{3.6}$$

Equation (3.6) is applicable for the differential elements (cells defined by nodes in the substrate material) when temperature becomes melting temperature of the substrate material ($T = T_m$) and $0 \leq x_m \leq 1$, i.e., a mushy zone. Consequently, here temperature of the cells with $0 \leq x_m \leq 1$ is set to melting temperature ($T = T_m$). When the value of x_m exceeds 1 ($x_m > 1$) equation (3.6) is not applicable for the differential element under consideration. In this case, equation (3.4) is used to determine the temperature rise in the liquid heating with the liquid thermal properties employed, i.e., the liquid heating initiates and continues till the temperature reaches the evaporation temperature. It is important to note that inside mushy region terms like $\frac{\partial T}{\partial r}$ and $\frac{\partial T}{\partial z}$ are zero, because temperature is constant, but equation (3.6) is valid at mushy zone/solid and mushy zone/liquid interfaces where these terms are not generally zero.

In the case if the temperature reaches the evaporation temperature, the mushy zone consideration needs to be implemented. In this case, equation (3.6) can be

modified for a differential element, which is subjected to the evaporation, i.e.:

$$\rho_b L_b \frac{\partial x_b}{\partial t} = \frac{k_b}{r}\frac{\partial}{\partial r}\left(r\frac{\partial T}{\partial r}\right) + k_b\frac{\partial^2 T}{\partial z^2} + S_o \tag{3.7}$$

Equation (3.7) is applicable for the range $T = T_b$ and $0 \leq x_b \leq 1$ in the mushy zone (partially liquid partially vapor zone). Consequently, temperature of the cells with $0 \leq x_b \leq 1$ is set to boiling temperature ($T = T_b$). It should be noted that x_m is replaced with x_b, which represents the fraction of vapor phase in the differential element.

In the case of variable properties equations (3.6) and (3.7) yields:

$$\rho_m L_m \frac{\partial x_m}{\partial t} = \frac{1}{r}\frac{\partial}{\partial r}\left(k_m\left(r\frac{\partial T}{\partial r}\right)\right) + \frac{\partial}{\partial z}\left(k_m\frac{\partial T}{\partial z}\right) + S_o \tag{3.8}$$

and,

$$\rho_b L_b \frac{\partial x_b}{\partial t} = \frac{1}{r}\frac{\partial}{\partial r}\left(k_b\left(r\frac{\partial T}{\partial r}\right)\right) + \frac{\partial}{\partial z}\left(k_b\frac{\partial T}{\partial z}\right) + S_o \tag{3.9}$$

It should be noted that ρ_b, L_b, ρ_m and L_m are considered as constants.

The boundary condition at the evaporating surface is introduced in relation to equation (3.7). In this case, the temperature along the evaporated surface is kept at boiling temperature, i.e., the cells in the evaporated region are kept at boiling temperature:

$$At \;\; z = z_b, r = r_b \rightarrow T(r_b, z_b, t) = T_b$$

where z_b and r_b represent the axial and radial location at the evaporated surface.

Equations (3.6) and (3.7) determine the relative position of solid-liquid and liquid-vapor interface in the substrate material. Liquid-vapor interface determines the shape and size of cavity generated after evaporation process.

Equations (3.4), (3.6), and (3.7) can be non-dimensionlized through introducing the following dimensionless parameters:

$$\begin{aligned} r^* &= r\delta \\ z^* &= z\delta \\ a^* &= a\delta \\ t^* &= \alpha\delta^2 t \\ T^* &= \frac{Tk_o\delta}{I_o(1-r_f)} \end{aligned}$$

where k_o represents the thermal conductivity at standard temperature. After introducing the dimensionless parameters, equations (3.4), (3.6) and (3.7) yield:

$$\frac{\partial T^*}{\partial t^*} = \frac{1}{r^*}\frac{\partial}{\partial r^*}\left(r^*\frac{\partial T^*}{\partial r^*}\right) + \frac{\partial^2 T^*}{\partial z^{*2}} + \exp(-z^*)\exp\left(-\frac{r^{*2}}{a^{*2}}\right) \tag{3.10}$$

$$\frac{\alpha_m\delta\rho_m L_m}{I_o}\frac{\partial x_m}{\partial t^*} = \frac{1}{r^*}\frac{\partial}{\partial r^*}\left(r^*\frac{\partial T^*}{\partial r^*}\right) + \frac{\partial^2 T^*}{\partial z^{*2}} + \exp(-z^*)\exp\left(-\frac{r^{*2}}{a^{*2}}\right) \tag{3.11}$$

$$\frac{\alpha_b \delta \rho_b L_b}{I_o} \frac{\partial x_b}{\partial t^*} = \frac{1}{r^*} \frac{\partial}{\partial r^*} \left(r^* \frac{\partial T^*}{\partial r^*} \right) + \frac{\partial^2 T^*}{\partial z^{*2}} + \exp(-z^*) \exp\left(-\frac{r^{*2}}{a^{*2}} \right) \tag{3.12}$$

In the case of variable properties equations (3.8) and (3.9) are non-dimensionalized with reference to thermal properties at $25°C$.

The non-dimensional initial condition for equations (3.10), (3.11), and (3.12) are:

$$T^* = \frac{T_o k \delta}{I_o (1 - r_f)} \quad \text{(Specified)} \quad at \;\; t^* = 0 \;\; \text{(initially)}$$

The non-dimensional boundary conditions are:

$$\begin{aligned}
\frac{\partial T^*}{\partial z^*} &= 0 \quad at \;\; z^* = 0 \;\; \text{(surface)} \\
\frac{\partial T^*}{\partial r^*} &= 0 \quad at \;\; r^* = 0 \;\; \text{(axis of symmetry)} \\
T^* &= \frac{T_o k \delta}{I_o (1 - r_f)} \quad \text{(Specified)} \quad at \;\; r^*, z^* \to \infty \;\; \text{(faraway)}
\end{aligned}$$

Temperature distribution inside the substrate material is obtained by solving the equations (3.10), (3.11), and (3.12) with the appropriate boundary conditions. The numerical solutions of equations (3.10), (3.11), and (3.12) are tested using an enthalpy method.

3.2 Enthalpy Method

Enthalpy form of energy equation is given by

$$\rho \frac{\partial H(T)}{\partial t} = \nabla \cdot (k \nabla T) + S_o \tag{3.13}$$

or in axisymmetric coordinates with source term as applicable to present study,

$$\rho\frac{\partial H(T)}{\partial t} = \frac{k}{r}\frac{\partial}{\partial r}\left(r\frac{\partial T}{\partial r}\right) + k\frac{\partial^2 T}{\partial z^2} + S_o \tag{3.14}$$

for step input pulse,

$$S_o = I_o\delta(1-r_f)\exp(-\delta z)\exp\left(-\frac{r^2}{a^2}\right)$$

or for time exponentially decaying pulse,

$$S_o = I_o\delta(1-r_f)\left[\exp(-\beta t) - \exp(-\gamma t)\right]\exp(-\delta z)\exp\left(-\frac{r^2}{a^2}\right)$$

Equations (3.13) and (3.14) are equivalent to the usual temperature form in which the heat conduction equation is written separately for the liquid and solid regions and coupled with the energy balance equation and temperature continuity at the solid-liquid interface. Therefore the enthalpy method is applicable for the solution of phase-change problems involving both a distinct phase change at a discrete temperature as well as phase change taking place over an extended range of temperatures e.g. in non-eutectic alloys.

Also for our case where we are assuming a single phase change temperature T_m for solid to liquid change and T_b for liquid to vapor change, we have relationship between enthalpy and temperature as,

$$T = \begin{cases} \frac{H}{c_p} & H < c_p T_m \\ T_m & c_p T_m < H < (c_p T_m + L_m) \\ \frac{H - L_m}{c_p} & (c_p T_m + L_m) < H < c_p T_b \end{cases}$$

Same boundary and initial conditions are applicable here as with equation (3.4). It is important to note that this method is only to model solid to liquid or liquid to solid phase change.

3.3 Analysis of Thermal Stress

The equation governing the thermal stresses due to laser pulse heating can be written through stress-strain relations. Assuming no external mechanical stresses acting on the surface of the substrate material, in cylindrical co-ordinates, these relations can be written as [75]:

$$\varepsilon_r = \frac{1}{E}\left[\sigma_r - \nu\left(\sigma_\theta + \sigma_z\right)\right] + \alpha_T T \tag{3.15}$$

$$\varepsilon_\theta = \frac{1}{E}\left[\sigma_\theta - \nu\left(\sigma_r + \sigma_z\right)\right] + \alpha_T T \tag{3.16}$$

$$\varepsilon_z = \frac{1}{E}\left[\sigma_z - \nu\left(\sigma_r + \sigma_\theta\right)\right] + \alpha_T T \tag{3.17}$$

where E, ν, and α_T are elastic module, Poisson's ratio, and thermal expansion coefficient, respectively.

The stress function (φ) can be defined when formulating the thermal stresses [75], i.e:

$$\sigma_r = \frac{\varphi}{r} \tag{3.18}$$

$$\sigma_\theta = \frac{d\varphi}{dr} \tag{3.19}$$

In case of plane strain, strain in the z-axis reduces to $\varepsilon_z = 0$ and σ_z can be determined from equation (3.17), i.e.:

$$\sigma_z = \nu\left(\sigma_r + \sigma_\theta\right) - \alpha_T E T \tag{3.20}$$

The compatibility equation for the rotationally symmetric case is [64]:

$$r\left(\frac{d\varepsilon_\theta}{dr}\right) + \varepsilon_\theta - \varepsilon_r = 0 \tag{3.21}$$

Substituting equations (3.15)-(3.20) into equation (3.21), the following is results obtained:

$$\frac{d^2\varphi}{dr^2} + \frac{1}{r}\frac{d\varphi}{dr} - \frac{\varphi}{r^2} = -\frac{\alpha_T E}{1-\nu}\frac{dT}{dr} \tag{3.22}$$

Integration of equation (3.22) yields:

$$\varphi = -\left(\frac{\alpha_T E}{1-\nu}\right)\frac{1}{r}\int_{r_g}^{r} Trdr + \frac{C_1 r}{2} + \frac{C_2}{r} \tag{3.23}$$

since $\sigma_r = \frac{\varphi}{r}$, then σ_r becomes:

$$\sigma_r = -\left(\frac{\alpha_T E}{1-\nu}\right)\frac{1}{r^2}\int_{r_g}^{r} Trdr + \frac{C_1}{2} + \frac{C_2}{r^2} \tag{3.24}$$

For the case of conduction limited heating the boundary conditions for σ_r are:

$$\frac{\partial \sigma_r}{\partial r} = 0 \quad at \quad r = r_g = 0 \quad \text{(axis of symmetry)}$$

$$\sigma_r = 0 \quad at \quad r \to \infty \quad \text{(faraway)}$$

For the case of non-conduction limited heating the boundary conditions for σ_r are:

$$\sigma_r = 0 \quad at \quad r = r_g \quad \text{(at solid liquid interface)}$$

$$\sigma_r = 0 \quad at \quad r \to \infty \quad \text{(faraway)}$$

Introducing the boundary conditions into equation (3.24) for both cases i.e. conduction limited and non-conduction limited heating, the coefficients C_1 and C_2 becomes zero, i.e.

$C_1 = 0$ and $C_2 = 0$. Hence equation (3.24) reduces to:

$$\sigma_r = -\left(\frac{\alpha_T E}{1-\nu}\right)\frac{1}{r^2}\int_{r_g}^{r} Trdr \tag{3.25}$$

From equations (3.19) and (3.23) we get:

$$\sigma_\theta = -\left(\frac{\alpha_T E}{1-\nu}\right)\frac{1}{r^2}[\int_{r_g}^{r} Trdr - Tr^2] \tag{3.26}$$

and equation (3.20) gives:

$$\sigma_z = -\left(\frac{\alpha_T E}{1-\nu}\right)T \tag{3.27}$$

Introducing the dimensionless stress as:

$$\sigma^* = \sigma\left[\frac{1-\nu}{\alpha_T E}\right]\left[\frac{k_o\delta}{I_o(1-r_f)}\right]$$

The dimensionless thermal stresses becomes:

$$\sigma_r^* = -\frac{1}{r^{*2}}\int_{r_g^*}^{r^*} T^* r^* dr^* \tag{3.28}$$

$$\sigma_\theta^* = \frac{1}{r^{*2}}[\int_{r_g^*}^{r^*} T^* r^* dr^* - T^* r^{*2}] \tag{3.29}$$

$$\sigma_z^* = -T^* \tag{3.30}$$

The equivalent stress can be written as [75]

$$\sigma_e = \sqrt{\frac{1}{2}\left[(\sigma_r - \sigma_\theta)^2 + (\sigma_r - \sigma_z)^2 + (\sigma_z - \sigma_\theta)^2\right]} \tag{3.31}$$

or in the dimensionless form as:

$$\sigma_e^* = \sqrt{\frac{1}{2}\left[(\sigma_r^* - \sigma_\theta^*)^2 + (\sigma_r^* - \sigma_z^*)^2 + (\sigma_z^* - \sigma_\theta^*)^2\right]} \tag{3.32}$$

It should be noted that thermo-mechanical coupling between the temperature and stress fields is omitted, since it is reported to be negligibly small [75].

Chapter 4

NUMERICAL METHOD and ALGORITHM

4.1 Introduction

In the previous chapter we described the models for conduction limited and non-conduction limited heating. These models result in parabolic partial differential equations in two dimensions. These equations do not yield an analytical solution due to mathematical complexities involved and hence some other method of solution is required. To solve these equations numerical methods could be employed, which are able to handle almost any problem of any degree of complexity. A preliminary idea about the task of a numerical method can be obtained by considering a heat flow situation. A grid is drawn to cover the whole domain. With a suffeciently fine grid, the complete distributions of the temperature can be expressed in terms of their values at the grid points. Thus, the task of the numerical method is to evaluate temperature at each grid points. In numerical scheme, we derive a set of algebraic equations from governing differential equation for the grid-point values of the temperature. The detail and accuracy of the answer obtained depends mainly upon the proper selection of nodes and time increments. Hence, in developing a numerical scheme, the primary

consideration is a trade-off between model detail and computational effort.

4.2 Numerical Method

Several techniques of numerical analysis exist. Among them most famous are finite difference, finite volume, finite element and spectral and pseudo-spectral methods. We are using finite volume technique for its simplicity and accuracy [77]. Before proceeding to finite volume method, it is appropriate to define certain properties of numerical solutions which determine the level of accuracy and details which can be achieved in finite difference based methods. These properties include [76]:

- Stability
- Consistency, and
- Convergence

Stability of a numerical solution describes whether or not the dependent variable is bounded. For transient analysis, the dependent variable is unstable if the solution oscillates with an amplitude that increases with time.

Consistency implies that the solution of the partial differential equation, if it is smooth, is an approximate solution of the finite difference scheme.

The third property of a numerical method is the degree of convergence of the solution. A numerical solution is said to be convergent if the discretization error approaches zero as the mesh is refined. In other words, the exact solution is approached numerically through mesh refinement by either increasing the number of spatial increments or the time increments. For finite difference or finite volume solutions, the

Lax theorem [76] states that the convergence is ensured if and only if the solution is both stable and consistent.

4.3 Finite Volume Approach

The particular practice that we have chosen here for the derivation of discretized equation is the Finite Volume [77] approach. The calculation domain is divided into subdomains or control volumes such that there is one control volume around a grid point. The differential equation is integrated over the control volume to yield the discretization equation. Thus, the discretization equation represents the same conservation principle over a finite region as the differential equation does over an infinitesimal region. This direct interpretation of the discretization equation makes the method easy to understand in physical terms; the coefficients in the equation can be identified, even when they appear in a computer program, as familiar quantities such as flow rates, conductances, areas, volumes diffusivities etc.

The control-volume approach can be regarded as a special case of the method of weighted residuals [77], in which the weighing function is chosen to be unity over a control volume and zero everywhere else. The main reason for choosing the control-volume formulation is its simplicity and easy physical interpretation.

4.3.1 Discretization

Our model equations (3.1), (3.4), (3.6) and (3.7) are in axisymmetric coordinates. The finite difference counterparts of these equations are derived by considering a grid point cluster in calculation domain. A portion of such a two-dimensional grid for

axisymmetric system is shown in Figure 4.1. For the grid point P, points E and W are its r-direction neighbors, while N and S are the z-direction neighbors. The control volume around P is shown. Its thickness in θ-direction is $2\pi r$ because of axis of symmetry. While thickness in r-direction is Δr and in z-direction it is Δz, distances between nodal points are being defined as δ_e, δ_w, δ_n and δ_s for distance between PE, PW, PN and PS respectively. Now we integrate equation (3.1) over this control volume;

$$\int_t^{t+\Delta t}\int_w^e\int_s^n \rho c_p \frac{\partial T}{\partial t} r\,dr\,dz\,dt = \int_t^{t+\Delta t}\int_w^e\int_s^n \left[\frac{1}{r}\frac{\partial}{\partial r}\left(k\frac{\partial T}{\partial r}\right) + \frac{\partial}{\partial z}\left(k\frac{\partial T}{\partial z}\right) + S_o\right] r\,dr\,dz\,dt \qquad (4.1)$$

For this integration we make the following assumptions:

- Temperature has same value over the whole control volume as nodal value.
- Time integration on right side is of explicit type, i.e. after time integration temperature at any node takes the value calculated at the previous time step.
- Source term, like temperature, has constant value over whole control volume as nodal value at any given instant.
- k and c_p are either function of temperature or constant, where ρ is constant.

After performing complete integration on left side and space integration on right

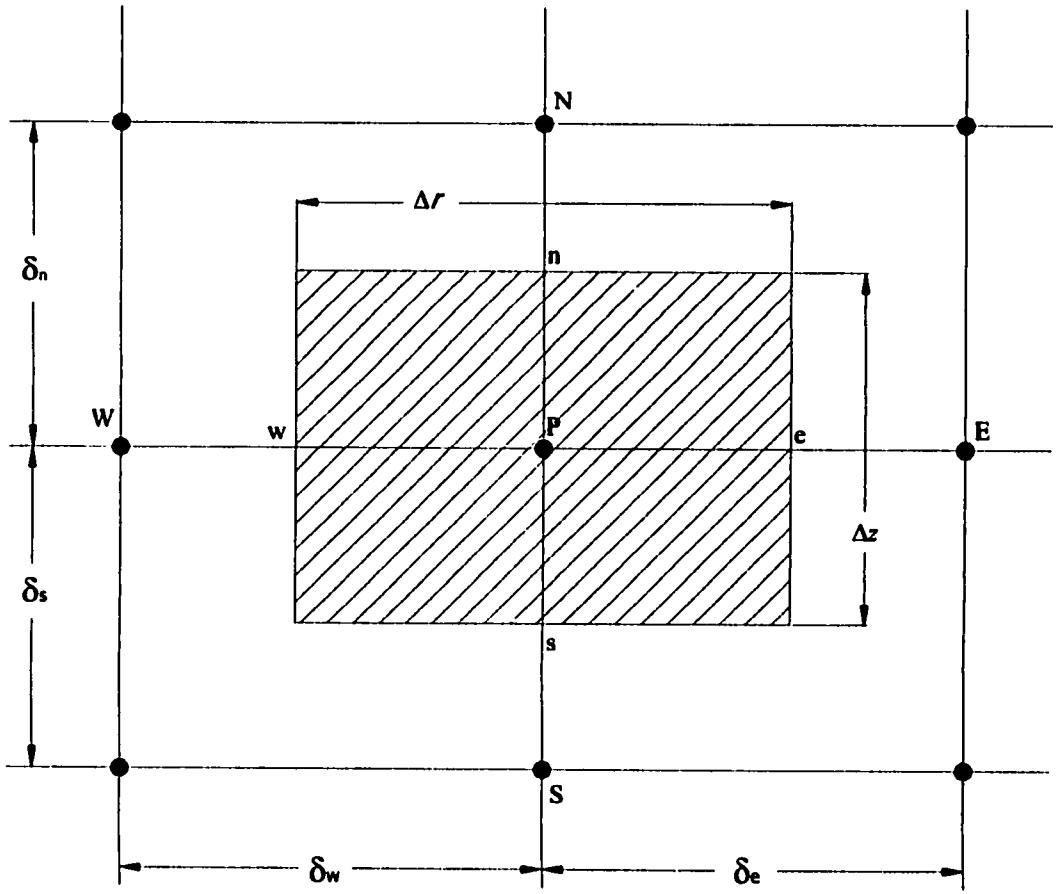

Figure 4.1: Control Volume

side we get.

$$(T_P - T_P^o)\,\rho c_p r_P \Delta r \Delta z = \int_t^{t+\Delta t} \left[\frac{k}{r_P} \left[\left(\frac{\partial T}{\partial r} \right)_e - \left(\frac{\partial T}{\partial r} \right)_w \right] \Delta z + k \left[\left(\frac{\partial T}{\partial z} \right)_n - \left(\frac{\partial T}{\partial z} \right)_s \right] \Delta r + S_o \Delta r \Delta z \right] dt \quad (4.2)$$

Now assuming linear temperature variation between nodal values we can replace the derivatives at wall with central difference equivalents and for time integration explicit scheme suggest that all temperature should be considered at existing or initial values. Thus we get

$$(T_P - T_P^o)\,\rho c_p \Delta r \Delta z = \left[\frac{k}{r_P} \left[\left(\frac{T_E^o - T_P^o}{\delta_e} \right) - \left(\frac{T_P^o - T_W^o}{\delta_w} \right) \right] \Delta z + S_o \Delta r \Delta z + k \left[\left(\frac{T_N^o - T_P^o}{\delta_n} \right) - \left(\frac{T_P^o - T_S^o}{\delta_s} \right) \right] \Delta r \right] \Delta t \quad (4.3)$$

Simplifying and arranging the above equation results in:

$$a_P T_P = a_E T_E^o + a_W T_W^o + a_N T_N^o + a_S T_S^o + a_P^o T_P^o + S_o \Delta r \Delta z \quad (4.4)$$

Where

$$
\begin{aligned}
a_P &= \frac{\rho c_p \Delta r \Delta z}{\Delta t} \\
a_E &= \frac{k \Delta z}{r_P \delta_e} \\
a_W &= \frac{k \Delta z}{r_P \delta_w} \\
a_N &= \frac{k \Delta r}{\delta_n} \\
a_S &= \frac{k \Delta r}{\delta_s} \\
a_P^o &= a_P - a_E - a_W - a_N - a_S
\end{aligned}
$$

This is the required discretized form of conduction equation.

In a similar manner we can discretize equations (3.6) and (3.7) which are taking care of heat transfer and phase change in mushy zone. These equations result as:

$$b_P x_{m_P} = a_E T_E^o + a_W T_W^o + a_N T_N^o + a_S T_S^o + a_P^o T_P^o + b_P x_{m_P}^o + S_o \Delta r \Delta z \qquad (4.5)$$

where

$$
\begin{aligned}
b_P &= \frac{\rho_m L_m \Delta r \Delta z}{\Delta t} \\
a_E &= \frac{k \Delta z}{r_P \delta_e} \\
a_W &= \frac{k \Delta z}{r_P \delta_w} \\
a_N &= \frac{k \Delta r}{\delta_n} \\
a_S &= \frac{k \Delta r}{\delta_s} \\
a_P^o &= -a_E - a_W - a_N - a_S
\end{aligned}
$$

4.3.2 Boundary Conditions

To discretize our domain we use a technique [77] in which we devide the whole domain in finite volume cells and put the nodes at the center of the cells in this scheme no node appear on boundary. For boundary we assume that there are also cells with zero thickness normal to the boundary as shown in Figure 4.2 where $\Delta r = 0$ at vertical wall on left boundary and $\Delta z = 0$ at horizontal wall on top boundary, thus we get nodes at the boundaries.

We have four boundaries and four boundary conditions we will use these boundary conditions with equations (4.2) and (4.3) to get discretized equations at boundaries.

At surface we have $\Delta z = 0$ and from boundary condition $\left(\frac{\partial T}{\partial z}\right)_n = 0$, with these conditions equation (4.3) gives:

$$
k \left(\frac{T_P^o - T_S^o}{\delta_s} \right) \Delta r = 0
$$

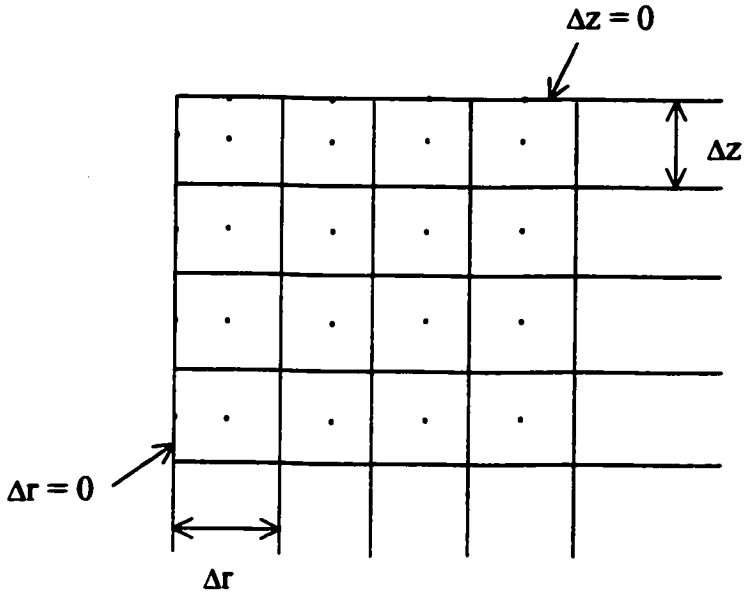

Figure 4.2: Computational grid and boundary cells.

or

$$T_P^o = T_S^o$$

at surface.

At axis of symmetry we have $\Delta r = 0$ and from boundary condition $\left(\frac{\partial T}{\partial r}\right)_w = 0$, with these conditions equation (4.3) gives:

$$k\left(\frac{T_E^o - T_P^o}{\delta_e}\right)\Delta z = 0$$

or

$$T_P^o = T_E^o$$

at axis of symmetry.

At remaining boundaries we have specified temperatures.

4.3.3 Stability

Equation (4.4) is representing an explicit scheme for calculating the future temperature of a single node in terms of current temperatures of that node and its neighbors. It is thereby possible to calculate the temperatures for a given time increment node by node. In explicit scheme, the time steps have some uper limit, we can not select arbitrarily large time steps. Using VonNuemann stability criteria [76] we can find out the stability condition for our model equation with uniform grid in the following

form:

$$1 \geq \left(\frac{1}{r_P \Delta r^2} + \frac{1}{\Delta z^2}\right) \frac{2k\Delta t}{\rho c_p} \tag{4.6}$$

In case of nonuniform grid, the most stringent conditions correspond to smallest grid size. So we will use the smallest grids to calculate our time step and will use it through out.

4.4 Stress Analysis

Once we obtain the temperature field in solid substrate we can calculate the stress fields σ_r, σ_θ, σ_z using equations (3.25), (3.26) and (3.27). Equation (3.25) and (3.26) involve evaluation of integrals, for this purpose we are using same grid which we used for solution of conduction equation and are using trapezoidal rule for numerical integration. At any arbitrary point P (Figure 4.3) we calculate stresses as:

$$\begin{aligned} \sigma_r &= -\left(\frac{\alpha_T E}{1-\nu}\right) \frac{1}{2r_P^2} [(T_g + T_{g+1})\,\delta_{g+1} + (T_{g+1} + T_{g+2})\,\delta_{g+2} + ... \\ &\quad + (T_{P-1} + T_P)\,\delta_P] \end{aligned} \tag{4.7}$$

and,

$$\begin{aligned} \sigma_\theta &= -\left(\frac{\alpha_T E}{1-\nu}\right) \frac{1}{2r_P^2} [[(T_g + T_{g+1})\,\delta_{g+1} + (T_{g+1} + T_{g+2})\,\delta_{g+2} + ... \\ &\quad + (T_{P-1} + T_P)\,\delta_P] - 2T_P r_P^2] \end{aligned} \tag{4.8}$$

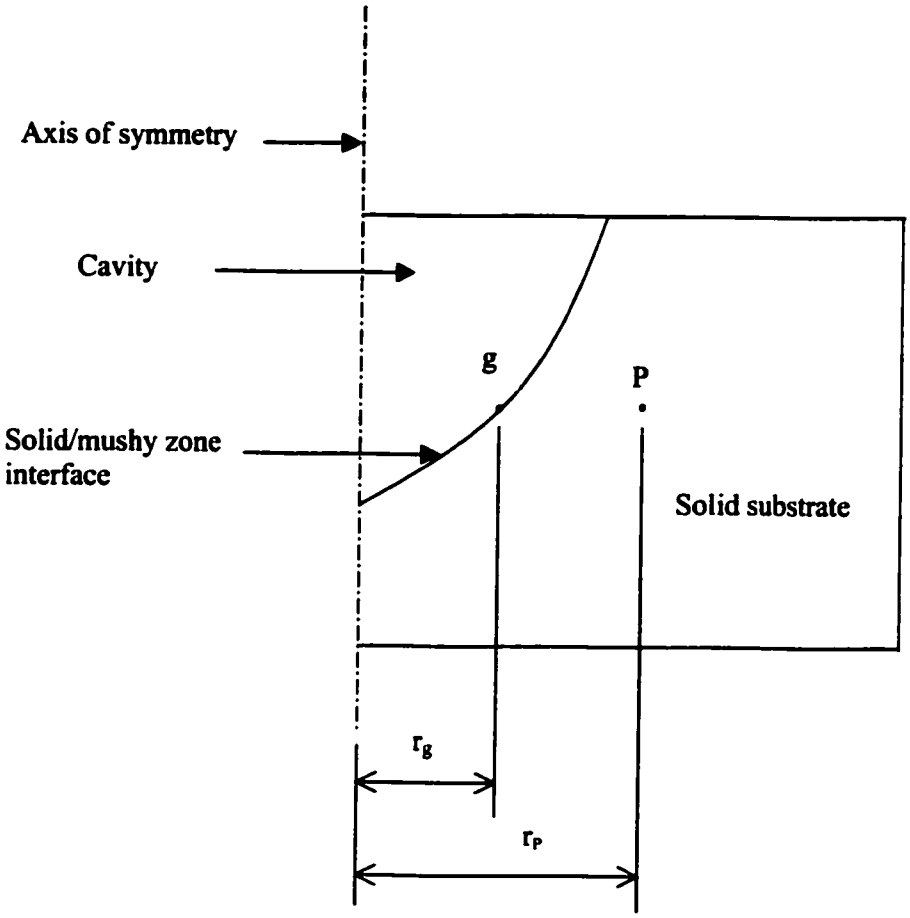

Figure 4.3: Nomenclature for stress calculation.

In case of conduction limited heating;

$$g = 0$$

4.5 Solution Algorithm

We are performing three different simulations here, one is for conduction limited heating of a stationary semi-infinite slab with fixed laser beam. In this simulation we are limiting the beam intensity so that peak temperature remain below melting point of substrate material. In other two simulations non-conduction limited heating is investigated, where we are providing enough energy to melt and subsequently evaporate the base material. In this case a cavity is formed and a layer of liquid phase exist in the cavity. In this simulations most important task is to track the moving boundaries. To perform all these simulations we developed two different algorithms and have written two programs.

4.5.1 Conduction Limited Heating Algorithm

To simulate the conduction limited heating, the following steps were followed and a program was developed whose flow chart is shown in Figure 4.4. The program consist of main body and three subroutines.

- Define initial conditions.
- A spatially variable grid is generated with 80×100 nodes.
- All the coefficients for discretized conduction equation (4.4) are calculated.

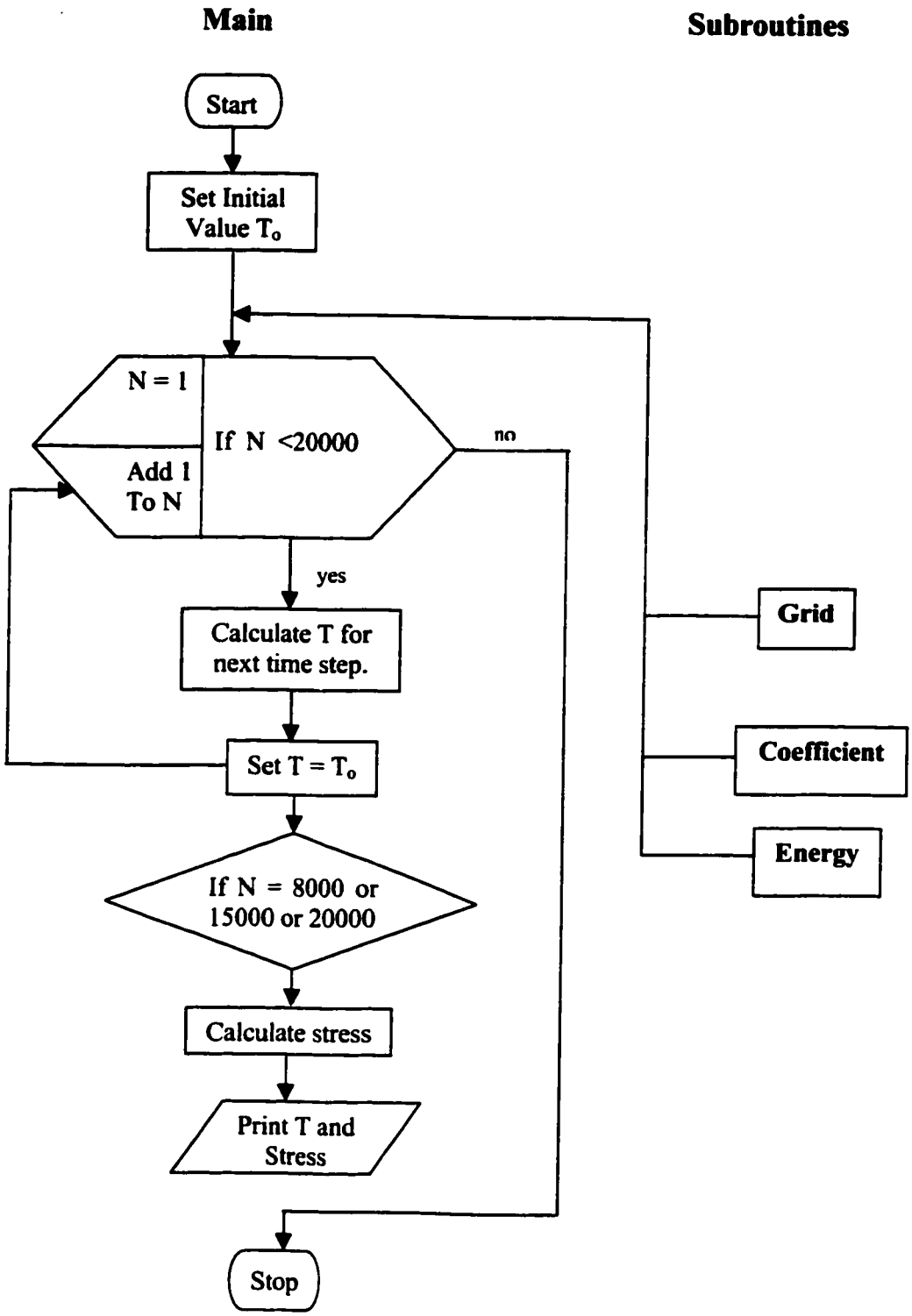

Figure 4.4: Flowchart for conduction limited heating algorithm.

- Source term at each node is calculated.
- Using stability criteria given in equation (4.6) with smallest grid size time step is established as 4×10^{-13}.
- Using this time step we need 20000 time steps to model heating period of 8ns.
- Using discretized equation (4.4) and initial conditions temperature is calculated at each node for next time step.
- In this manner we can keep on advancing and can calculate temprature history.
- To calculate stress field at any given instant we use equation (4.7) (4.8) and (3.31) and temperature field at that instant.
- For the analysis we save temperature and stress fields at certain heating periods.

A schematic view of laser beam and mesh points used in simulation is shown in Figure 4.5.

4.5.2 Non-Conduction Limited Heating Algorithm

To simulate the non-conduction limited heating following steps are followed and a program is developed whose flow chart is shown in Figure 4.6. The program consist on main body and six subroutines. Here we are employing a switch-on switch-off technique to track the moving boundary for the case when material reached to evaporating temperature. Conduction equation is only applicable to solid and liquid heating and therefore the region reaching the evaporation temperaure is out of computation do-

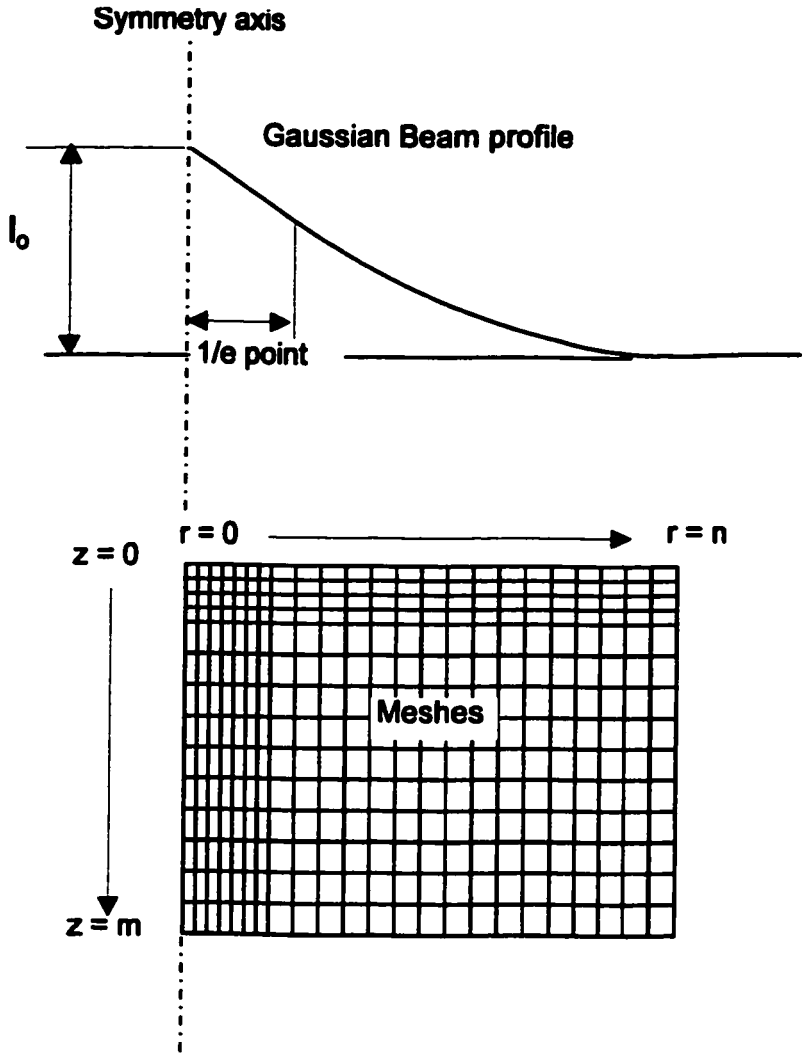

Figure 4.5: Schematic view of laser beam profile and mesh points (n=80,m=100 for conduction limited heating, n = 480 and m = 500 for non-conduction limited heating).

main. We switched those cells off and enforce a boundary condition for liquid gas interface.

- Define initial conditions.
- A 500×450 grid is generated with a uniform region of 400×300 near the beam center and remaining away from the beam spot.
- All the coefficient for discretized equations (4.4) and (4.5) are calculated.
- Source term at each node is calculated.
- Using stability criteria given in equation (4.6) with smallest grid size time step is established as 4×10^{-13}.
- Using this time step we need 20000 iterations in time to model heating period of 8ns.
- Using discretized equation (4.4) and initial conditions temperature is calculated at each node for next time step.
- When the melting temperature is reached then we invoke equation (4.5) for the mushy region. Once required conditions for a cell to melt down completely are met, we move back to equation (4.4) for the cell.
- When temperature of a cell reaches the evaporating temperature we envoke equation (4.5) for evaporation and when cell is evaporated completely i.e. $x_b \geq 1$ we switched this cell off i.e. we remove it from the calculation domain and shift the boundary and boundary condition to next adjacent cells. Now this cell is not

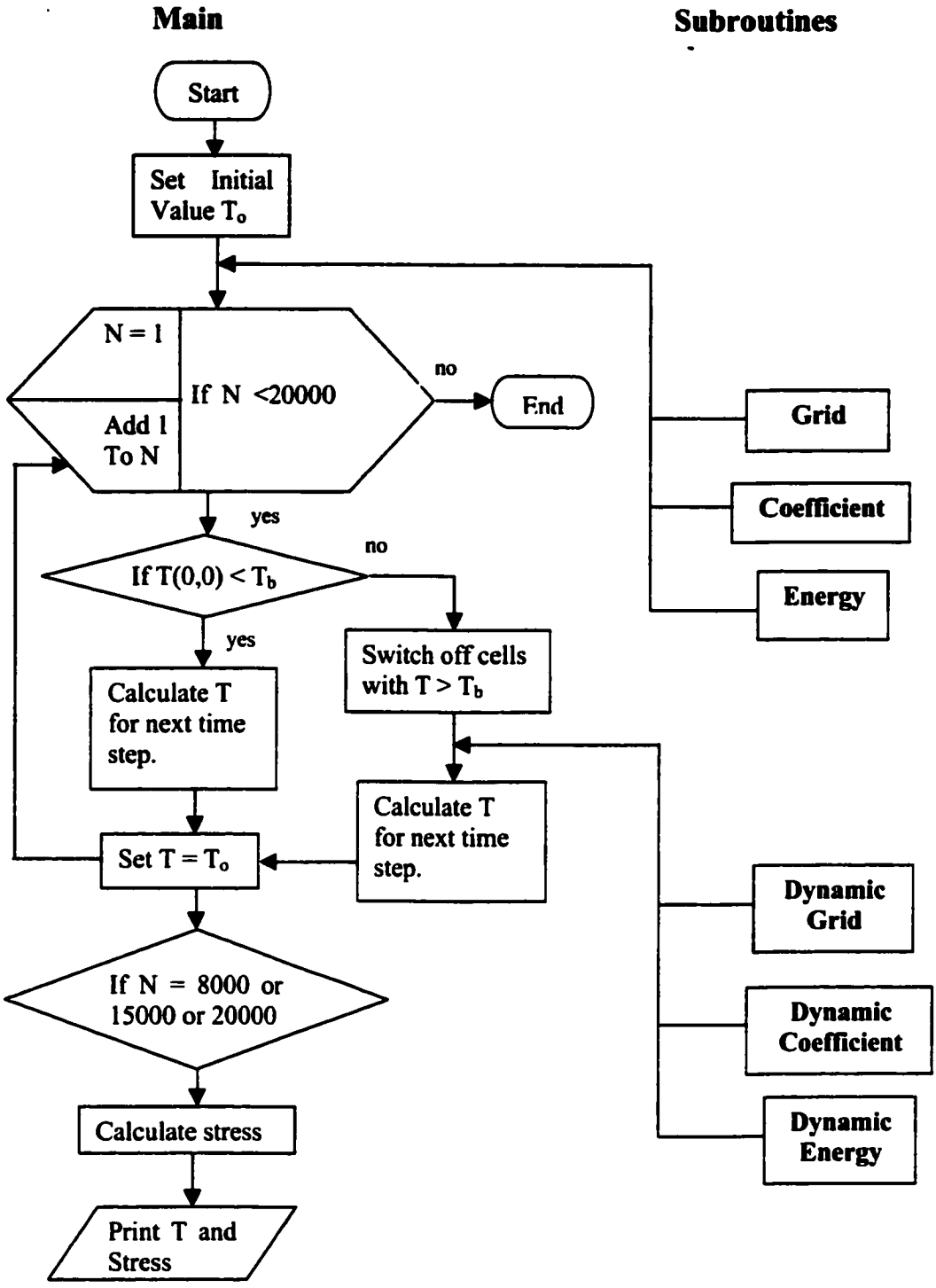

Figure 4.6: Flowchart for non-conduction limited heating algorithm.

interacting with reminder of the substrate material and it is also not absorbing energy from the beam anymore.

- Now we have to calculate the new energy term for remaining cells in calculation domain.

- We calculate the new grid, source term and coefficients using subroutines dynamic grid, dynamic coefficient and dynamic energy.

- To calculate the stress field at any instant we use equation (4.7) (4.8) and (3.31) and temparature field at that instant.

Chapter 5

RESULTS and DISCUSSIONS

Laser heating of substrate material with stationary pulse is considered in current study. Both conduction limited and non-conduction limited processes are modeled. As the pulse duration is 8ns which is much higher than electron relaxation time therefore equilibrium heating models are applicable and Fourier theory is used to predict the temperature in substrate material.

5.1 Conduction Limited Heating

Laser pulse heating of steel substrate is considered and thermal stresses during the heating pulse are computed. Since laser output power intensity distribution is as Gaussian, the axisymmetric heating and thermal stresses are considered in the analysis. As the process is conduction limited therefore no phase change is involved. The thermal properties of substrate material and pulse properties are given in Table 5.1.

5.1.1 Temperature Field for Conduction Limited Heating

Figure 5.1 shows the dimensionless temperature contours at two heating period while Figure 5.2 shows the dimensionless temperature distribution inside the substrate

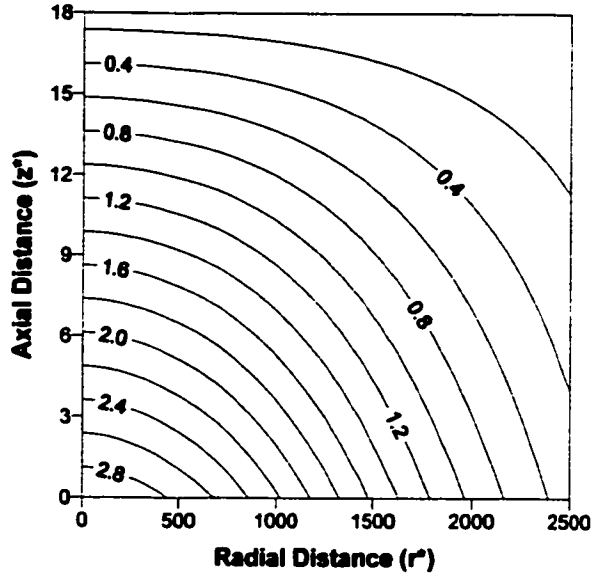

Time (t*) = 11

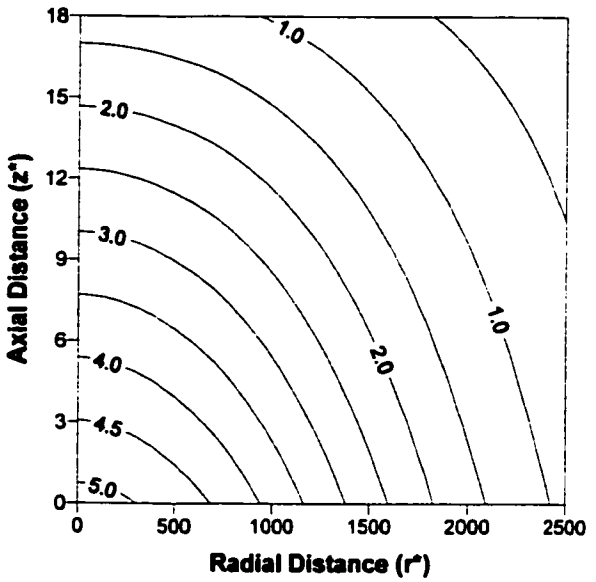

Time (t*) = 21

Figure 5.1: Temperature Contours.

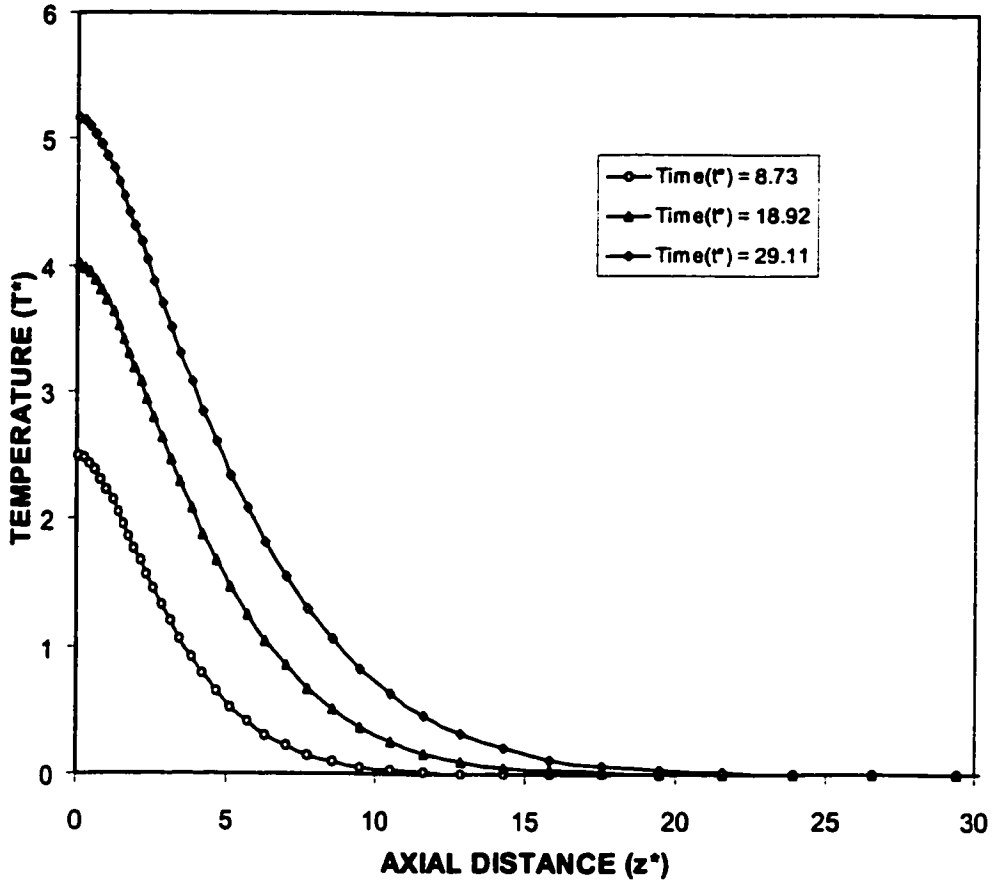

Figure 5.2: Variation of dimensionless temperature along dimensionless axial distance for different heating periods.

material for three heating periods. Temperature with increasing distance from the surface. This is more pronounced as the heating period progresses ($t^* = 29.11$). in this case, in the early heating period the energy gain by the substrate material results in the temperature rise in the surface vicinity. However, the temperature gradient is not substantial to accelerate the heat diffusion from surface region to bulk of the substrate material. Consequently, in the early heating period internal energy gain of the substrate dominates the heat diffusion from surface region to the bulk of the substrate material. As the heating progress the internal the internal gain of the substrate material becomes high in the surface vicinity, due to the absorption of irradiated energy field, and temperature gradient across the surface region becomes high. This is because of the absorption depth, i.e. the laser beam energy is absorbed within an absorption depth, which is about $1.6 \times 10^{-8}m$. Consequently, for the distances extend from the absorption depth towards the solid bulk, the internal energy gain is not considerable. Moreover, the high temperature gradient in the surface region accelerates the heat diffusion from the surface region to bulk of the substrate material. Consequently, as the heating period progresses the temperature gradient in the surface vicinity increases. This can also be seen from Figure 5.3 in which the temperature gradient along the axial distance is shown at three heating periods. The temperature gradient attains minimum value at some depth below the surface. At the point of minimum temperature gradient, the energy balance among the amount of absorbed energy, internal energy gain and energy diffused attain, i.e. the rate of internal energy increase attains almost steady as the heating progresses. The location of equilibrium moves away from the surface as the heating progresses. This indicates

that as the heating progresses the temperature gradient increases towards the solid bulk.

Figure 5.4 shows the temporal variation of temperature at the workpiece surface and at some depths below the surface while $r-$axis location is zero. Temperature rises rapidly in the early heating duration. As the heating progresses, the rate of rise of temperature reduces. This can also be seen from Figure 5.5, in which the time derivative of temperature with time is shown. The rapid rise of surface temperature in the early heating period is because of the rapid rise of the internal energy of the substrate in the surface region. In this case, the energy absorbed from the irradiated field is converted into internal energy gain of the substrate and the low temperature gradient suppresses the heat diffusion from the high temperature region to low temperature region (towards bulk of the substrate material). However, temperature profile behaves slightly different at distances below surface. In this case, the rate of temperature rise is low in the early heating period as the heating progresses; it almost attains steady rise. This is because of energy transport mechanism from the surface region to some depth below the surface i.e. the energy is transported through the diffusional process, which is slow in the pulse beginning due to low temperature gradient in this region.

Figure 5.6 shows the temperature distribution in the radial direction at different $z-$axis locations. The temperature gradient in the radial direction ($\partial T^*/\partial r^*$) attains low values in the region close to the symmetry axis. This is because of the laser power intensity distribution across the surface, which is Gaussian. In this case, in the region close to the symmetry axis (close to the irradiated spot center), laser energy

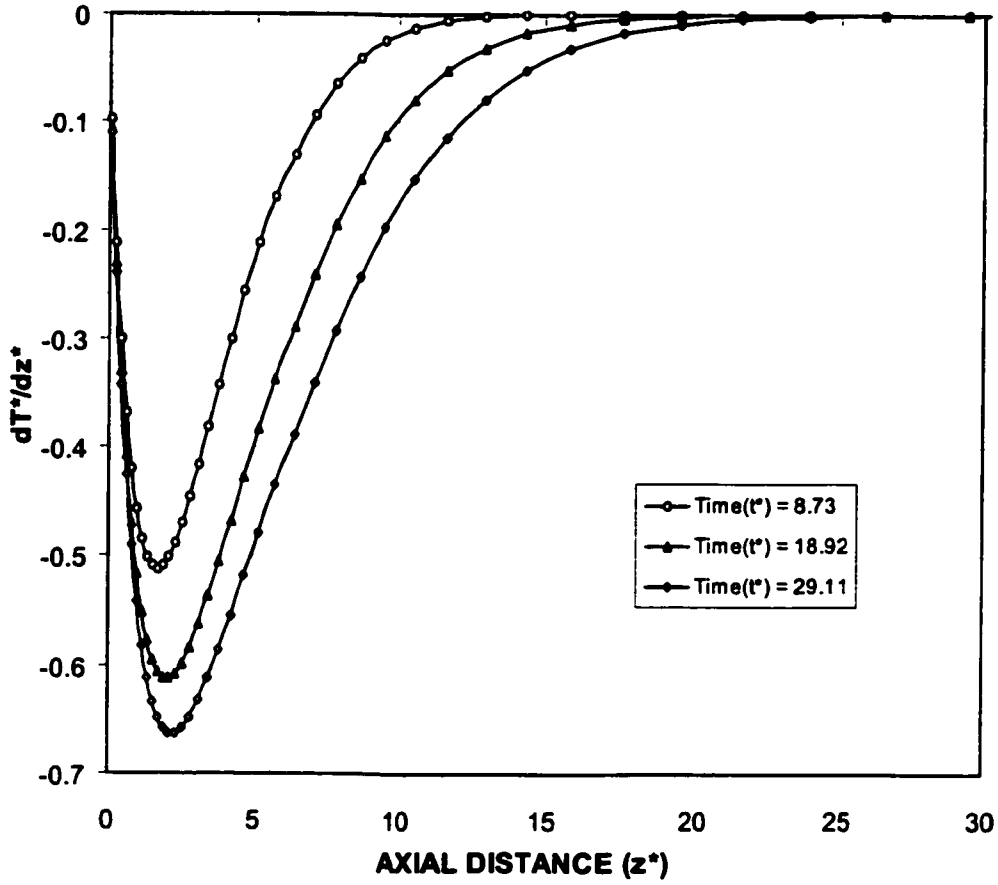

Figure 5.3: Variation of dimensionless temperature gradient along dimensionless axial distance for different heating periods.

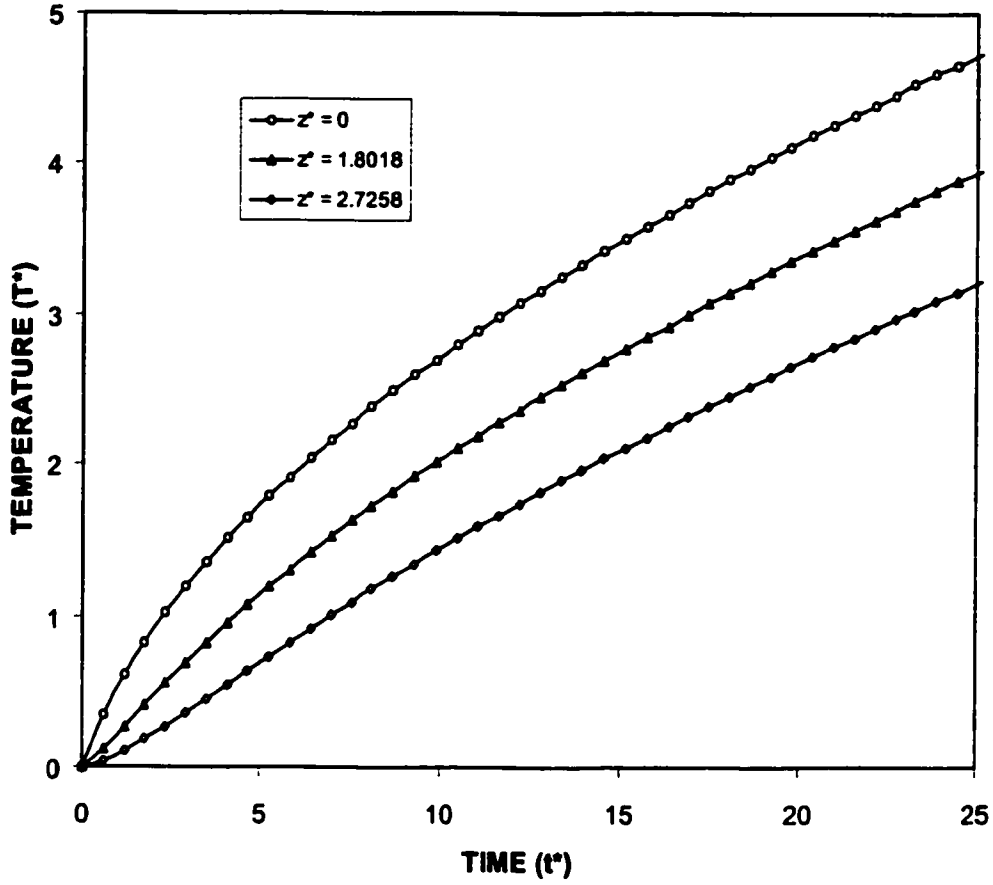

Figure 5.4: Temporal Variation of dimensionless temperature at different z-axis locations.

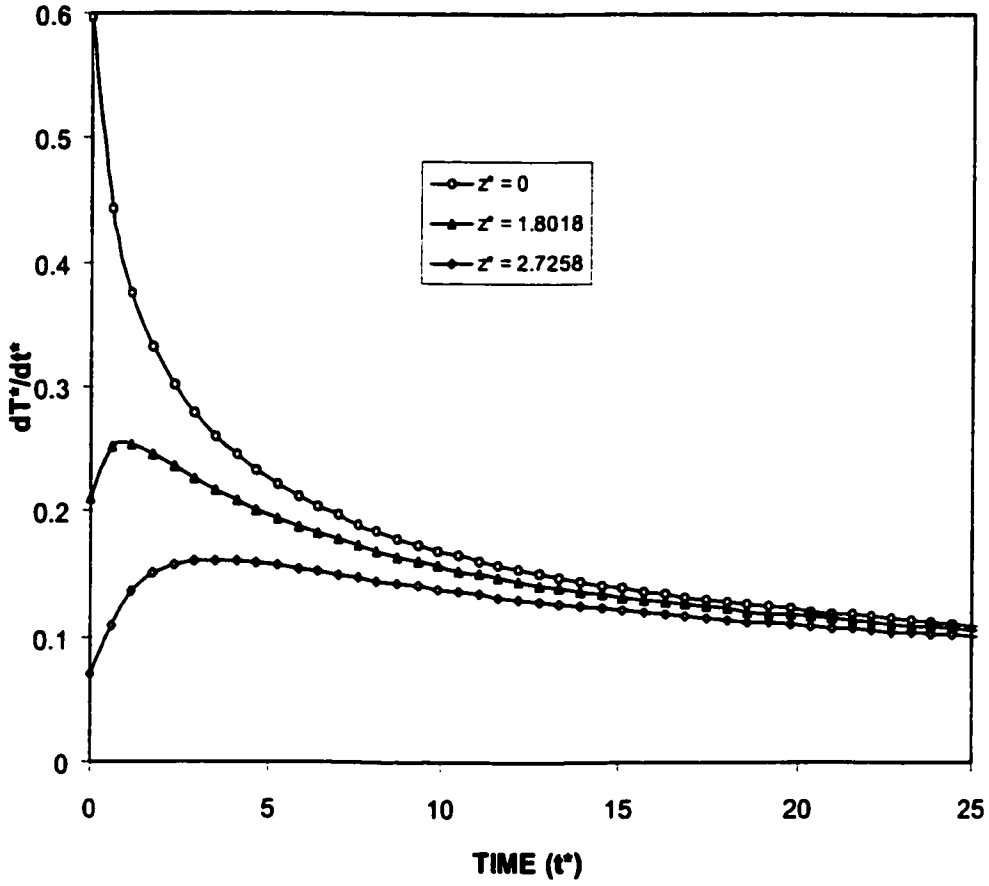

Figure 5.5: Temporal variation of dimensionless time derivative of dimensionless temperature at different z-axis locations.

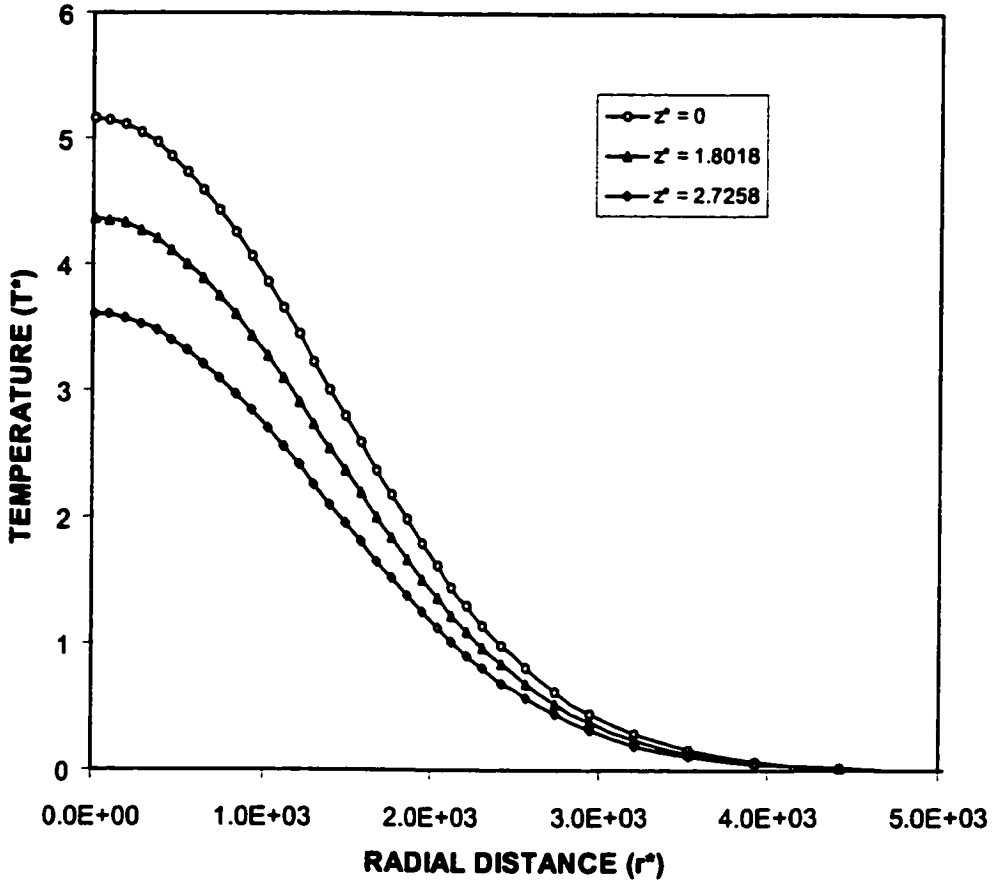

Figure 5.6: Variation of dimensionless temperature along dimensionless radial distance at different z-axis locations.

deposited into the substrate is high, i.e. the internal energy gain is high. However, the radial temperature gradient in this region is low, since the temperature distribution in this region does not decay sharply in this region. Consequently, heat diffusion in radial direction in this region is not significant. Moreover, as the distance extends further away from the symmetry axis, the temperature gradient becomes less due to less deposited energy in this region. Therefore, heat diffusion in this region becomes important as the internal energy gain through absorption of irradiated energy.This can also be seen from Figure 5.7 in which the temperature gradient $(\partial T^*/\partial r^*)$ is shown at different $z-$axis locations. The temperature gradient attains minimum at some distance from the symmetric axis. At the point of minimum temperature gradient internal energy gain and conduction losses are in balance such that the rate of internal energy becomes steady. Moreover, the location of point of minimum $(\partial T^*/\partial r^*)$ does not change with the depth below the surface. The temperature gradient attains less value as the depth from the surface increases.

5.1.2 Stress Field for Conduction Limited Heating

Figure 5.8 shows radial stress contours at two heating times while Figures 5.9 and 5.10 shows the radial stress distribution with axial direction and with time respectively. The radial stress component is compressive inside the substrate material and it increases as the heating period increases. This is because of the thermal strain developed rapidly during the heating period, i.e. material expands along the $z-$axis, since the free surface is located at $(z^* = 0)$ for all $r-$values. Consequently, material expansion generates compression in the radial direction. The stress component is

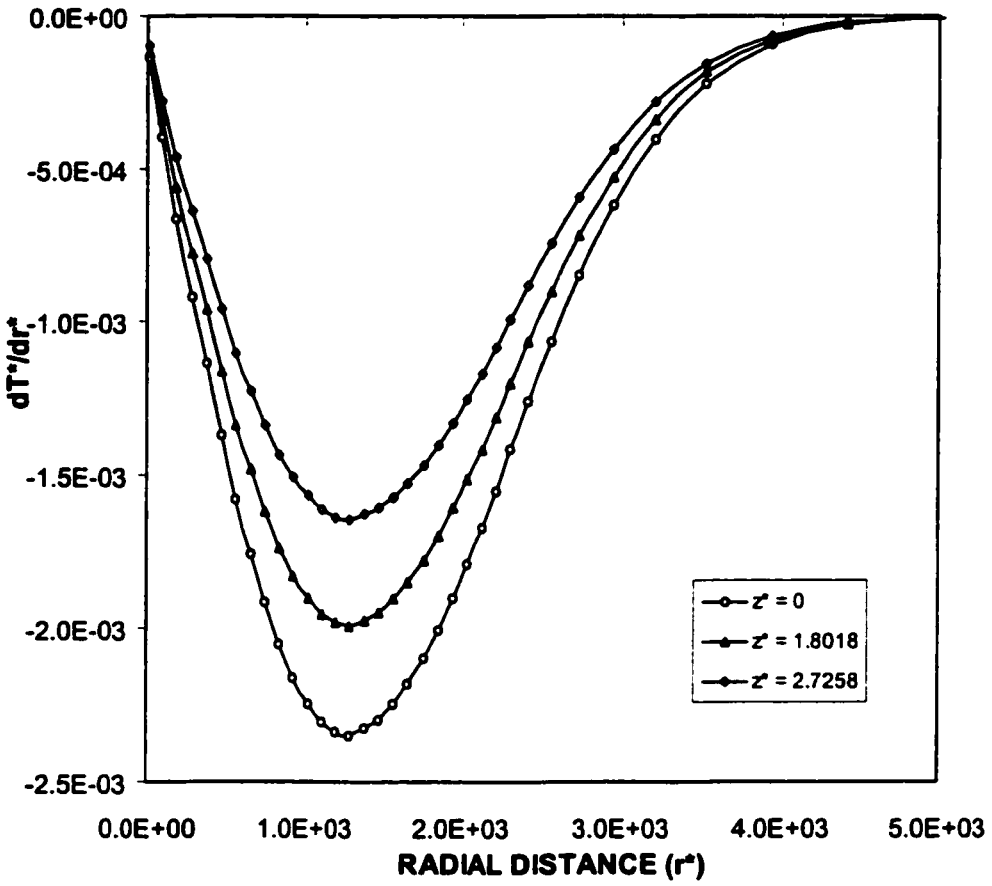

Figure 5.7: Variation of dimensionless temperature gradient along dimensionless radial distance for different z-axis locations.

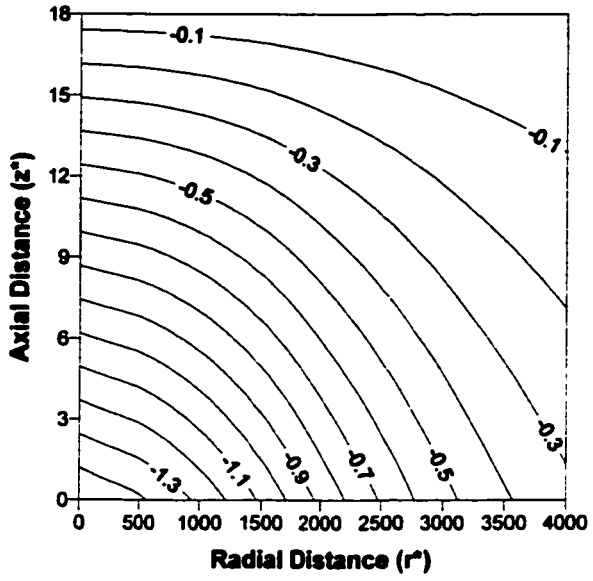

Time (t*) = 11

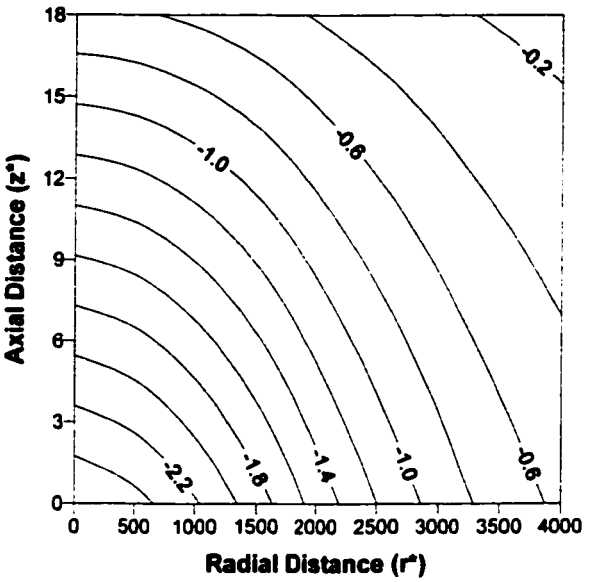

Time (t*) = 21

Figure 5.8: Radial stress contours.

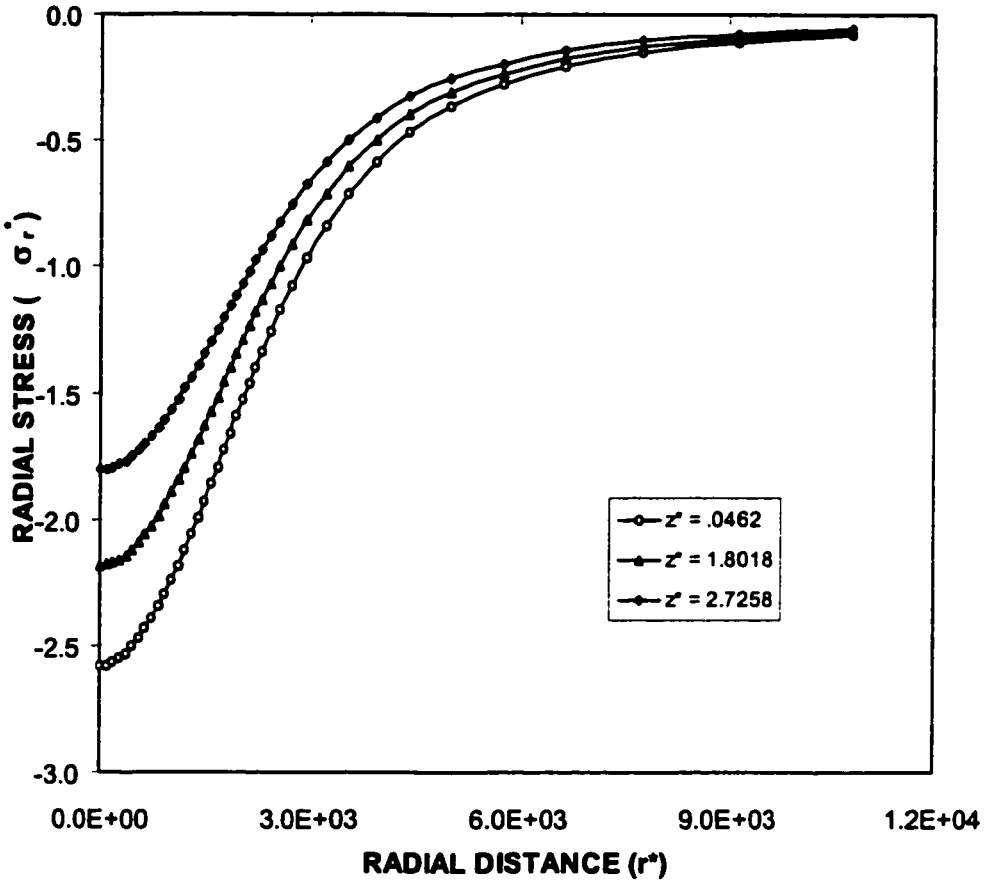

Figure 5.9: Variation of dimensionless radial stress component along dimensionless radial distance at different z-axis locations.

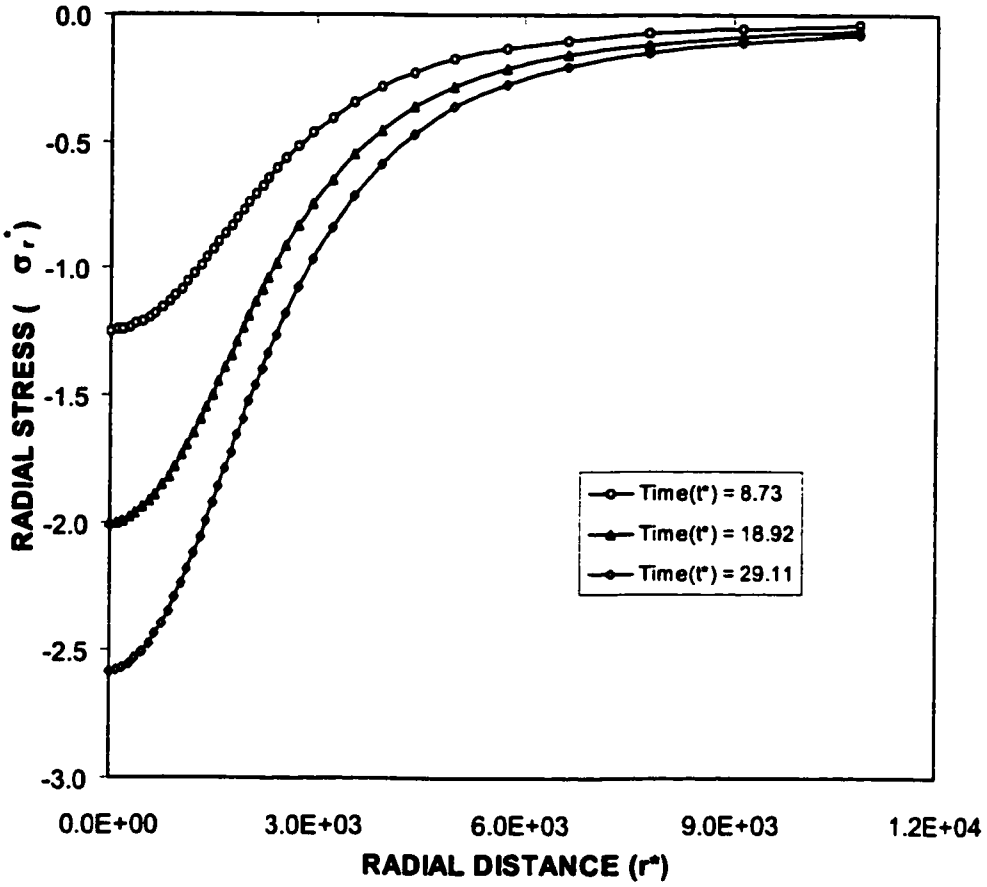

Figure 5.10: Variation of dimensionless radial stress component along dimensionless radial distance at different heating periods.

zero at the surface ($z^* = 0$), which employed as the boundary condition in the stress analysis. The gradient of the stress component attains low values in the surface vicinity. This is because of the temperature distribution in the radial direction, which has low gradient in the surface vicinity of the substrate material. This is true for all heating periods. In the case of Figure 5.10, the radial stress component increases with increasing heating period. The rate of increase in stress component is higher in the early heating period. In this case, the temperature rises rapidly in the early heating period due to absorption of irradiated energy, which in turn results in rapid change in temperature gradient. Therefore, the temporal variation in thermal strain becomes considerable in the early heating period. This is more pronounced in the region irradiated by a laser beam ($z^* \leq 1$).

Figure 5.11 shows the tangential stress contours at two heating periods while Figures 5.12 and 5.13 show the tangential stress component in the radial direction for different $z-$axis locations and at different heating periods, respectively. The stress component is compressive in the region close to irradiated spot center and as the radial location moves away from the irradiated spot center, it becomes tensile. The compressive behavior of the stress component close to the irradiated spot center is because of the temperature profile in the radial direction, i.e. the temperature attains the high values at the irradiated spot center and as the radial distance increases away from the irradiated spot center temperature reduces such that temperature gradient in radial direction ($\partial T^*/\partial r^*$) attains high values. This results in change of strain in this region. Consequently, positive stress values are resulted. As the distance increases further away from the irradiated spot center stress component reduces to

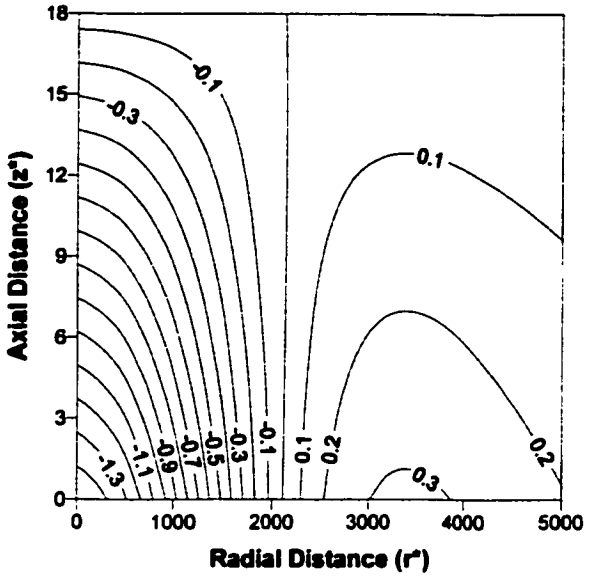

Figure 5.11: Tangential stress contours.

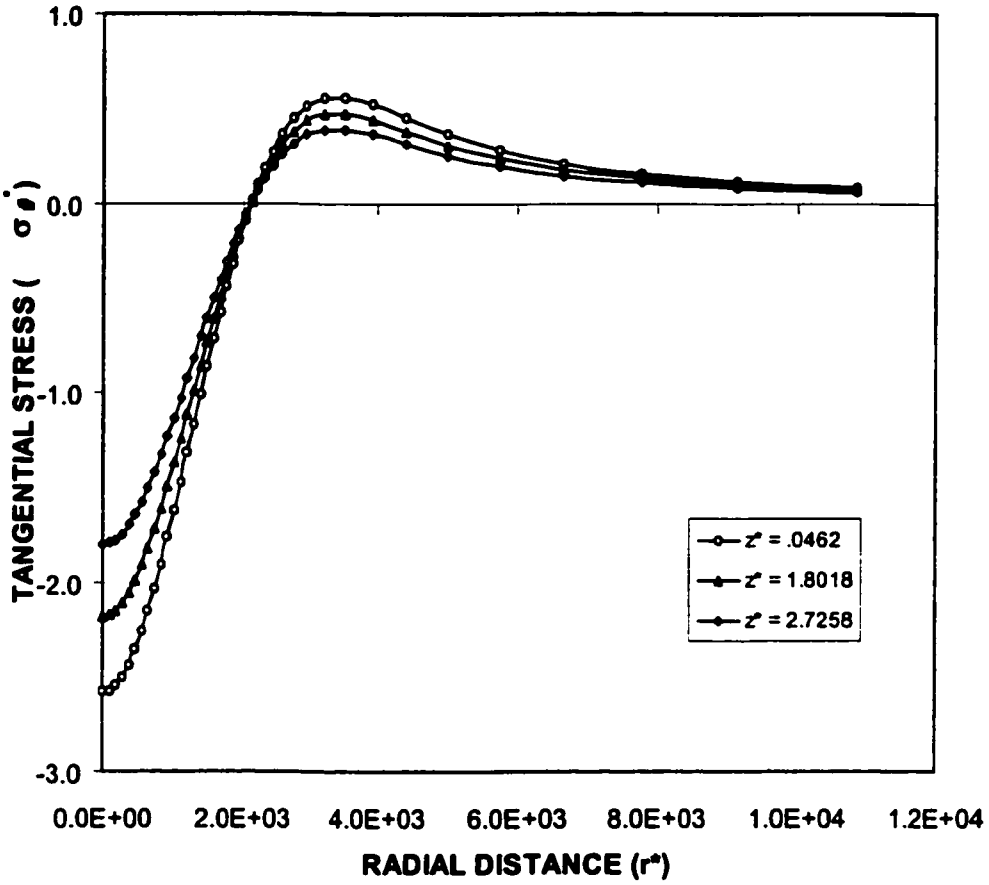

Figure 5.12: Variation of dimensionless tangential stress component along dimensionless radial distance at different z-axis locations.

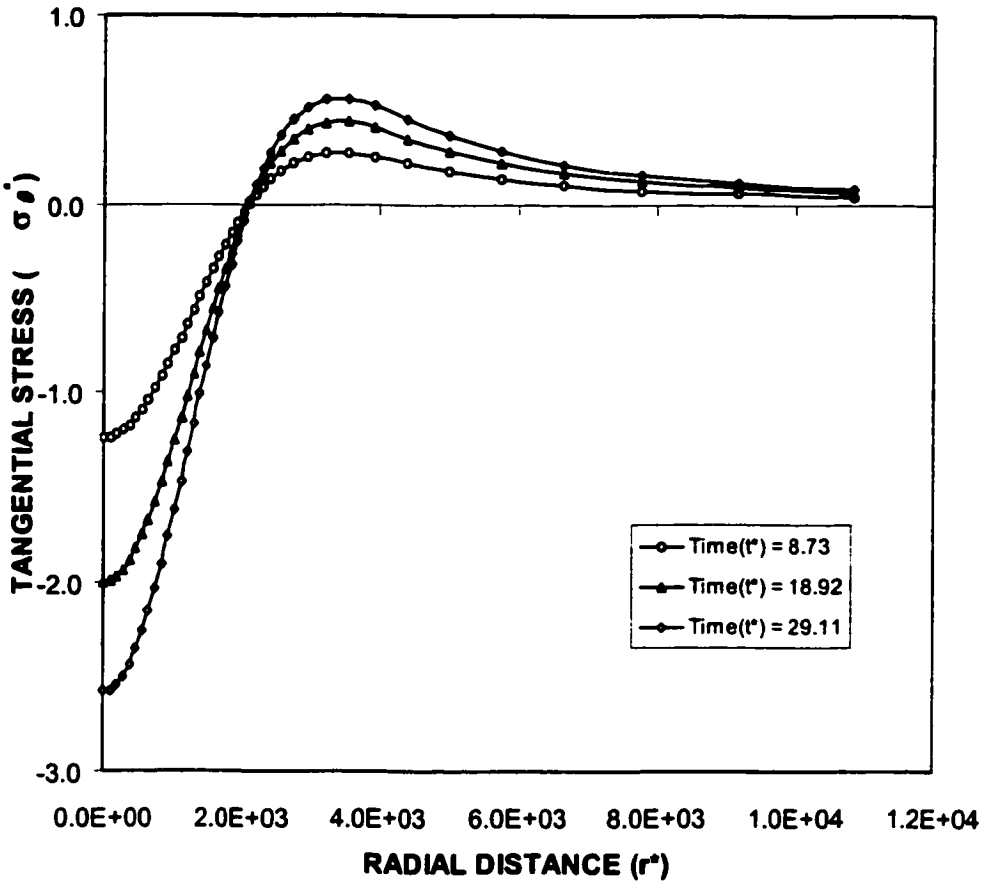

Figure 5.13: Variation of dimensionless tangential stress component along dimensionless radial distance at different heating periods.

zero, i.e. consistent with the boundary conditions employed in the stress analysis. In the case of Figure 5.13, the behavior of the stress component is similar to those shown in Figure 5.12, i.e. it is compressive in the region close to the irradiated spot center while it is tensile out of this region for all heating periods. The stress component attains high values as the heating period progresses. This is true for the compressive and tensile stress components. The stress gradient becomes higher as the heating period progresses. This is because of the development of temperature field with time, i.e. the rate of rise of temperature distribution in the radial direction increases as the heating progresses.

Figure 5.14 shows the equivalent stress contours at two heating periods while Figures 5.15 and 5.16 show equivalent stress distribution in the radial direction at different $z-$axis locations and for different heating periods, respectively. The equivalent stress shows wavy appearance with radial distance. This occurs because of the influence of radial distribution of stress components. In this case, all the stress components (radial, tangential and axial components) attain high values in the region close to the surface and the gradients of the stress components along the radial direction are not the same.

The stress gradient is low in the region close to the symmetry axis. This is because of the temperature distribution in the radial direction, i.e. the temperature gradient $(\partial T^*/\partial r^*)$ is also low in this region. Moreover, temperature gradient decays rapidly as the distance from the symmetry axis extends to $(250 \leq r^* \leq 1100)$, when the radial distance increases further $(1100 < r^* < 3000)$ the equivalent stress gradient becomes high. This because of the tangential stress component which becomes tensile

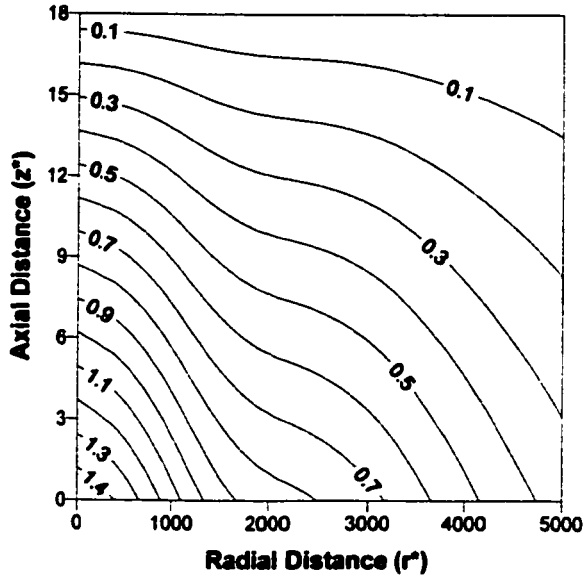

Time (t*) =11

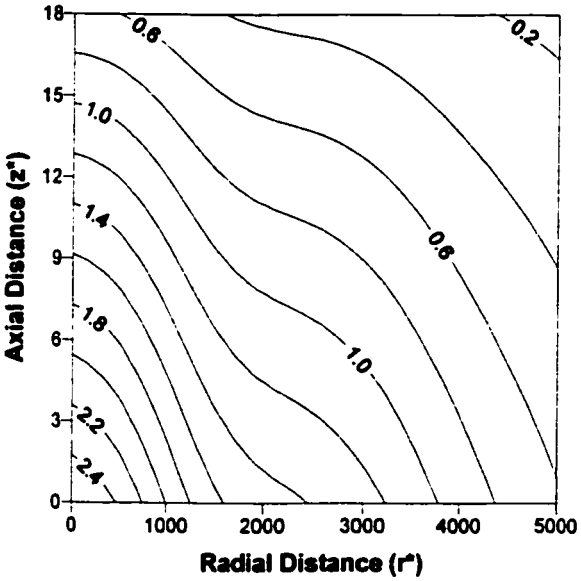

Time (t*) = 21

Figure 5.14: Equivalent stress contours.

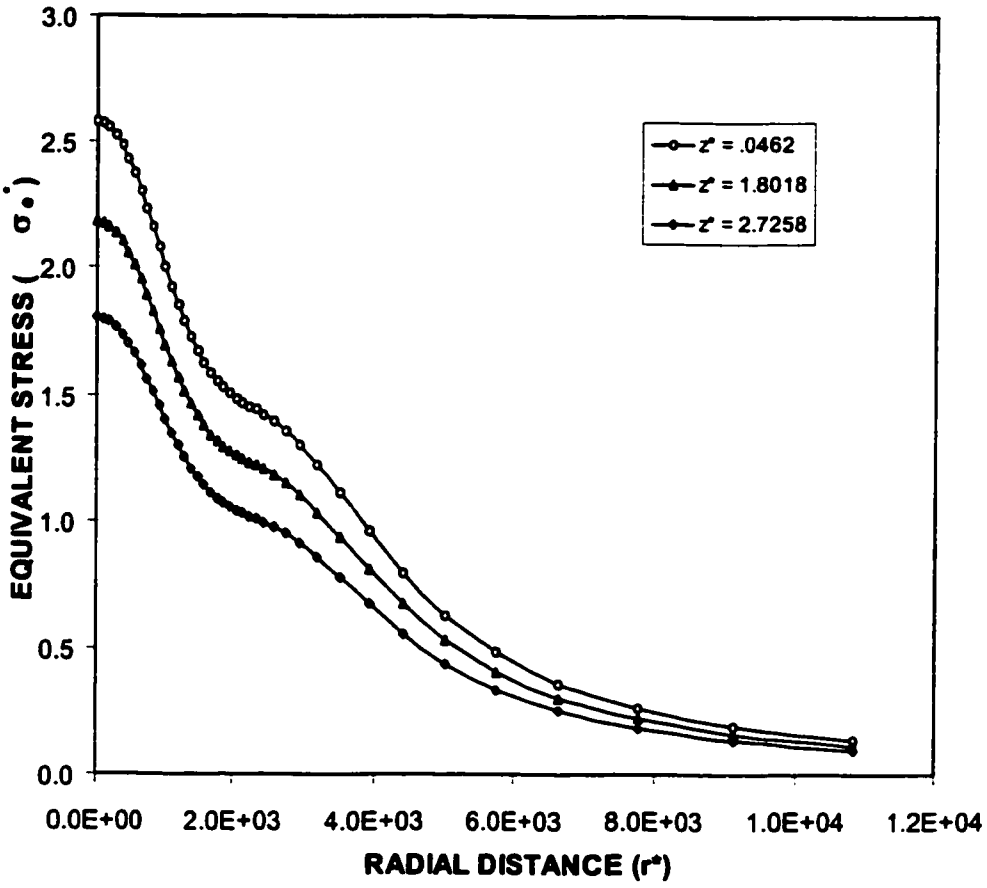

Figure 5.15: Variation of dimensionless equivalent stress along dimensionless radial distance at different z-axis locations.

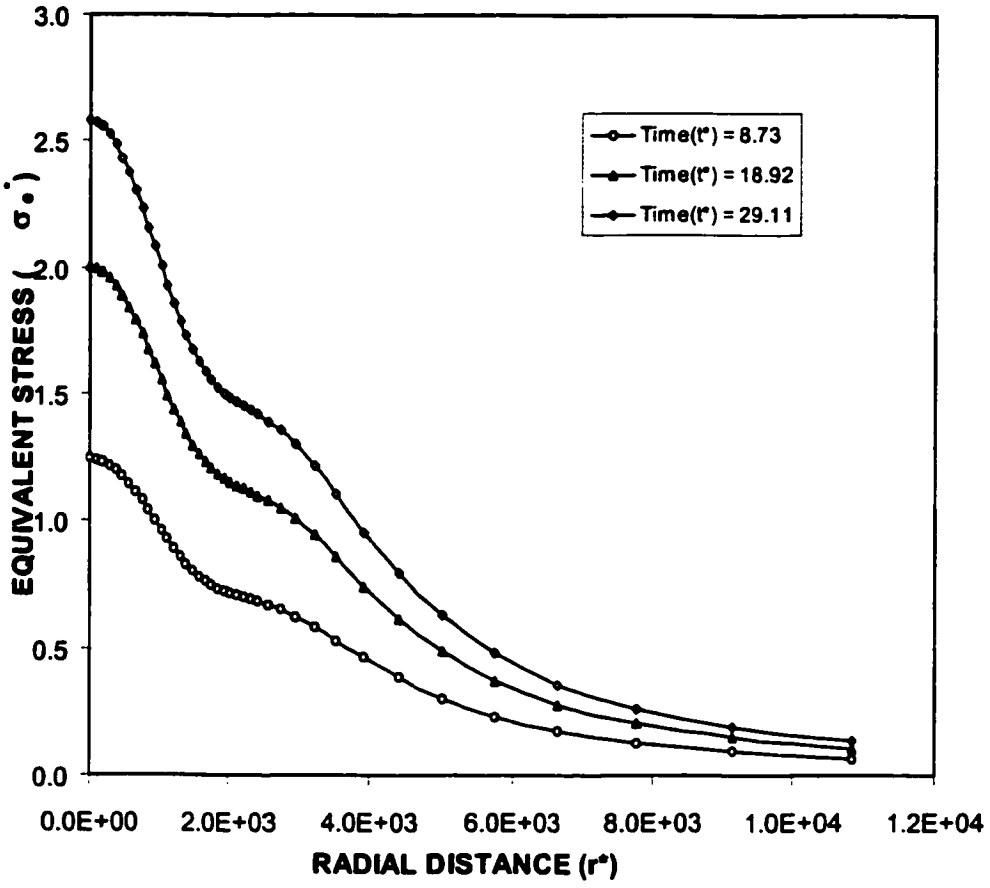

Figure 5.16: Variation of dimensionless equivalent stress along dimensionless radial distance at different heating periods.

in this region (Figure 5.12). The effect of the z-axis location on the equivalent stress is significant in the region ($3000 < r^* < 9000$). In this case, equivalent stress gradient decreases at a larger rate in the surface vicinity ($z^* = 0.462$) than those corresponding to other locations in the axial direction. In the case of Figure 5.16, the behavior of equivalent stress is similar to those shown in Figure 5.15. The decay rate of the equivalent stress increases as the heating period progresses. This occurs because of the radial temperature distribution inside the substrate material, i.e. increasing heating period results in high magnitude of temperature in the region close to the symmetry axis (Figure 5.6).

Figure 5.17 shows the equivalent stress distribution along the $z-$axis at different heating periods. Equivalent stress profiles almost the temperature profiles inside substrate material provided that the stress gradient differs than the temperature gradient. In this case, the equivalent stress decay rate is higher than the temperature decay rate.

5.2 Non-Conduction Limited Heating Step-Input Pulse Case

Laser pulse heating of steel is considered and numerical approach is introduced to simulate the temperature and thermal stress fields in the substrate material. In the analysis, melting and evaporation are included to account for the phase change processes. Control volume approach is introduced when discretizing the governing equation of energy transport. The variable properties are employed in the simulations, which are given in Table 5.2 while the pulse parameters are given Table 5.3.

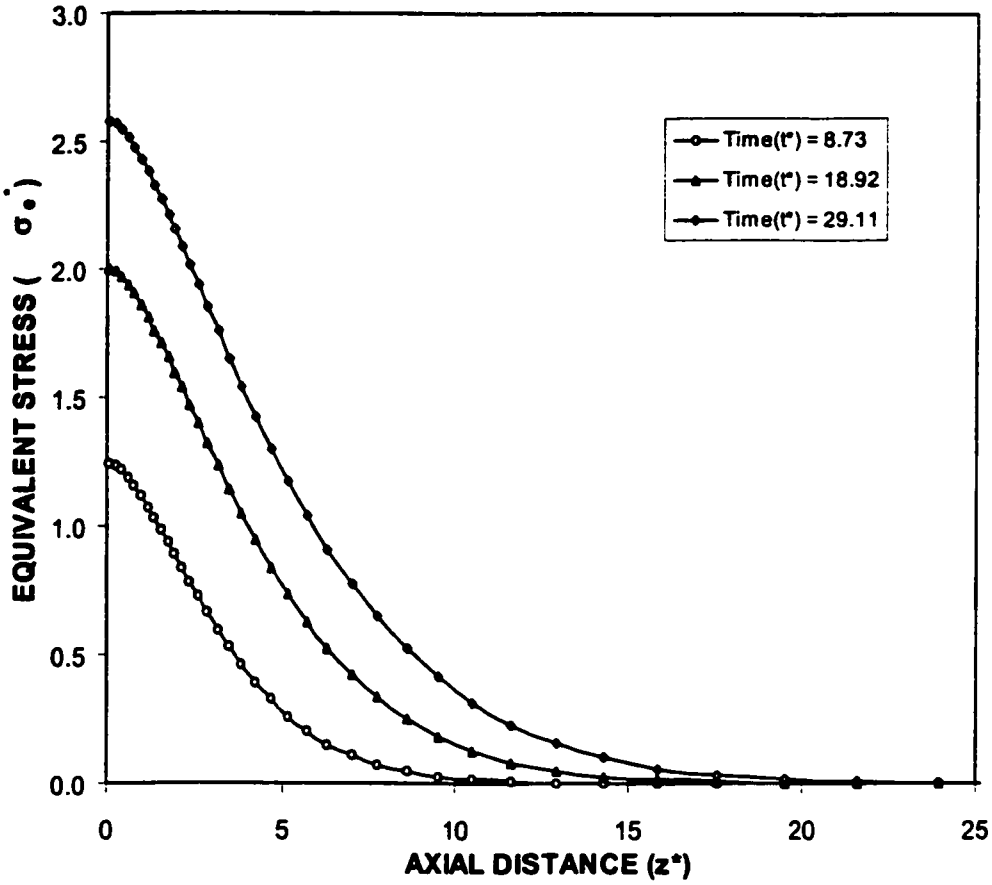

Figure 5.17: Variation of dimensionless equivalent stress along dimensionless axial distance at different heating periods.

5.2.1 Temperature Field for Non-Conduction Limited Heating

Figure 5.18 shows the counter plot of dimensionless temperature profiles inside the substrate material while Figure 5.19 shows dimensionless temperature distribution inside the substrate material along the $z-$axis at different heating periods. Temperature profiles terminate at some depth below the surface depending on the heating period, e.g. for $t^* = 0.846$, the corresponding depth is $z^* \cong 11$. This is because of the cavity formation after the evaporation process, i.e. substrate material was displaced during the evaporation process, which in turn generates a cavity, provided that the depth of cavity depends on the heating duration. Moreover, two regions in the temperature profiles are evident. In the first region, a solid heating occurs ($T^* < 0.07$), while liquid phase heating is dominant in the second region ($0.07 < T^* < 0.126$). This is observed through the temperature gradient $\left(\frac{\partial T^*}{\partial z^*}\right)$ curve, which is shown in Figure 5.20. In this case, the slope of temperature gradient curve changes across these regions. The slope of temperature gradient curves corresponding to different heating periods are similar in solid and liquid heating regions. This is because of the energy transport process; in which case, energy gained in the substrate material due to absorption of irradiated laser source ceases, i.e. the depth of cavity exceeds the absorption depth of the substrate material for the heating periods shown in Figure 5.19. Consequently, energy transport due to diffusion dominates the heat transfer process during the heating periods considered. The slope of the liquid heating changes sharply after the initiation of melting process, i.e. in the region of the melt the slope of temperature

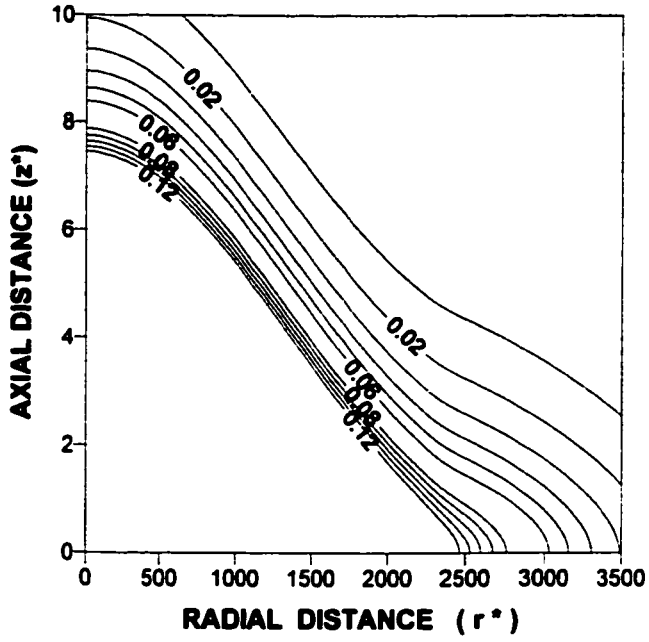

Time (t*) = 3.05

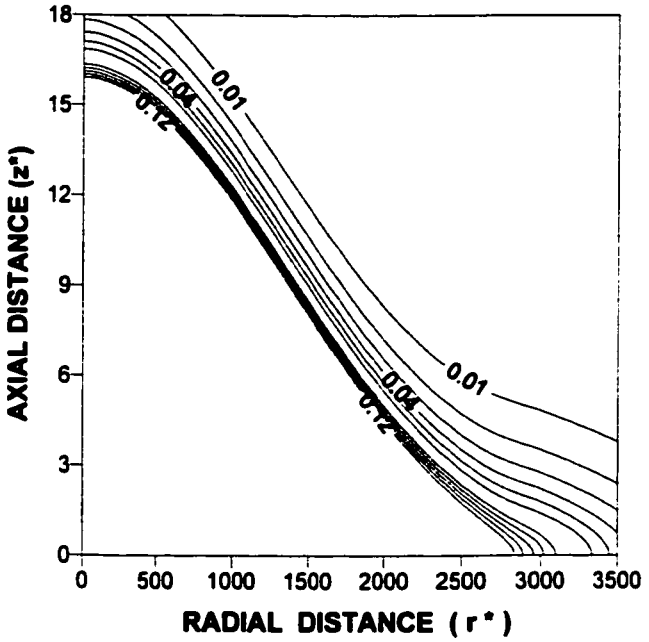

Time (t*) = 6.1

Figure 5.18: Temperature Contours for different heating periods.

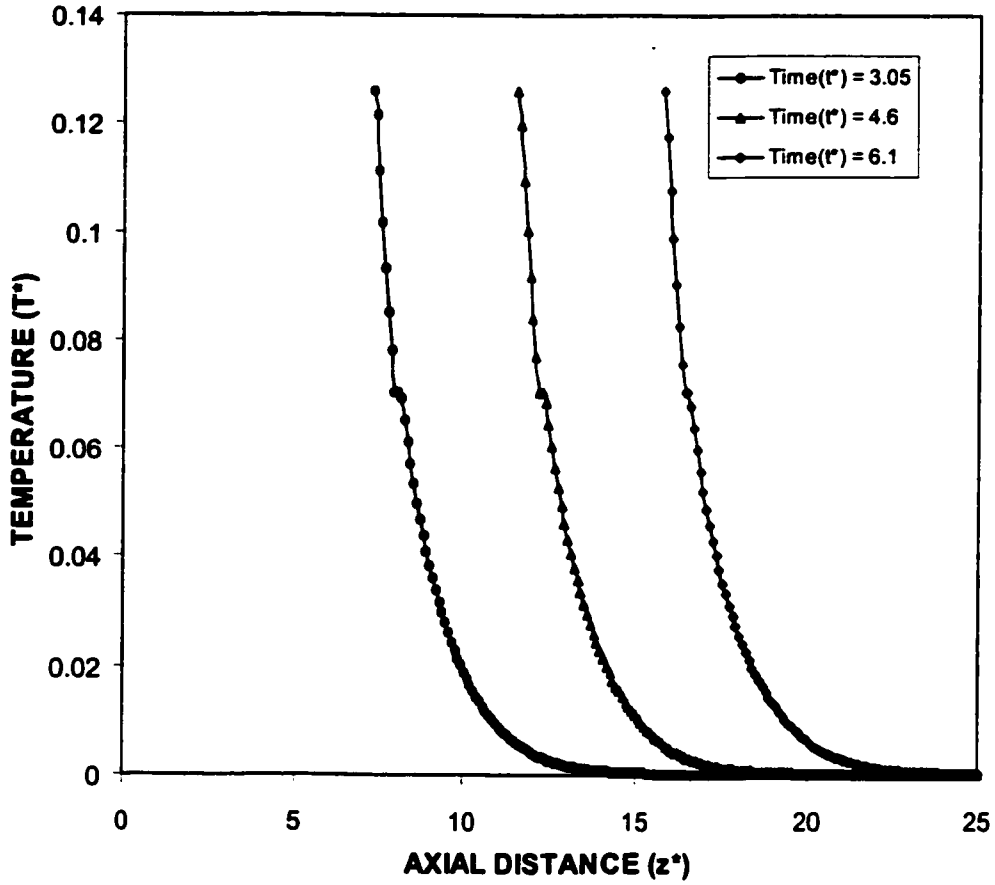

Figure 5.19: Variation of dimensionless temperature along dimensionless axial distance at different heating periods.

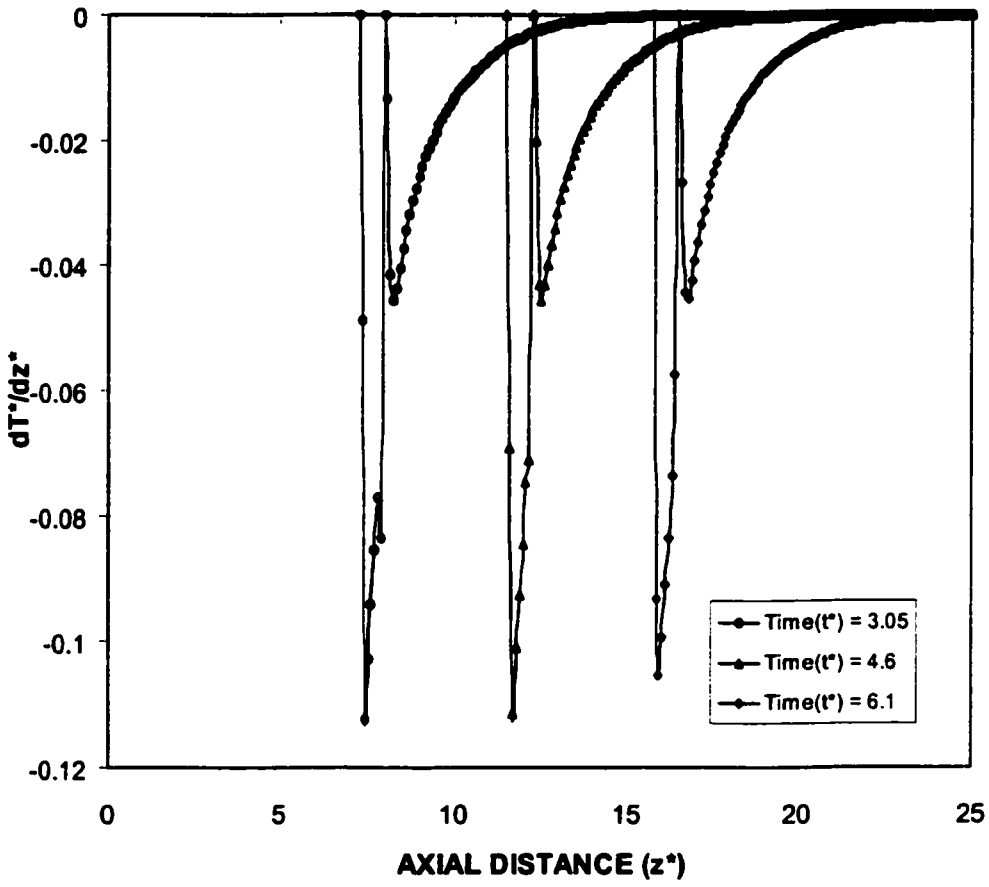

Figure 5.20: Variation of dimensionless temperature gradient along dimensionless axial distance for different heating periods.

curves changes sharply. This is because of the mushy zone introduced in the analysis, i.e. some of the substrate material is partially melted at constant temperature. Since the laser input intensity is high and the interaction duration is short, the size of the mushy zone is considerably small.

Figure 5.21 shows the dimensionless temperature profiles inside the substrate material along the radial axis at different heating periods. The behavior of the temperature profiles is similar to those shown in Figure 5.19, provided that the slope at the curves are different. The size of the cavity in the radial direction does not change considerably with time as compared to its counterpart corresponding to axial direction. This is because of the laser power intensity distribution across the heated spot, which is Gaussian, i.e. $\frac{1}{e}$ points of the power intensity distribution is $r^* = 1880$, which is comparable to the size of the cavity in the radial direction. In this case, evaporation ceases in the region corresponding to absorption of low intensity irradiation.

Figure 5.22 shows temporal variation of dimensionless surface temperature for constant and variable properties as well as dimensionless surface temperatures obtained from the enthalpy method. It should be noted that surface temperatures are computed from one-dimensional and constant properties case for enthalpy method for the simplicity. The dimensionless temperature profiles obtained from the one-dimensional enthalpy and energy methods are identical. Moreover, predictions of one-dimensional and three-dimensional cases are also almost identical. This is because of the short duration of heating and small area of irradiated spot, i.e. the radial conduction is negligibly small for the present case. The effect of variable properties on

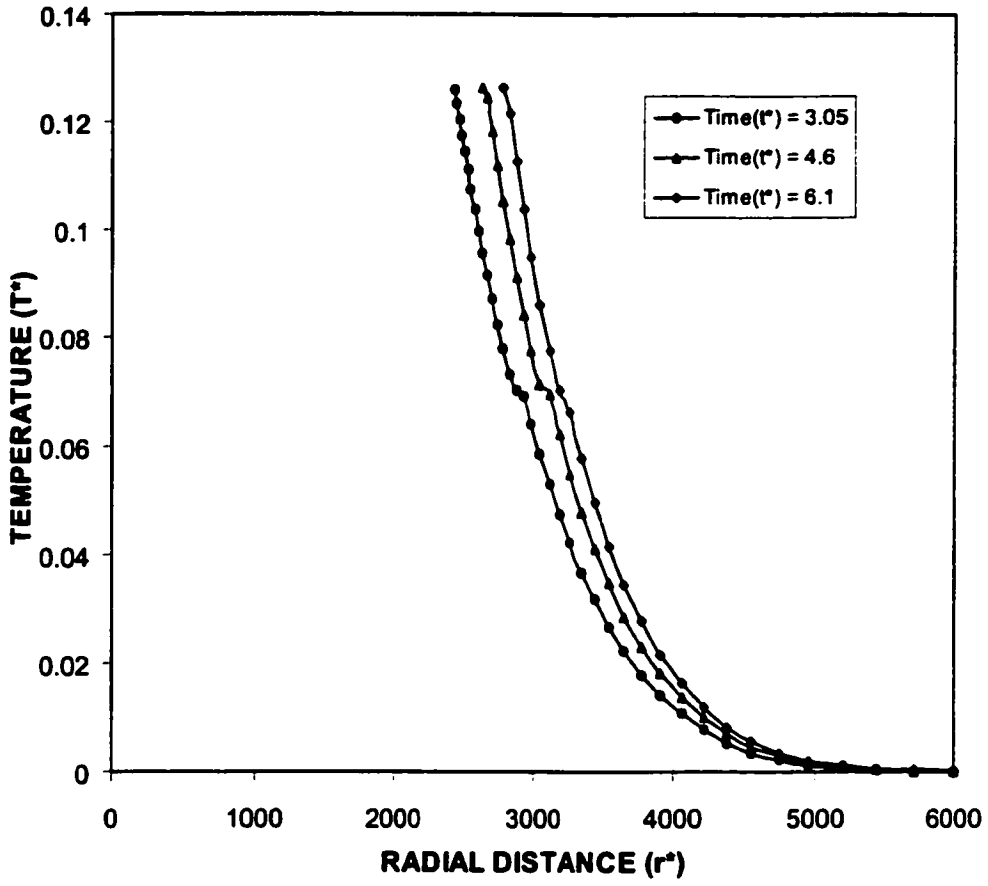

Figure 5.21: Variation of dimensionless temperature along dimensionless radial distance for different heating periods.

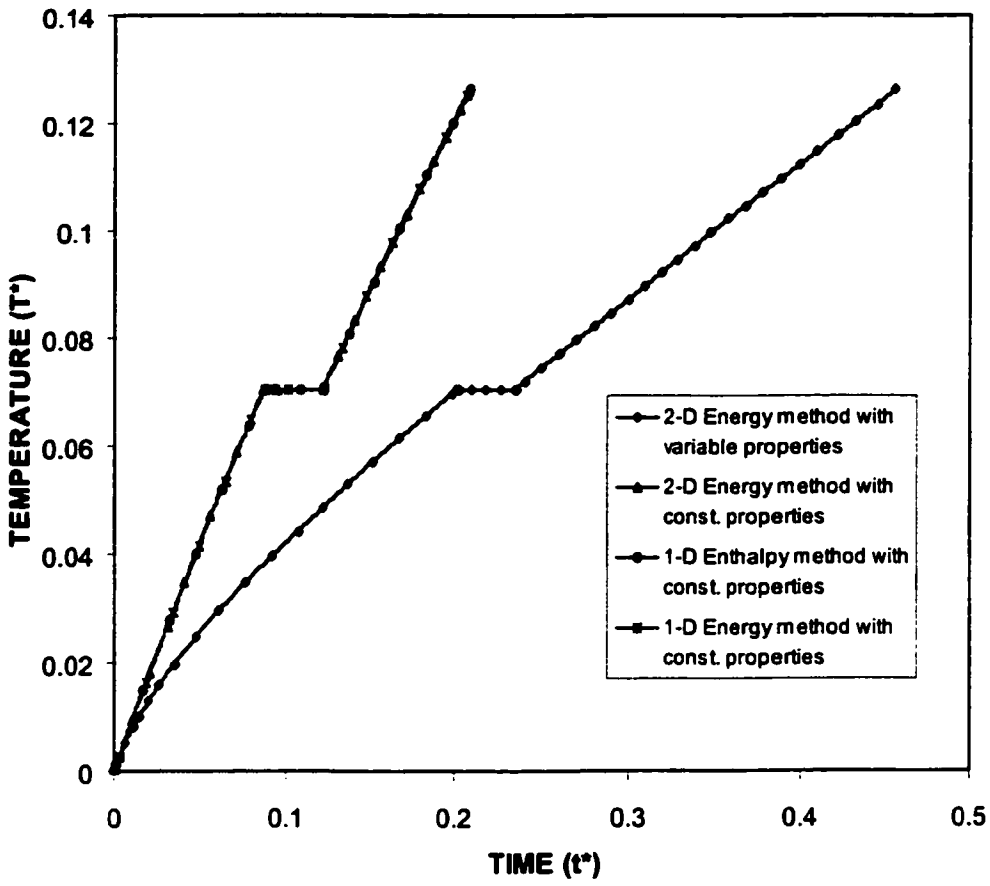

Figure 5.22: Temporal variation of dimensionless surface temperature obtained from energy and enthalpy methods for constant and variable properties.

temperature profiles is evident, since the specific heat capacity and thermal conductivity of the substrate material changes with temperature (Table 5.2). It should be noted that increasing temperature results in high specific heat capacity and low thermal conductivity; therefore, thermal diffusivity reduces with increasing temperature. The rise of surface temperature in the early heating period is higher as compared to that corresponding to late heating period. This occurs because of the internal energy gain of the substrate material in the surface vicinity during the early heating period. As the heating period increases, the temperature rise in the surface vicinity increases.. In this case, temperature differential across the surface vicinity and the region next to the surface vicinity increases. This enhances the temperature gradient and diffusional energy transport from surface vicinity to the solid bulk accelerates, i.e., the rate of surface temperature rise becomes low.

5.2.2 Stress Field for Non-Conduction Limited Heating

Figure 5.23 shows the dimensionless tangential stress component along the $z-$axis at different heating periods. The stress curves terminates inside the substrate material due to melt isotherms. The tangential stress component is compressive along the $z-$axis for all heating periods, Moreover, the level of the stress component increases to reach its maximum in the vicinity of the melt surface and as the axial distance from the melt surface increases towards the solid bulk it reduces to reach zero at some depth below the surface. This behavior is observed for all heating periods. This occurs because of i) thermophysical properties of the substrate material, in which case thermal diffusivity decreases slightly as temperature increases and the

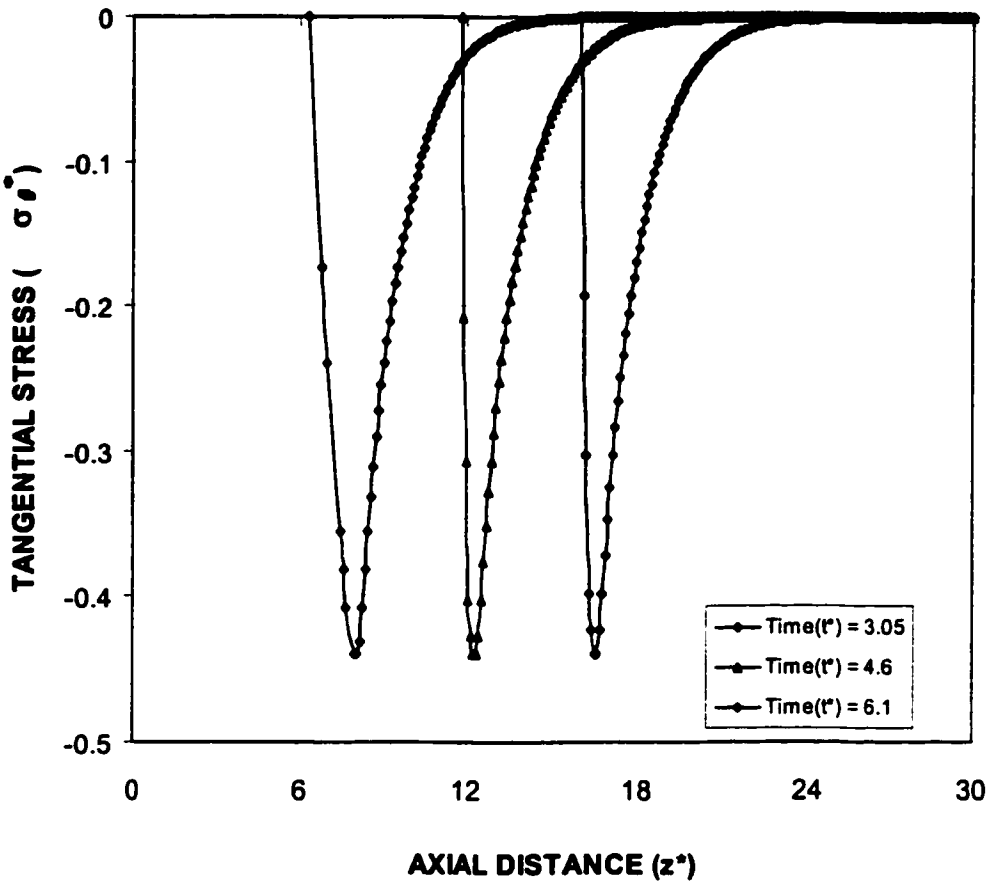

Figure 5.23: Variation of dimensionless tangential stress along dimensionless axial distance for different heating periods.

temperature gradient increases, and ii) expansion of the free surface, i.e. expansion of the free surface generates a high magnitude of strain below the surface, since stress free surface condition is employed in the analysis.

Figure 5.24 shows the dimensionless tangential stress components along the radial direction at different heating periods. In the region close to the melt surface ($r^* \leq 4500$) tangential stress component is compressive and it becomes tensile as the radial distance increases further away from the melt surface for all heating times. The magnitude of the stress component increases in the region close to the surface and its magnitude reduces sharply with radial distance. This is because of the free surface generated in the cavity, i.e. expansion of the substrate material generates a high strain region next to the free surface (cavity wall). The strain reduces to zero at the cavity wall, since it is free surface and no external forces is applied at the free surface. Consequently, tangential stress is zero at the melt surface.

Figure 5.25 shows the dimensionless radial stress component along the axial distance at different heating periods. The radial stress component is zero at the melt surface and the stress magnitude reaches maximum in the region close to the melt surface. The radial stress component is compressive. This is due to the free stress conditions at the melt surface and the thermal expansion in the region close to the free surface. It should be noted that zero stress component moves with the movement of the melt surface in the axial direction.

Figure 5.26 shows the dimensionless radial stress component along the radial direction at different heating periods. The magnitude of the stress component reduces as the heating progresses. Moreover, the peak of stress magnitude moves away from

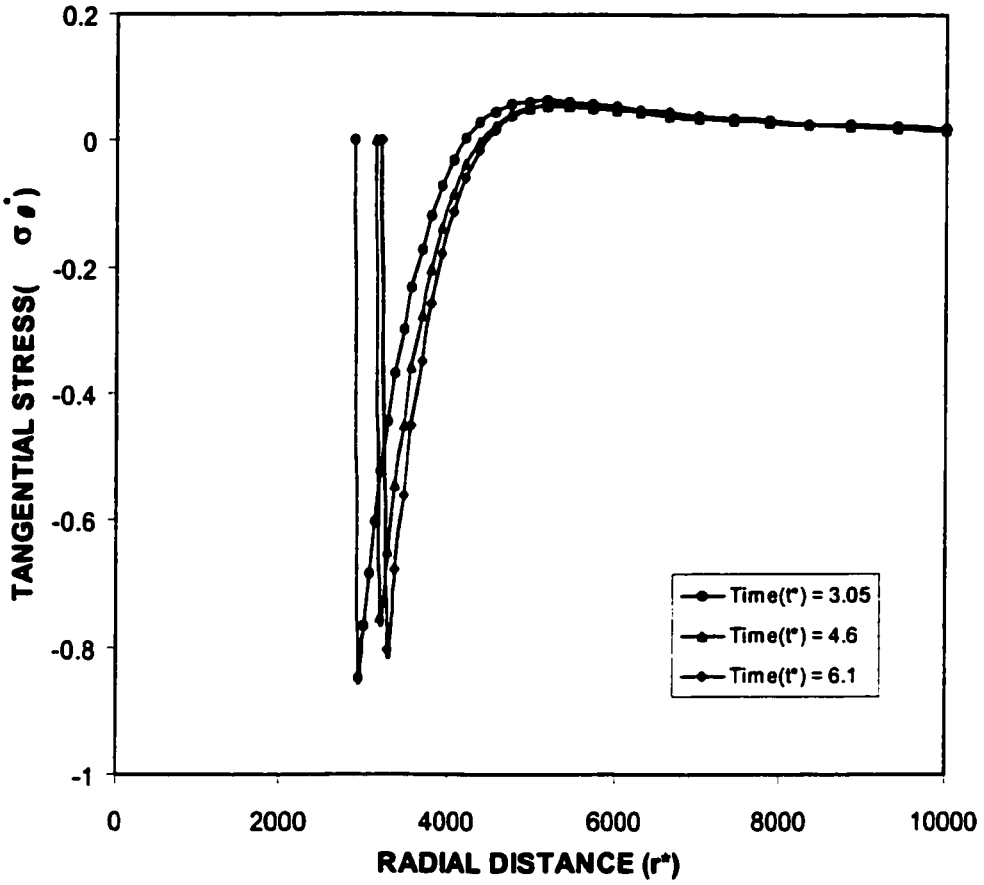

Figure 5.24: Variation of dimensionless tangential stress along dimensionless radial distance for different heating periods.

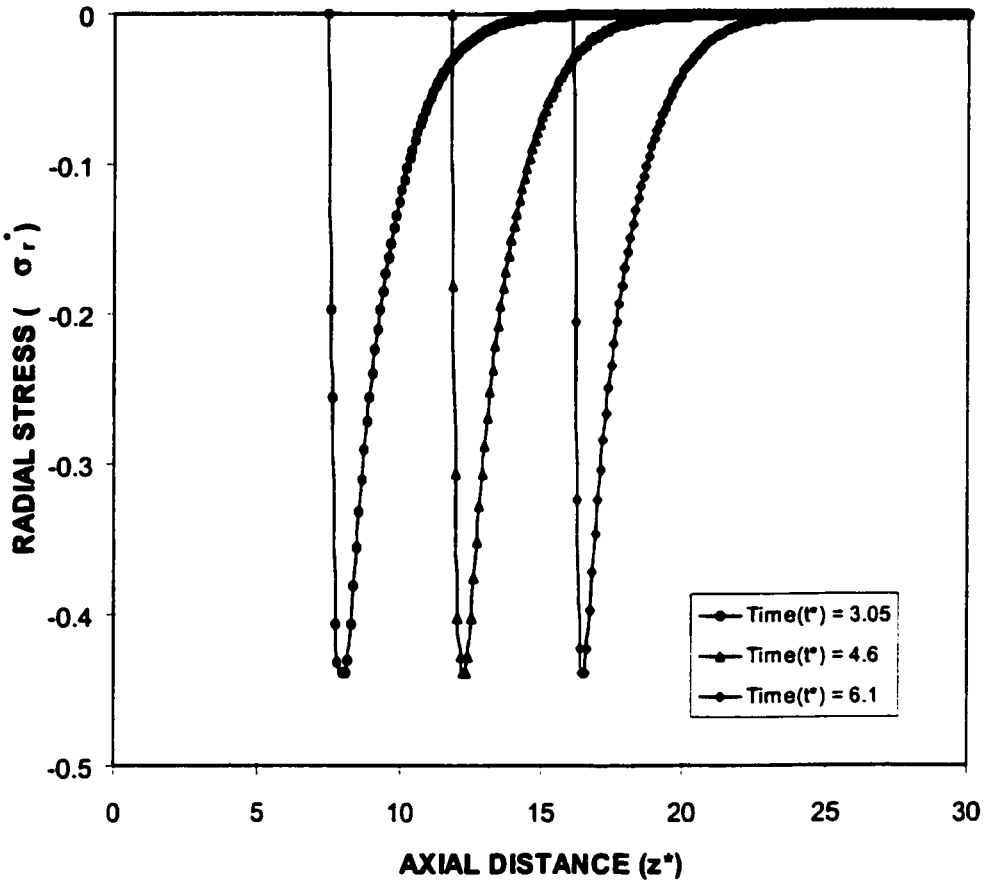

Figure 5.25: Variation of dimensionless radial stress along dimensionless axial distance for different heating periods.

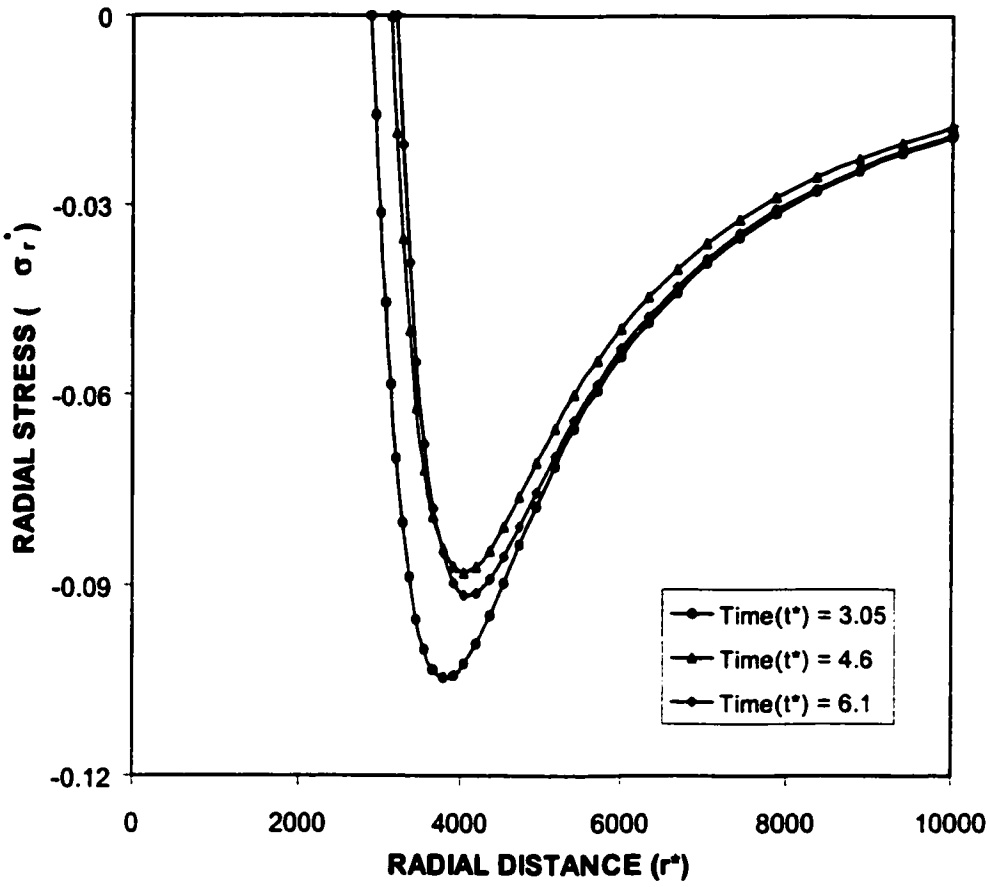

Figure 5.26: Variation of dimensionless radial stress along dimensionless radial distance for different heating periods.

the melt surface as the heating progresses. This occurs because of the temperature gradient in this region. Moreover, the stress component is compressive for all the heating periods.

Figure 5.27 shows the dimensionless equivalent stress contours inside the substrate material while Figure 5.28 shows dimensionless equivalent stress along the axial direction as heating period is variable. The equivalent stress is zero at the melt surface and increases sharply to maximum in the region close to the melt surface. This indicates that the stress level reduces in the region close to the melt surface, i.e. low temperature gradient results in low level of stresses in this region. The zero equivalent stress moves from the liquid surface as the heating period progresses. This is because of the recession velocity of the surface, which propagates into the solid bulk as the heating pulse progresses. The stress magnitude is high in the region below the liquid surface. Moreover, the stress gradient is slightly lower for the stress curve decreasing from its maximum towards the solid bulk as compared to that corresponding to stress curve decreasing from its peak towards the liquid surface. This is because of the temperature gradient, which has a similar trend in these regions.

Figure 5.29 shows the dimensionless equivalent stress in the radial direction at different heating periods for constant and variable properties. The magnitude of the equivalent stress attains higher values as compared to its counter part that corresponding to the constant properties case. In the case of variable properties, the equivalent stress has two peaks in the radial direction. The first peak occurs in the region close to the melt surface while the second peak is developed some depth below the melt surface. The location of first peak moves away from the liquid surface

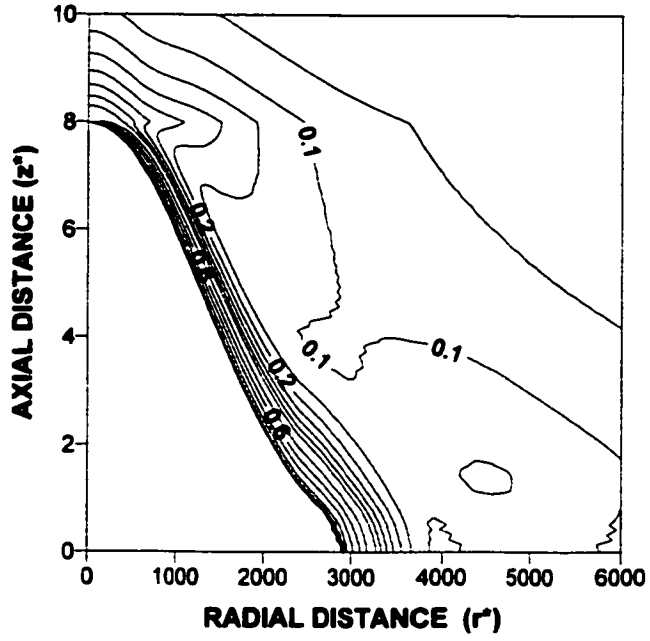

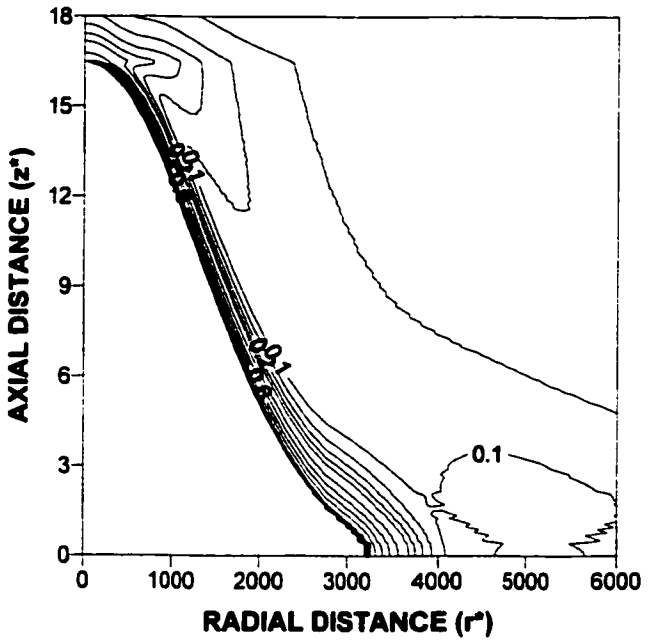

Figure 5.27: Equivalent stress contours for step input pulse at different heating periods.

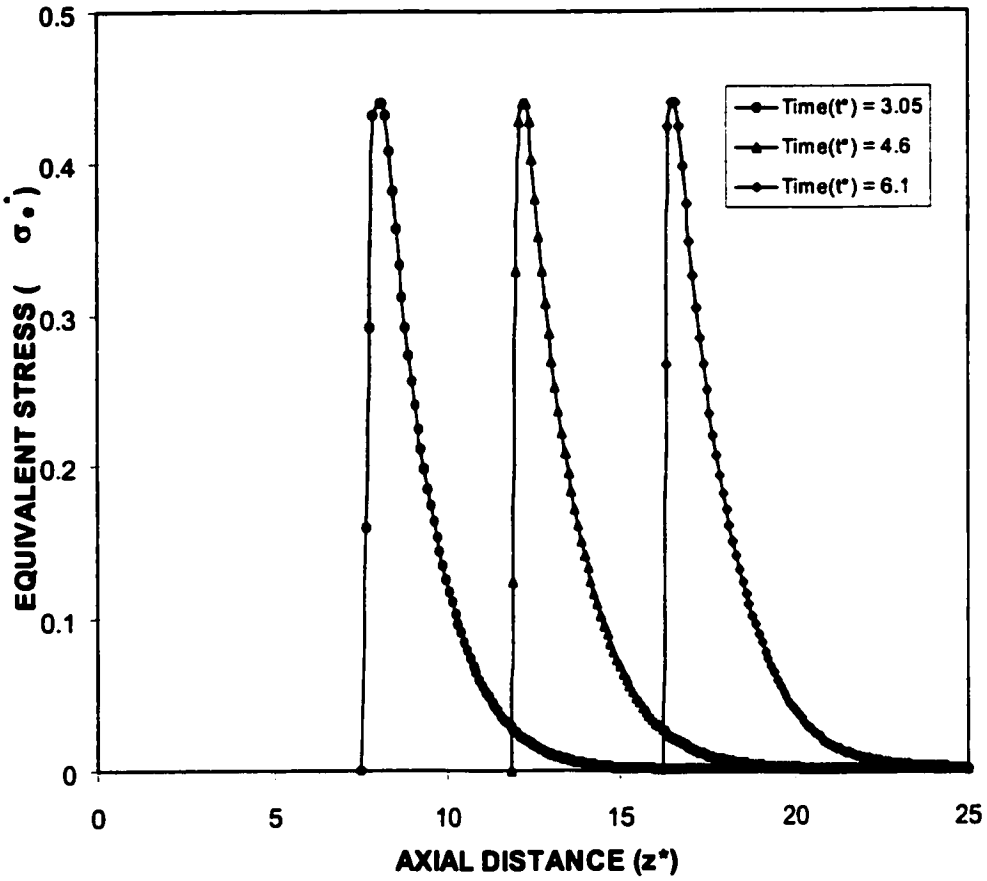

Figure 5.28: Variation of dimensionless equivalent stress along dimensionless axial distance for different heating periods.

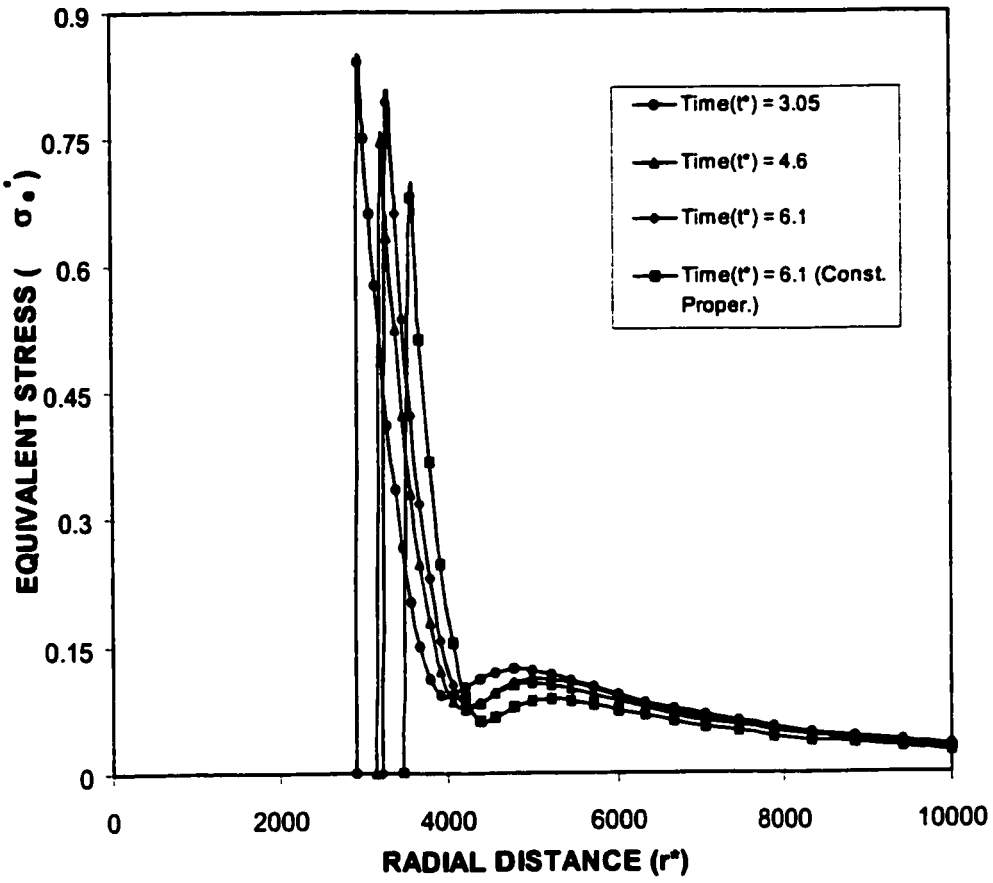

Figure 5.29: Variation of dimensionless equivalent stress along dimensionless radial distance for different heating periods.

while the location of the second peak moves towards the liquid surface as the heating progresses. The movement of first peak of the equivalent stress is because of the liquid surface, which moves towards the solid bulk at a velocity equal to a recession velocity as the heating progresses. The appearance of the second peak is because of the tangential stress component, in which case, it increases to become compressive in the radial direction at same depth below the liquid surface. Moreover, the magnitude of equivalent stress peak is low in the early heating period while the magnitude of the second peak of equivalent stress is higher in the early heating period as compared to those corresponding to late heating periods. This indicates that in the early heating period the expansion of the substrate material along the radial direction generates high stress center in the region some distance below the surface as well as in the region close to the surface. As the heating period progresses ,the second stress center at some depth below the surface gradually diminishes.

5.3 Non-Conduction Limited Heating Time Exponentially Varying Pulse Case

The numerical simulation of laser pulse heating of steel is carried out. The phase change processes including melting and evaporation are incorporated in the analysis. The temperature field in the substrate material and thermal stresses developed in the solid phase of the substrate material are computed for time exponentially varying laser heating pulse. The material properties and laser pulse used in the simulations are given in Tables 5.2 and 5.4.

5.3.1 Temperature Field for Conduction Limited Heating with Time Varying Pulse

Figure 5.30 shows the dimensionless temperature contours inside the substrate material for two pulse parameters $\left(\frac{\beta}{\gamma} = \frac{1}{2} \text{ and } \frac{\beta}{\gamma} = \frac{1}{4}\right)$. Temperature contour beyond 0.12 is not plotted, since the value 0.12 corresponding to the evaporation temperature, i.e. the empty space in the figure indicates the shape of the cavity generated after the evaporation process. The depth of the cavity extends further inside the substrate material for $\frac{\beta}{\gamma} = \frac{1}{4}$ despite the fact that peak power intensity for both pulses are the same (Figure 5.31). In this case, the pulse intensity rise rapidly and attains high values for $\frac{\beta}{\gamma} = \frac{1}{4}$ as compared to that corresponding to $\frac{\beta}{\gamma} = \frac{1}{2}$. The rapid rise of the pulse intensity enhances the heating process during the early heating period. The size of the cavity at the surface of the substrate material is in the order of $40\mu m$ $(r^* = 2500)$, after about 0.6 ns heating pulse $(t^* = 6.1)$, which is almost the same as the irradiated spot size. Moreover, for pulse parameter $\frac{\beta}{\gamma} = \frac{1}{2}$, this reduces slightly.

Figure 5.32 shows temperature profiles inside the substrate material at $r-$axis location is zero $(r^* = 0)$ for different heating periods. The temperature profiles up to the evaporation temperature are shown. Temperature profiles reduces sharply in the liquid region and the decay is almost gradual in the solid region. This can also be seen from Figure 5.33, in which temperature gradient $\left(\frac{\partial T^*}{\partial z^*}\right)$ is shown inside the substrate material. Temperature gradient changes sharply in the melt region $(.07 < T^* < .12)$ while change is relatively gradual in the solid region $(T^* < .07)$. The region of melting is evident from $\frac{\partial T^*}{\partial z^*}$ curve, in which case, $\frac{\partial T^*}{\partial z^*}$ changes at the point of phase change.

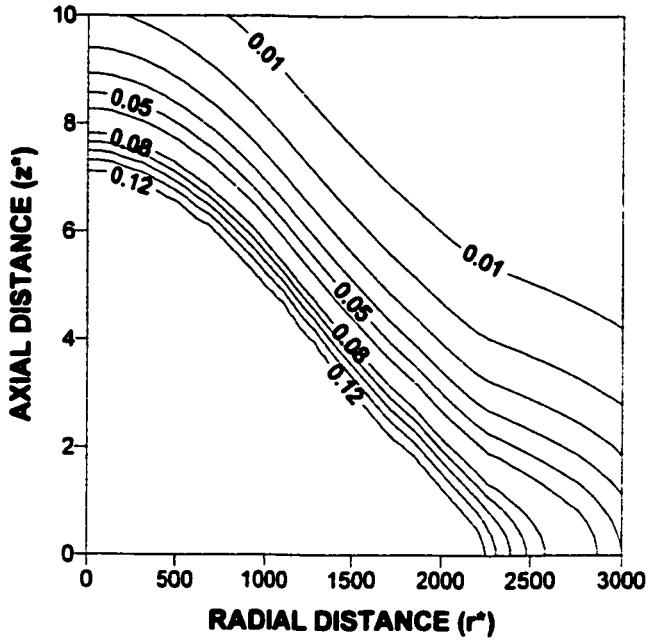

$\beta/\gamma = 1/2$

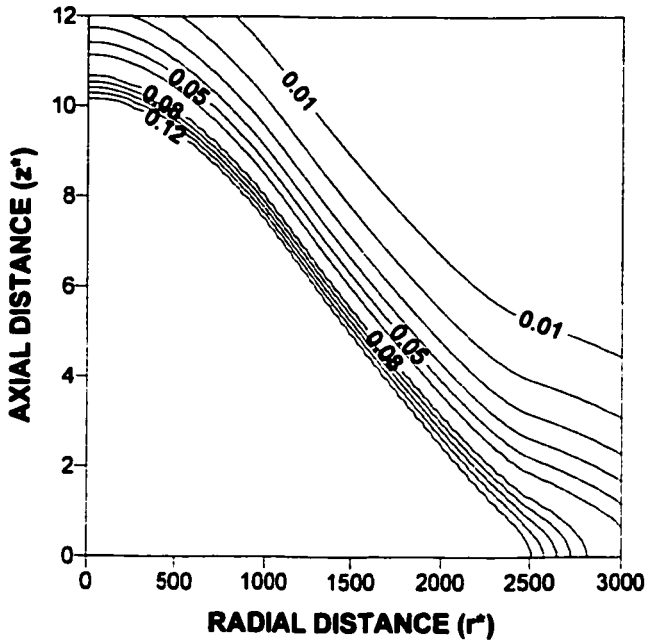

$\beta/\gamma = 1/4$

Figure 5.30: Temperature contours at Time (t*) = 6.1

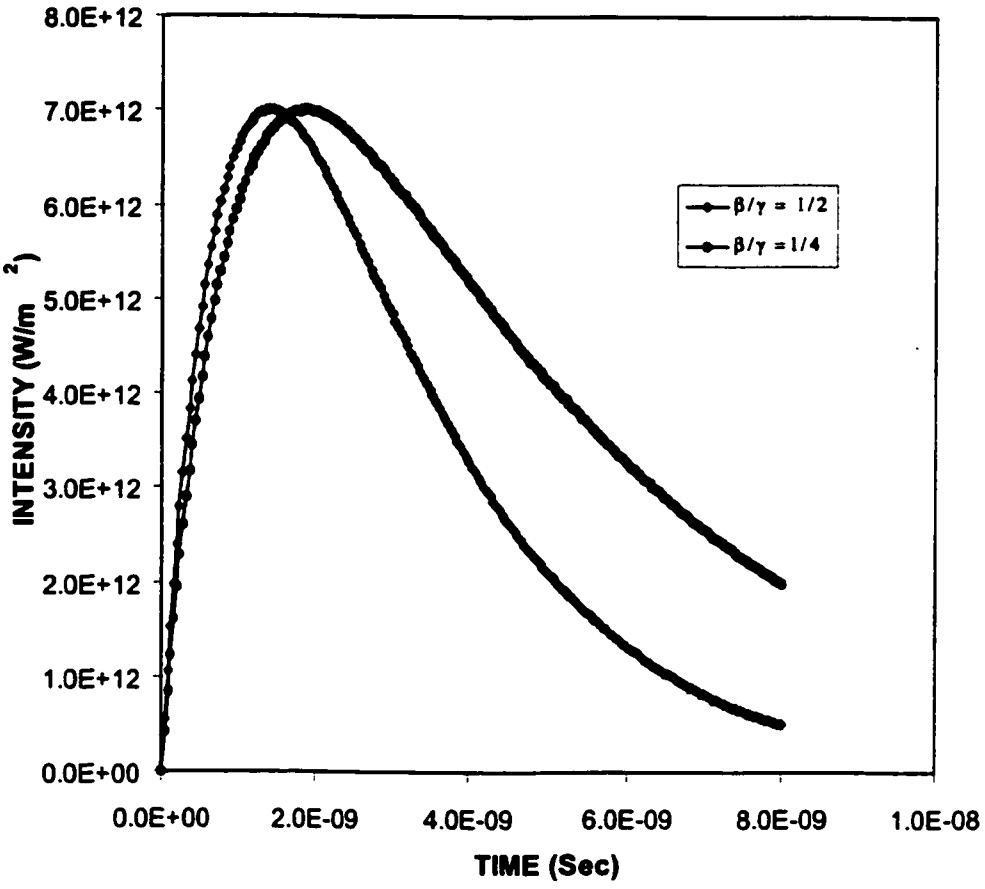

Figure 5.31: Power intensity distribution with time for time exponentially varying pulse.

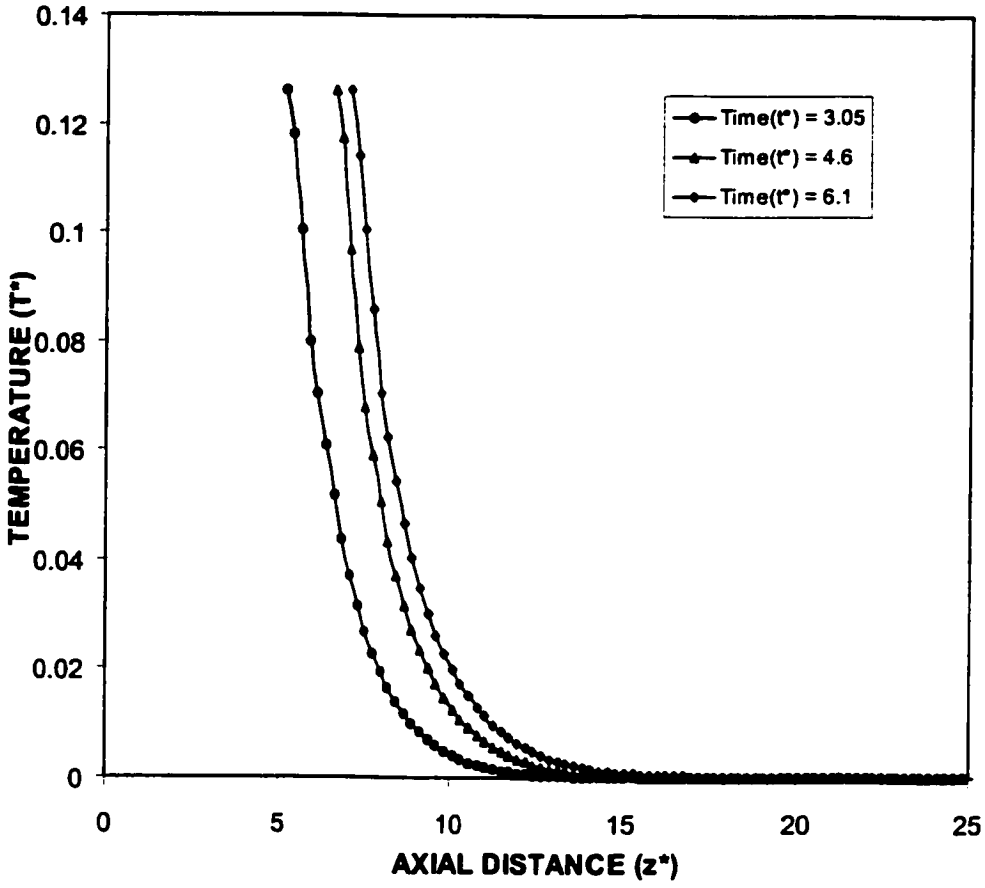

Figure 5.32: Variation of dimensionless temperature along dimensionless axial distance for different heating periods.

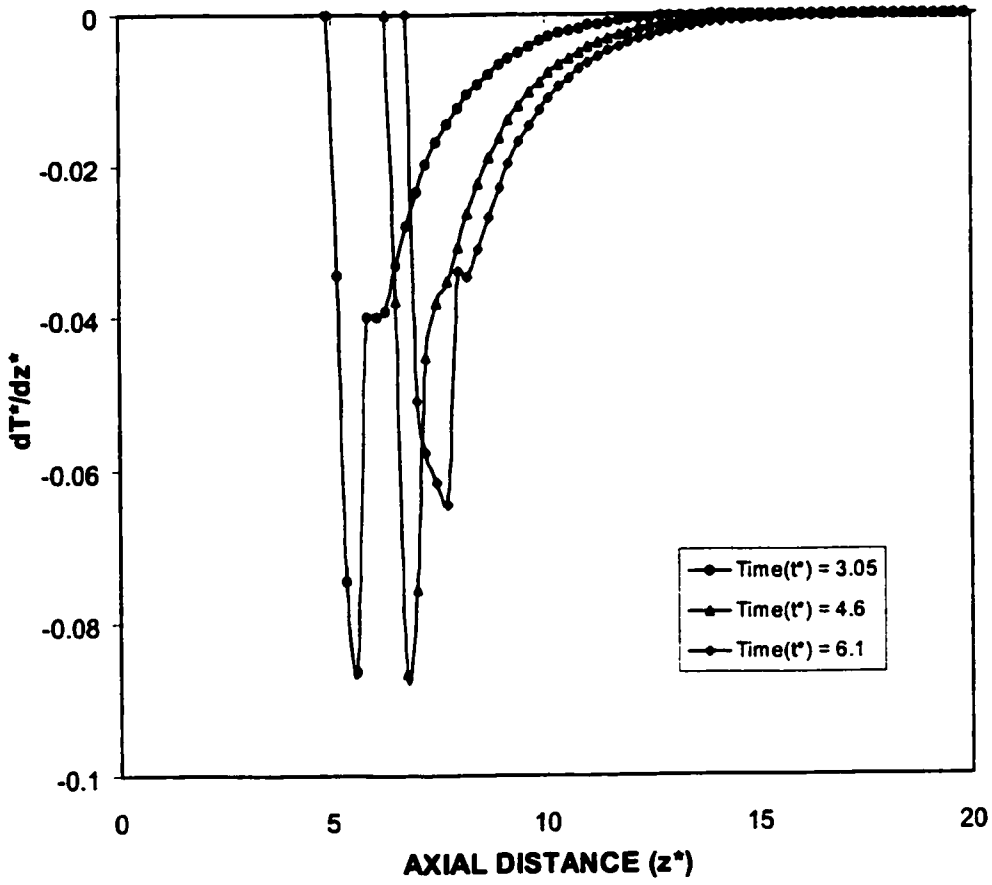

Figure 5.33: Variation of dimensionless temperature gradient along dimnsionless axial distance for different heating periods.

Moreover, $\frac{\partial T^*}{\partial z^*}$ reduces to reach its minimum before it increases. Although $z-$axis location ($z^* = 6.2$) is beyond the absorption depth, the heat diffusion across the liquid-solid interface increases considerably the internal energy gain of the substrate material. Consequently temperature gradient attains high values. As the depth increases further, the temperature gradient increases gradually. This occurs because of the diffusional energy transport, i.e. in the solid next to the melt region, large temperature gradient accelerates the diffusional energy transport from this region to bulk of the substrate material; however, as the depth below the surface increases further, temperature gradient becomes less and diffusional energy transport towards the solid bulk reduces. This is more pronounced in the early heating period. As the heating period progresses ($t^* > 4.5$), the decay rate of temperature profiles becomes almost same.

Figure 5.34 shows the dimensionless temperature distribution along the radial direction at $z-$axis location is zero ($z^* = 0$) for different heating periods. The widths of evaporated, melted and solid heated zones are evident. This can also be seen from Figure 5.35, in which temperature gradient in the radial direction $\left(\frac{\partial T^*}{\partial r^*}\right)$ is shown. The temperature gradient reduces sharply in the melt region and decay of gradient reduces as the distance from the irradiated spot center increases towards the edge of the heated spot. Moreover, the decay of the temperature in the radial direction did not follow the pulse intensity profile in the same direction, i.e. temperature decay rapidly towards the edge of the heated spot. The variation of temperature distribution in the radial direction with heating period is not considerable. This is because of the time exponentially varying pulse, in which case, peak intensity does

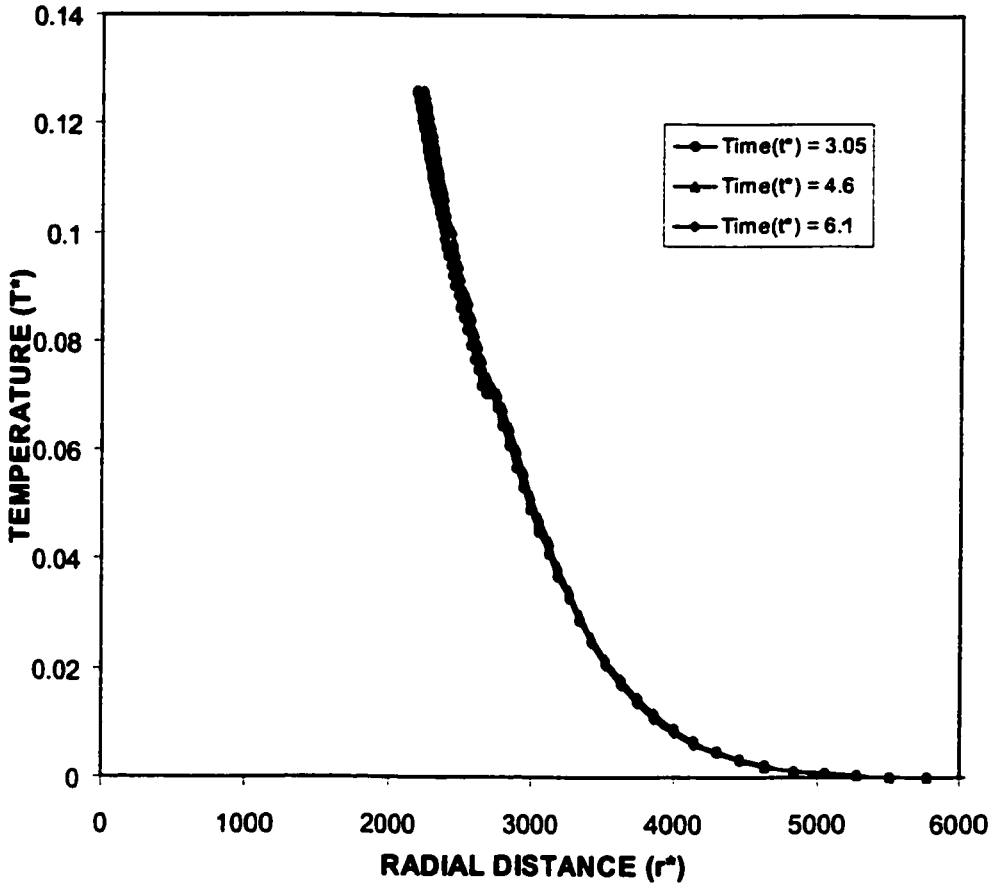

Figure 5.34: Variation of dimensionless temperature along dimensionless radial distance for different heating periods.

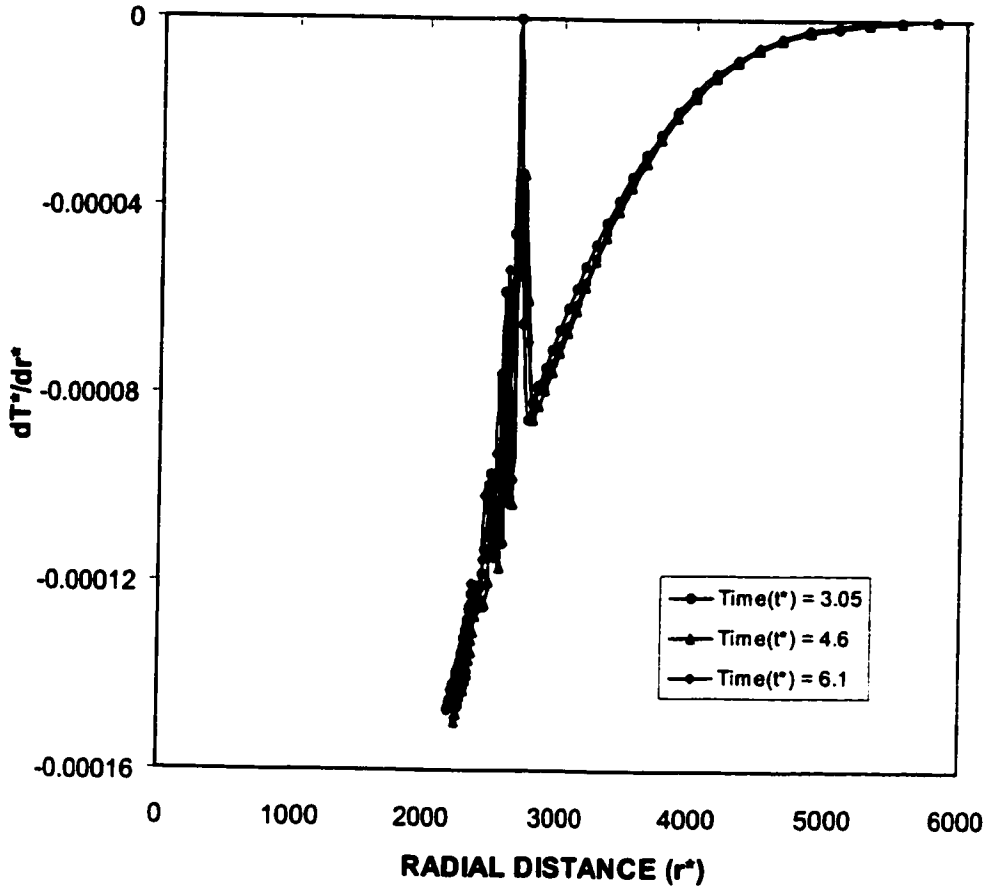

Figure 5.35: Variation of dimensionless temperature gradient along dimensionless radial distance for different heating periods.

not alter considerably within the heating period considered (Figure 5.31).

Figure 5.36 shows temporal variation of surface temperatures obtained from enthalpy and energy methods for constant and variable properties for comparison. Temperature profiles are obtained from one-dimensional analysis, since the analysis related to the enthalpy method is one-dimensional. It can be seen that the results obtained from enthalpy and present model are in good agreement. Moreover, the effect of variable properties on temperature profiles are evident. In this case, the rate of temperature rise becomes less for the variable properties case, i.e. the specific heat capacity and thermal conductivity reduce with increasing temperature, which in turn alters the heat diffusion rates inside the substrate material.

5.3.2 Stress Field for Non-Conduction Limited Heating with Time Varying Pulse

Figure 5.37 shows the dimensionless tangential stress component along the axial direction as dimensionless heating periods are variable. Tangential stress component is compressive, provided that stress level at the melt boundary is zero, i.e. free stress condition is set at melt surface in the simulations. The magnitude of stress component increases sharply as the distance from the melt surface, reaching its maximum before decreasing sharply to at some depth below the surface. The behavior of stress component in the axial direction is because of the temperature gradient, in which case, the magnitude of temperature gradient in this region decays sharply. As the heating period progresses, the magnitude of maximum stress remains the same, how-

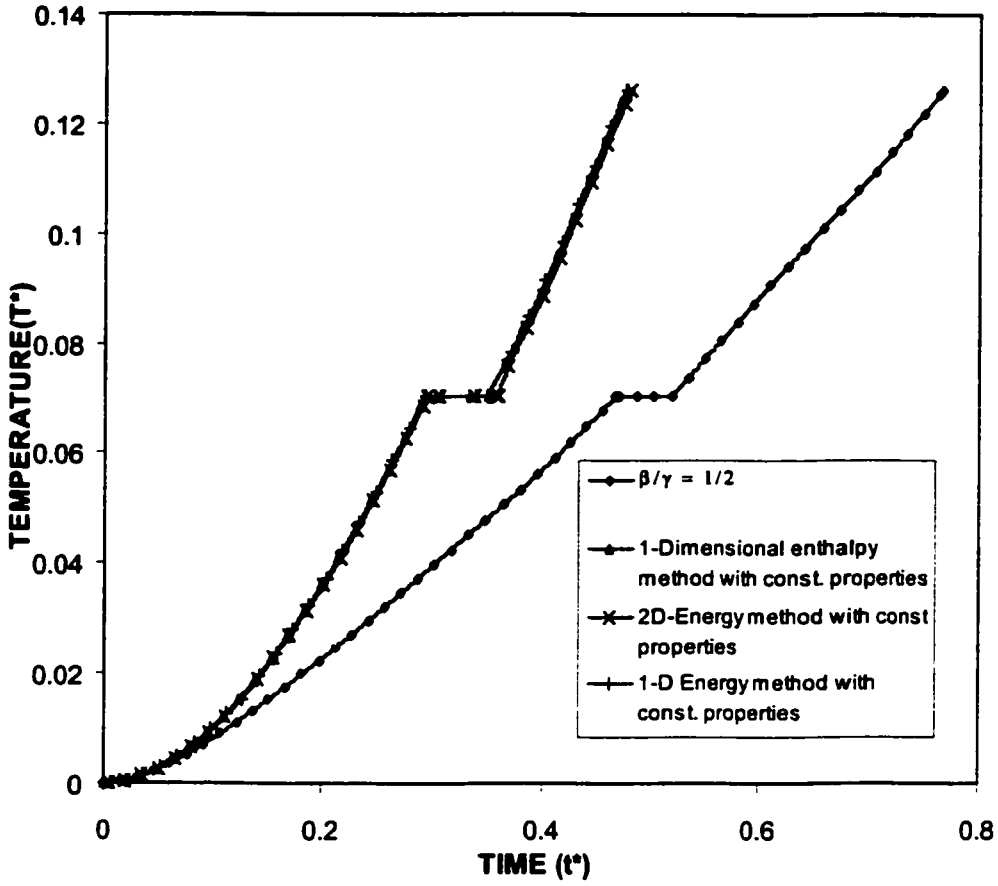

Figure 5.36: Temporal variation of dimensionless surface temperature obtained for enthalpy and energy methods.

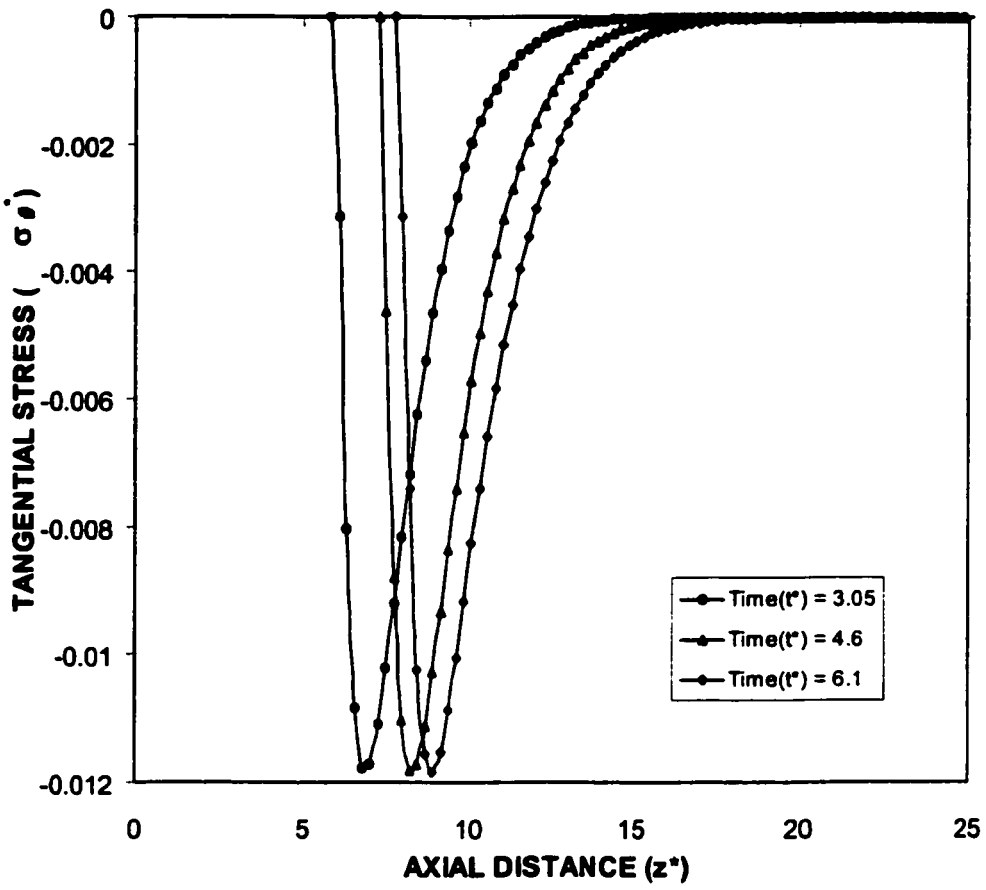

Figure 5.37: Variation of dimensionless tangential stress along dimensionless axial distance for different heating periods.

ever, its location moves away from the center of the heated spot. This occurs because of the advancement of the melt surface in the axial direction as the heating period progresses. Moreover, the behavior of tangential stress gradients corresponding to different heating periods is almost same. This is due to the surface temperature gradient behavior with time.

Figure 5.38 shows the dimensionless tangential stress component along the radial distance as the dimensionless heating period is variable. The tangential stress component is compressive in the region close to the irradiated spot center and it becomes tensile as the distance from the spot center increases towards the edge. This is because of the thermal strain generated in this region, i.e. thermal expansion results in contraction in the region close to the irradiated spot center. The magnitude of stress component increases sharply to reach its maximum in the region below the melt zone and it reduces sharply to zero as the radial distance increases. Moreover, increasing the radial distance further towards the solid bulk results in increase in the stress component, provided that the stress component becomes tensile. The level and stress profile remain almost same with time.

Figure 5.39 shows the dimensionless radial stress component along the radial-axis as dimensionless heating periods are variable. Radial stress component is compressive, which is because of the thermal strain developed in the radial direction. The magnitude of stress component increases sharply to reach its peak and decays gradually as the distance in the radial direction increases away from the irradiated spot center. The location of maximum stress component remains the same for all the heating periods considered, however, its magnitude increases with progressing heat-

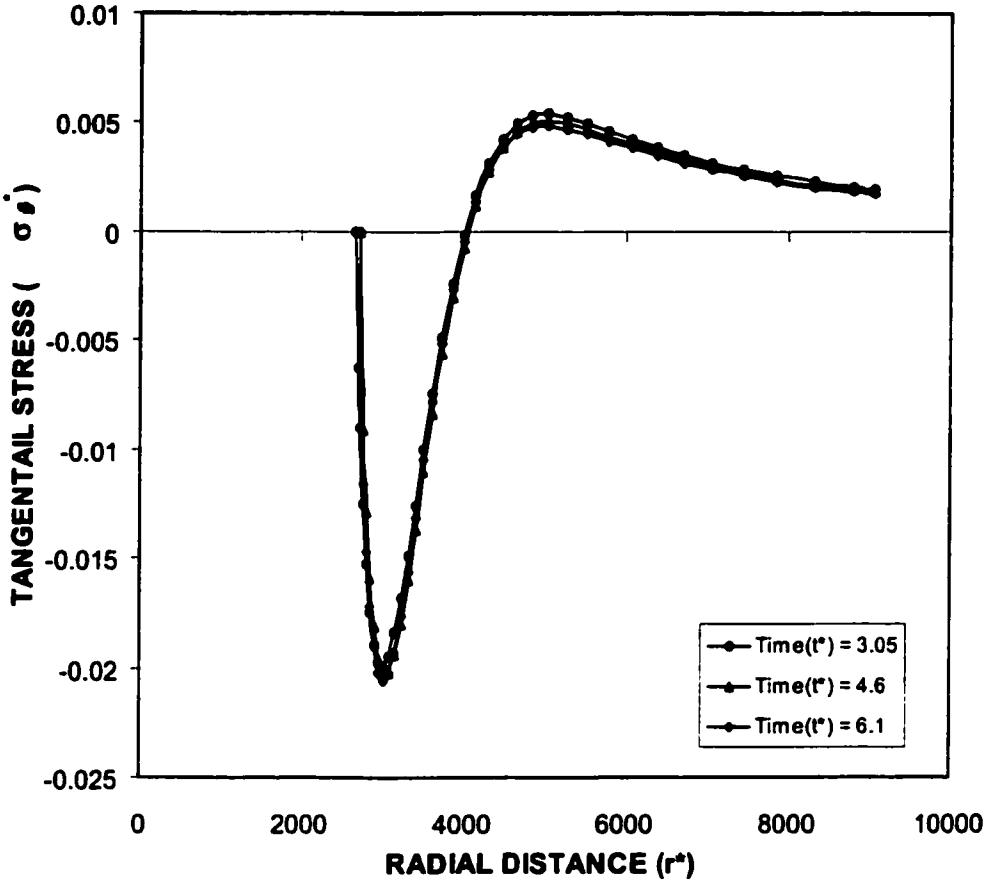

Figure 5.38: Variation of dimensionless tangential stress along dimensionless radial distance for different heating periods.

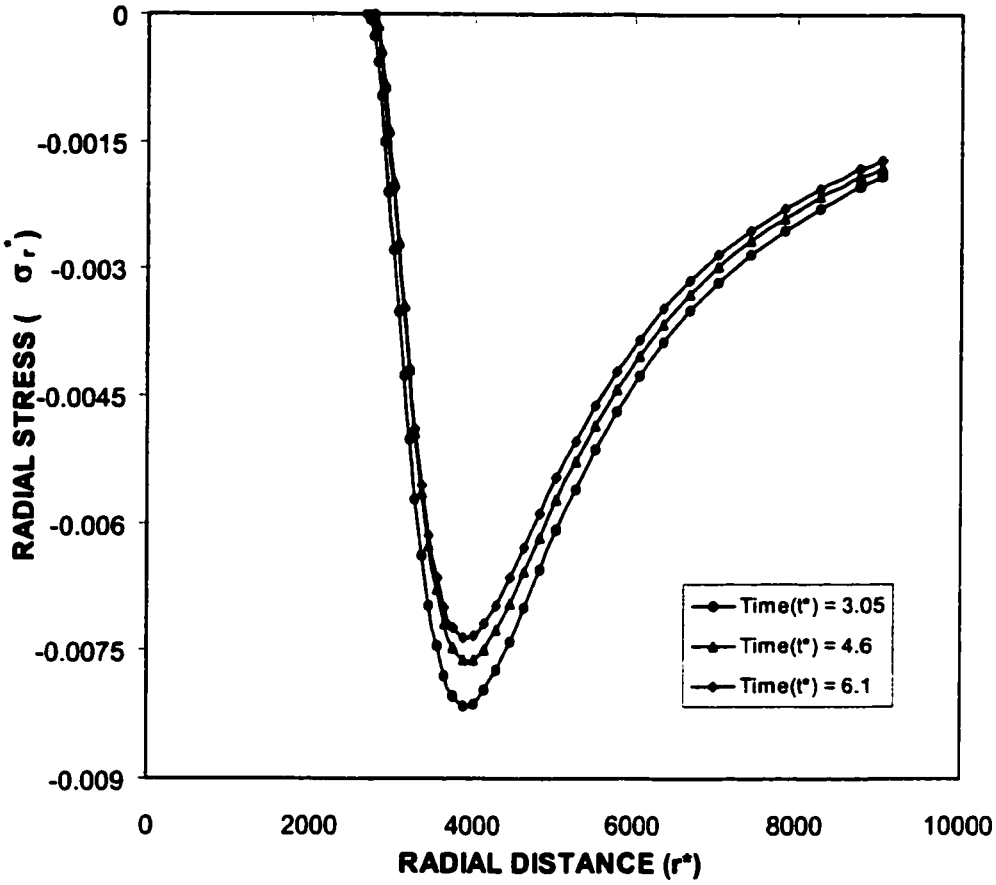

Figure 5.39: Variation of dimensionless radial stress along dimensionless radial distance for different heating periods.

ing period. Moreover, stress gradient increases in the region close to the irradiated spot center as the heating progresses. This occurs because of the radial temperature gradient, which increases slightly in this region with progressing heating period.

Figure 5.40 shows the 3-dimensional plot of dimensionless equivalent stress for two dimensionless heating periods. The equivalent stress level varies considerably along the axial and radial directions. Figure 5.41 shows the dimensionless equivalent stress along the radial distance as heating periods are variable. The magnitude of stress increases sharply to reach its maximum in the region next to the melt zone. As the radial distance increases away from the melt surface stress level reduces to reach minimum. As the distance increases further, the stress level increases reaching its second peak, provided that the magnitude of the second peak is less than that corresponding to the first peak. Moreover, the rise of second peak is gradual while the rise of first peak is sharp. The generation of second peak is because of the radial component of the tangential stress, which becomes tensile in this region. The influence of heating period on the equivalent stress is more pronounced for the second stress peak. In this case, the magnitude of stress level reduces as the heating period progresses.

Figure 5.42 shows the dimensionless equivalent stress along the axial direction as dimensionless heating period is variable. equivalent stress increases sharply to reach its maximum in the region next to the melt surface. As the radial distance increases further towards the irradiated spot edge it decays gradually. This occurs because of the tangential stress component (Figure 5.38), in which case, behaviors of equivalent and tangential stress levels in the radial direction are almost identical.

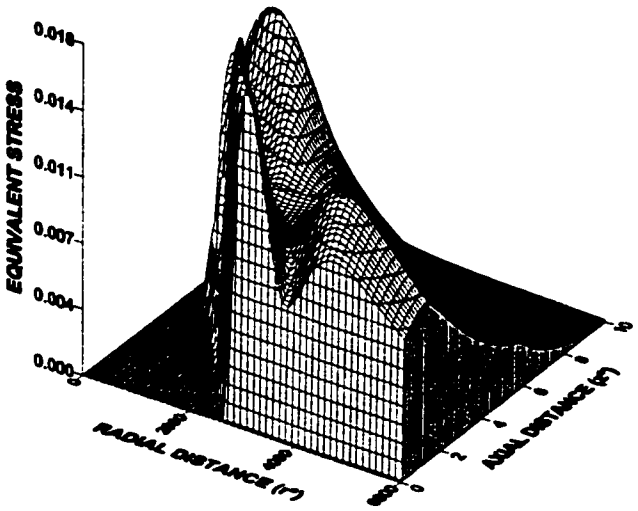

Figure 5.40: Equivalent stress surface plot for time exponential pulse at different heating periods.

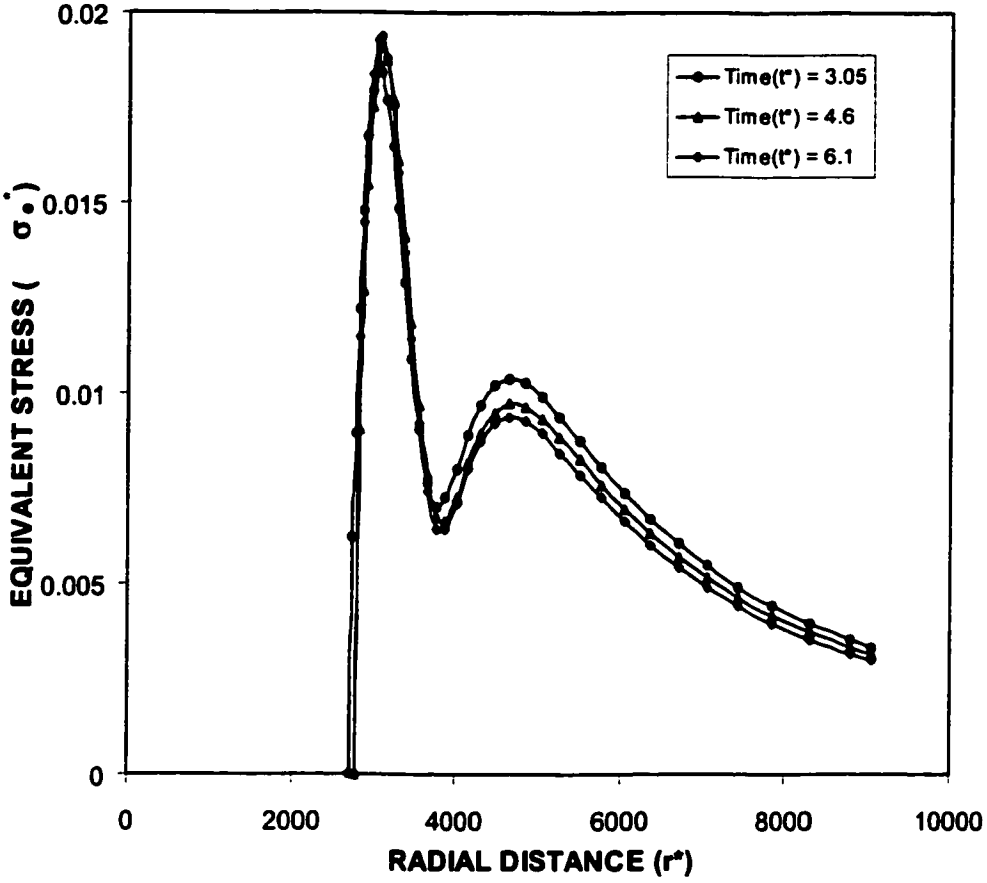

Figure 5.41: Variation of dimensionless equivalent stress along dimensionless radial distance for different heating periods.

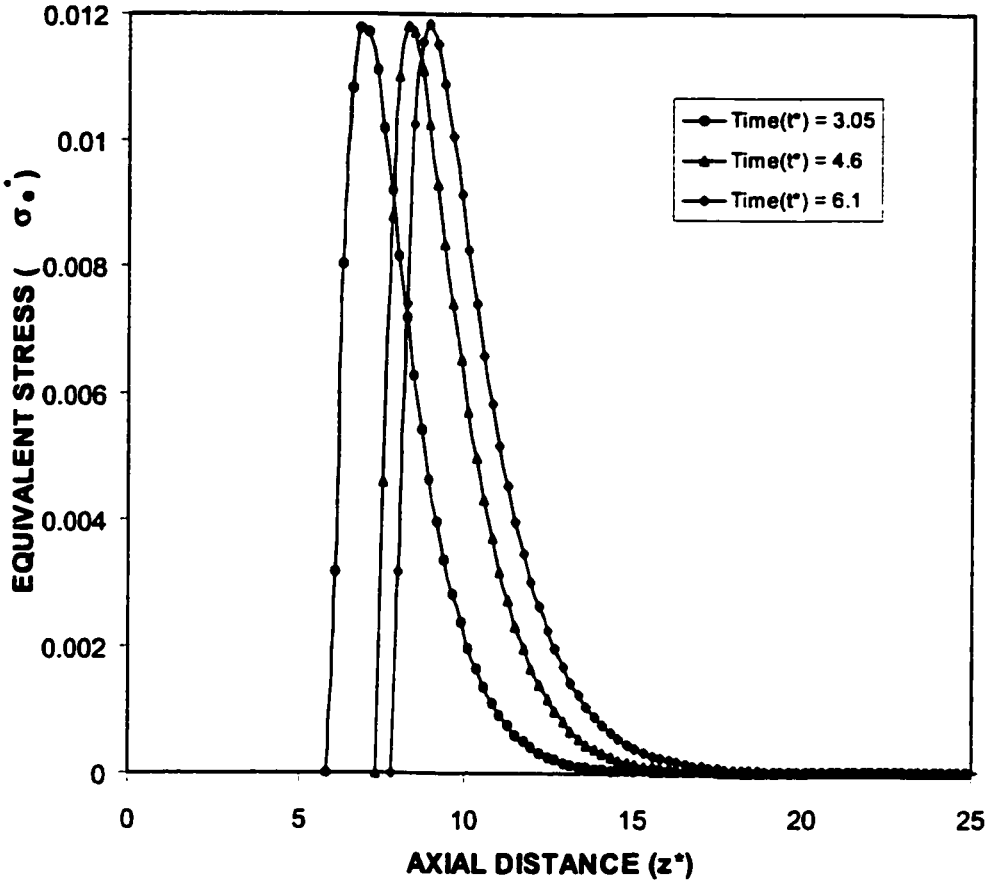

Figure 5.42: Variation of dimensionless equivalent stress along dimensionless axial distance for different heating periods.

The maximum equivalent stress moves towards the solid bulk as the heating period progresses, provided that the stress gradients during rise and fall do not change much for different heating periods. The change of maximum stress location is because of; i) advancing of melt surface towards the solid bulk with progressing of heating period, and ii) temperature profile next to the melt zone does not alter considerably for different heating periods.

5.4 Validation

To validate some of the results pertinent to conduction limited heating case, we compare the prediction of conduction limited heating in one-dimensional form with the results of analytical solution [78]. One dimensional heat conduction equation with constant properties for laser heating is given as:

$$\rho c_p \frac{\partial T}{\partial t} = k \frac{\partial^2 T}{\partial x^2} + I_o \delta \exp(-\delta x) \tag{5.1}$$

with boundary conditions as:

$$\begin{aligned} \frac{\partial T}{\partial x} &= 0 \ \ at \ \ x = 0 \ \ \text{(at surface)} \\ T &= T_o \ \ \text{(Specified)} \ \ at \ \ x \rightarrow \infty \ \ \text{(at infinity)} \end{aligned}$$

and initial condition:

$$T = T_o \ \ \text{(Specified)} \ \ at \ \ t = 0 \ \ \text{(initially)}$$

Equations (5.1) can be non-dimensionlized through introducing the following dimensionless parameters:

$$x^* = \delta x$$

$$t^* = \alpha\delta^2 t$$

$$T^* = \frac{Tk\delta}{I_o}$$

After introducing the dimensionless parameters, equations (5.1) for constant properties yield:

$$\frac{\partial T^*}{\partial t^*} = \frac{\partial^2 T^*}{\partial x^{*2}} + \exp(-x^*) \tag{5.2}$$

Non-dimensional boundary conditions take the form as:

$$\frac{\partial T^*}{\partial x^*} = 0 \ \ at \ \ x^* = 0 \ \ \text{(at surface)}$$

$$T^* = \frac{T_o k\delta}{I_o} \ \ \text{(Specified)} \ \ at \ \ x^* \to \infty \ \ \text{(at infinity)}$$

Non-dimensional initial condition is,

$$T^* = \frac{T_o k\delta}{I_o} \ \ \text{(Specified)} \ \ at \ \ t^* = 0 \ \ \text{(initially)}$$

Solution of the equation (5.2) is given as [78]:

$$\begin{aligned} T^*(x^*,t^*) &= \frac{1}{2}\left\{4\sqrt{t^*}\text{ierfc}\left[\frac{x^*}{2\sqrt{t^*}}\right]\right. \\ &\quad + \exp(t^*-x^*)\,\text{erfc}\left[\sqrt{t^*}-\frac{x^*}{2\sqrt{t^*}}\right] \\ &\quad \left. + \exp(t^*+x^*)\,\text{erfc}\left[\sqrt{t^*}+\frac{x^*}{2\sqrt{t^*}}\right] - 2\exp(-x^*)\right\} \end{aligned} \tag{5.3}$$

The growth of surface temperature with time may be obtained by putting $x = 0$ in equation (5.3), with the result:

$$T^*(0,t^*) = 2\left(\frac{t^*}{\pi}\right)^{1/2} + \exp(t^*)\,\text{erfc}\left[\sqrt{t^*}\right] - 1 \tag{5.4}$$

Figure 5.43 showes the results obtained from equation (5.4) and from numerical solution. It can be observed that both results are in good agreement with almost no discrepancy.

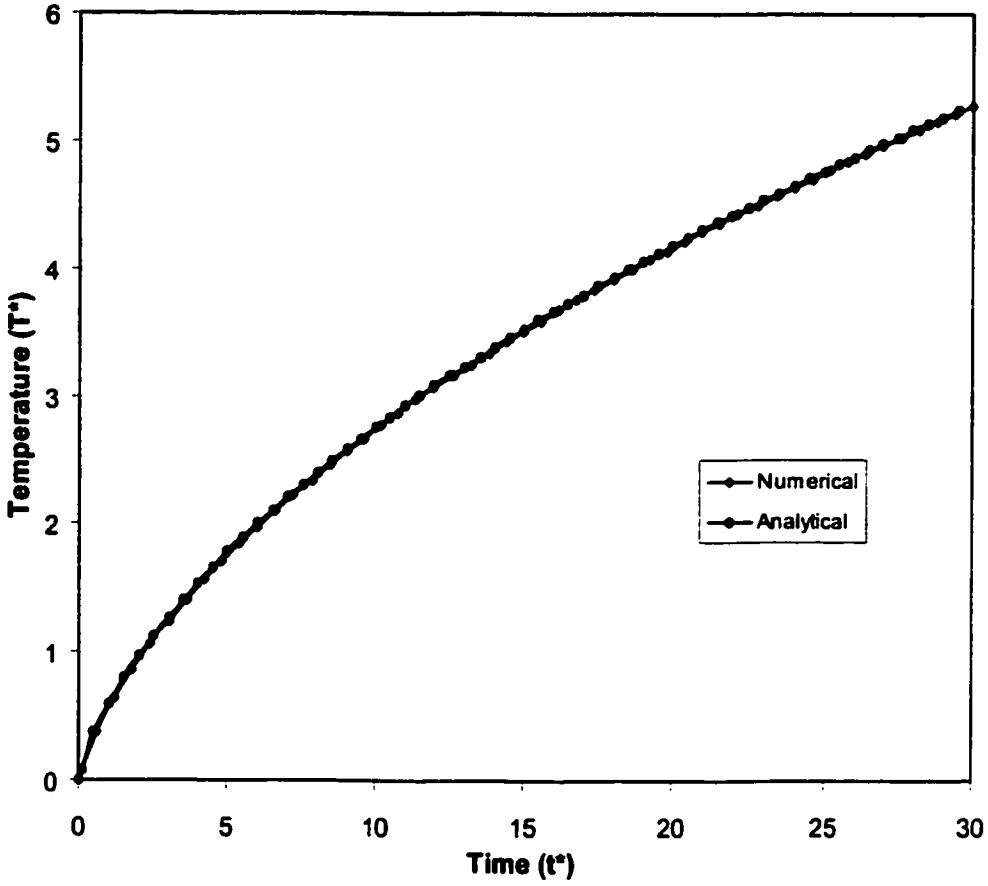

Figure 5.43: Comparision of dimensionless surface temperature along dimensionless time for numerical and analytical solutions.

c_p J/KgK	k W/mK	ρ kg/m^3	α m^2/s	α_T $1/K$	δ $1/m$	ν	E GPa	a m	$I_o(1-r_f)$ W/m^2
106	80	7870	9.59×10^{-5}	16×10^{-6}	6.16×10^{7}	.3	270	32500	1.4×10^{11}

Table 5.1: Thermophysical properties of the substrate material and beam properties used in simulation for conduction limited heating.

	δ (1/m)	ρ (kg/m^3)	Cp(J/KgK) ($Cp_m = Cp_b = Cp$ at $T = T_m$)	k (W/mK) ($k_m = k_b = k$ at $T = T_m$)	T_m (K)
Constant Properties	6.16×10^{7}	7836	330	52	1810
Variable Properties	6.16×10^{7}		24.558+1.223×T -0.37693$\times10^{-3}$T^2	64.102-0.04803T +1.518$\times10^{-5}$T^2	
L_m (J/kg)	L_b (J/kg)	E (GPa)	ν	α_T $\times10^{-6}$(1/K)	T_b (K)
2.4×10^{5}	6.26×10^{6}	11.7	0.3	217.96	3030

Table 5.2: Properties of substrate material used in computation.

Pulse Intensity (W/m^2)	Gaussian Parameter a (1/m)	Heating period (ns)
7×10^{12}	3.266×10^{3}	$0-8$

Table 5.3: Pulse properties for step input pulse.

Pulse Intensity (W/m^2)	Gaussian Parameter a (1/m)	Heating period (ns)	β (1/s)	γ (1/s)
7×10^{12}	3.266×10^{3}	$0-8$	0.5×10^{9}	1×10^{9}

Table 5.4: Pulse properties for time exponentially varying pulse.

Chapter 6

CONCLUSIONS

We have considered in our study both conduction limited and non-conduction limited heating cases. We modeled phase change from solid to liquid and liquid to gas. We also studied the thermal stresses developed in substrate material due to laser heating. We obtain the following conclusions about each type of heating process:

6.1 Conduction Limited Heating

In general, it is found that the radial stress component is compressive, axial stress component is tensile while tangential stress component is compressive in the region close to the symmetry axis and it is tensile as the distance increases further away from the symmetry axis. The specific conclusions derived in this study can be listed as follows:

1. Temperature in the radial direction does not follow exactly the pulse intensity profile. The temperature gradient in the radial direction becomes small in the region close to the symmetry axis. As the distance increases the temperature gradient changes sharply.

2. In the early heating period temperature rises rapidly in the region irradiated by a laser beam, especially in the surface vicinity. In this case, the energy

absorbed from the irradiated field is converted into internal energy gain of the substrate material and since the temperature gradient is low in the early heating period, diffusional energy transport becomes less towards to the bulk of the solid material. Consequently, internal energy gain dominates the diffusional energy transport in the surface vicinity. As the heating progresses, temperature gradient attains high values and the diffusional energy transport to the solid bulk enhances. In this case, time derivative of temperature attains a steady value. This occurs at $t^* \geq 6$.

3. Axial stress distribution along the axial direction behaves similar to temperature distribution along the axial direction, provided that stress gradient differs than the temperature gradient. The magnitude of radial stress component reduces as the depth from the surface increases towards the bulk of the substrate in the axial direction. As the heating progresses, the radial stress gradient $(\frac{\partial T^*}{\partial z^*})$ increases in the surface vicinity of the substrate material. The tangential stress component is compressive in the surface vicinity as the distance from the symmetry axis increases it becomes tensile. This is due to the temperature gradient $(\frac{\partial T^*}{\partial r^*})$ variation along the radial direction i.e. $(\frac{\partial T^*}{\partial r^*})$ is small in the region close to the symmetry axis and it becomes large as the distance from the symmetry axis increases further.

4. Equivalent stress shows a wavy behavior in the radial direction. This is because of the level of stress components in the radial direction, i.e. tangential stress component changes from compressive to tensile in the region $r^* \geq 1100$ while the

trend of the axial and radial stress component remains the same along the radial direction. The equivalent stress distribution in the axial direction is similar to the axial stress distribution. The equivalent stress rises rapidly in the early heating period and as the heating period progresses the rise of equivalent stress becomes steady with time, i.e. it becomes similar to the temporal variation of the temperature, provided that they have different magnitude of gradients.

6.2 Non-Conduction Limited Heating

In general, it is found that the constant and variable properties cases result in different surface temperature profiles In this case, the rate of surface temperature rise corresponding to constant properties is higher than its counterpart corresponding to variable properties. This, in turn, enhances the stress levels in this region. The depth of the cavity extends in the axial direction considerably while the cavity extension in the radial direction is limited with the size of the power intensity distribution across the substrate material surface. Two stress centers are generated inside the substrate material during the heating process, provided that the second stress center diminishes as the heating period progresses. The specific conclusions derived from the present study can be listed as follows:

1. The slope of temperature gradient changes across the initially melted region due to the mushy zone generated. The temperature gradient along the z-axis and corresponding to different heating periods are similar. This indicates that in a region below the absorption depth of the substrate material, diffusion is

the dominating mechanism and material response to diffusion is similar for all heating periods.

2. The tangential and radial stress components are compressive and the magnitude of stress level increases in the region close to the melt surface. However, tangential stress component in the radial direction becomes tensile beyond $r^* = 4200$. This is because of the zero stress component at the melt surface and the strain development due to thermal expansion in this region.

3. Equivalent stress has two peaks in the radial direction, provided that the magnitude of stress peak close to the melt surface is higher than that occurs some depth below the surface. As the heating period progresses, the magnitude of first peak increases while opposite is true for the second peak, i.e. the second stress center diminishes as the heating period progresses.

4. The equivalent stress behavior in the axial direction is similar to the radial stress component behavior in the axial direction, except the radial stress component is negative (compressive). The magnitude of equivalent stress peak in the radial direction remains same for all heating periods and the stress peak moves away from the melt surface as heating progresses.

Bibliography

[1] M.F. Modest and H. Abakians. Heat conduction in a moving semi-ininite solid subjected to pulsed laser irradiation. *Journal of Heat Transfer*, 108:597-601, 1986.

[2] B.F. Blackwell. Temperature profile in semi-infinite body with exponential source and convective boundary condition. *Journal of Heat Transfer*, 112:567-571, 1990.

[3] C. Maier, P. Schaaf and U. Gonser. Calculation of the temperature profile for laser treatment of metallic samples. *Materials Science and Engineering*, A150:271-280, 1992.

[4] T.Q. Qiu and C.L. Tien. Short-pulse laser heating on metals. *International Journal of Heat and Mass Transfer*, 35(3):719-726, 1992.

[5] S.M. Zubair and M.A. Chaudhry. Heat conduction in a semi-infinite solid when subjected to spatially decaying instantaneous laser source.*Warme – und Stoffubertragung*, 28:425-431, 1993.

[6] P. Ehrhard, C. Holle and C. Karcher. Temperature and penetration depth prediction for a three-dimensional field below a moving heat source. *International Journal of Heat and Mass Transfer*, 36(16):3997-4008, 1993.

[7] G.R.B.E. Romer and J. Meijer. Metal surface temperature induced by moving laser beams. *Optical and Quantum Electronics*, 27:1397-1406, 1995.

[8] M.A. Al-Nimr and S.A. Masoud. Nonequilibrium laser heating of metal films. *Journal of Heat Transfer*, 119:188-190, 1997.

[9] B.S. Yilbas and S.Z. Shuja. Heat transfer analysis of laser heated surfaces- conduction limited case. *Applied Surface Science*, 108:167-175, 1997.

[10] B.S. Yilbas, S.Z. Shuja and M. Sami. Thermal analysis of laser heat treated engineering alloys. *Surface Engineering*, 13(2):149-156, 1997.

[11] Z. Ji and S. Wu. FEM simulation of the temperature field during the laser forming of sheet metal. *Journal of Materials Processing Technology*, 74:89-95, 1998.

[12] S.Z. Shuja and B.S. Yilbas. Gas-assisted laser repetitive pulsed heating of a steel surface. *Proceedings of institution of Mechanical Engineers, Part C*, 212:741-757, 1998.

[13] L.M. Phinney and C.L. Tien. Electronic desorption of surface species using short-pulse lasers. *Journal of Heat Transfer*, 120:765-771, 1998.

[14] M.A. Al-Nimr, V.S. Arpaci. Picosecond thermal pulses in thin metal films. *Journal of Applied Physics*, 85(5):2517-2521, 1999.

[15] O. Manca, B. Morrone and S. Nardini. Thermal analysis of solid at high peclet numbers subjected to moving heat sources. *Journal of Heat Transfer*, 121:182-186, 1999.

[16] J.A. Ramos. Closed-form analytical solution to the temperature distribution inside a finite thickness body interacting with a moving Gaussian laser beam. *Lasers in Engineering*, 8:267-283, 1999.

[17] B.S. Yilbas and M. Sami. Three-dimensional kinetic theory approach for laser pulse heating. *Proceedings of institution of Mechanical Engineers, Part C*, 213:491-506, 1999.

[18] P.R.Woodard and J. Dryden. Thermal analysis of a lser pulse for discrete spot

surface transformation hardening. *Journal of Applied Physics*, 85(5):2488-2496, 1999.

[19] B.S. Yilbas and S.Z. Shuja. One-equation, two-equation and kinetic theory: Laser pulse heating. *Japanese Journal of Applied Physics, Part* 1, 39(7A):4018-4027, 2000.

[20] S.Z. Shuja and B.S. Yilbas. 3-dimensional conjugate heating of a moving slab. *Applied Surface Science*, 167:134-148, 2000.

[21] Nano-second laser pulse heating and assisting gas jet considerations. *International Journal of Machine Tools and Manufacture Design, Research and Application*, 40:1023-1038, 2000.

[22] S.Z. Shuja and B.S. Yilbas. The influence of gas jet velocity in laser heating- a moving workpiece case. *Proceedings of institution of Mechanical Engineers, Part C*, 214:1059-1078, 2000.

[23] B.S. Yilbas. Laser short-pulse heating: moving heat source and convective boundary considerations. *Physica A*, 293:157-177, 2001.

[24] B.S. Yilbas and M. Kalyon. Repetitive laser pulse heating with a convective boundary condition at the surface. *Journal of Physics D : Applied Physics*, 34:222-231, 2001.

[25] J.N. Gonsalves and W.W. Duley. Cutting thin metal sheets with the cw CO_2 laser. *Journal of Applied Physics*, 43(11):4684-4687, 1972.

[26] M.F. Modest and H. Abakians. Evaporative cutting of a semi-infinite body with moving CW laser. *Journal of Heat Transfer*, 108:602-607, 1986.

[27] B.S. Yilbas and Z. Yilbas. Some aspects of laser-metal vapor interaction. *Pramana – Journal of Physics*, 31(5):365-381, 1988.

[28] B.S. Yilbas, R. Davies, Z. Yilbas and A. Koc. Analysis of the absorption mecha-

nism during laser-metal interaction. *Pramana – Journal of Physics*, 34(6):473-489, 1990.

[29] P.S. Wie and J.Y. Ho. Energy considerations in high-energy beam drilling. *International Journal of Heat and Mass Transfer*, 33(10):2207-2217, 1990.

[30] S.Y. Bang and M.F. Modest. Multiple reflection effects on evaporative cutting witha moving CW laser. *Journal of Heat Transfer*, 113:663-669, 1991.

[31] S. Roy and M.F. Modest. CW laser machining of hard ceramics-I. Effects of three-dimensional conduction, variable properties and various laser parameters. *International Journal of Heat and Mass Transfer*, 36(14):3515-3528, 1993.

[32] S.Y. Bang, S. Roy and M.F. Modest. CW laser machining of hard ceramics-II. Effects of multiple reflections. *International Journal of Heat and Mass Transfer*, 36(14):3529-3540, 1993.

[33] W. Schulz, D. Becker, J. Franke, R. KJemmerling and G. Harziger. Heat conduction losses in laser cutting of metals. *Jornal of Physics D : Applied Physics*, 26:1357-1363, 1993.

[34] B.S. Yilbas and A.Z. Sahin. Turbulent boundary layer approach allowing chemical reactions for CO_2 laser oxygen-assisted cutting process. *Proceedings of institution of Mechanical Engineers, Part C*, 208:275-284, 1994.

[35] B.S. Yilbas, A.Z. Sahin and R. Davies. Laser heating mechanism including evaporation process initiating laser drilling. *International Journal of Machine Tools and Manufacture Design, Research and Application*, 35(7):1047-1062, 1995.

[36] B.S. Yilbas and A.Z. Sahin. Oxygen assisted laser cutting mechanism- a laminar boundary layer approach including the combustion process. *Optics and Laser Technology*, 27(3):175-184, 1995.

[37] B.S. Yilbas and A.Z. Al-Garni. Some aspect of laser heatig of engineering materials. *Journal of Lase Applications*, 8:197-204, 1996.

[38] B.S. Yilbas. Experimental investigation into CO_2 laser cutting parameters. *Journal of Materials Processing Technology*, 58:323-330, 1996.

[39] M.F. Modest. Three-dimensional, transient model for laser machining of ablating/decomposing materials. *International Journal of Heat and Mass Transfer*, 39(2):221-234, 1996.

[40] Y.V. Afanasiev, V.A. Isakov, I.N. Zavestovskaya, B.N. Chichkov, F. von Alvensleben and H. Welling. Hydrodynamic regimes of UV laser ablation of polymers. *Applied Physics A : Materials Science and Processing*, 64:561-572, 1997.

[41] V. Semak and A. Matsunawa. The role of recoil pressure in energy balance during laser materials processing. *Journal of Physics D : Applied Physics*, 30:2541-2552, 1997.

[42] X. Liu, D. Du and G. Mourou. Laser ablation and micromachining with ultrshort laser pulses. *IEEE Journal of Quantum Electronics*, 33(10):1706-1716, 1997.

[43] W. Pecharapa and A. Kar. Effects of phase changes on weld pool shape in laser welding. *Journal of Physics D : Applied Physics*, 30:3322-3329, 1997.

[44] G. Tahmouch, P. Meyrueis and P. Grandjean. Cutting by a high power laser at a long distance without an assist gas for dismantling. *Optics and Laser Technology*, 29(6):307-316, 1997.

[45] B.S. Yilbas. The analysis of CO2 laser cutting. *Proceedings of institution of Mechanical Engineers, Part B*, 211:223-232, 1997.

[46] A. Kar, J.A. Rothenflue and W.P. Latham. Scaling laws for thick-section cutting with a chemical oxygen-iodine laser. *Journal of Laser Applications*, 9:279-286, 1997.

[47] R. Aloke, V. Girish, R.F. Scrutton and P.A. Molian. A model for prediction of dimensional tolerances of laser cut holes in mild steel thin plates. *International Journal of Machine Tools and Manufacture Design, Research and Application*, 37(8):1069-1078, 1997.

[48] R.K. Ganesh and A. Faghri. A generalized thermal modeling of laser drilling process-I. Mathematical modeling and numerical methodology. *International Journal of Heat and Mass Transfer*, 40(14):3351-3360, 1997.

[49] R.K. Ganesh, A. Faghri and Y. Hahn. A generalized thermal modeling for laser drilling process-II. Numerical simulation and results. *International Journal of Heat and Mass Transfer*, 40(14):3361-3373, 1997.

[50] C.L. Liu, J.N. Leboeuf, R.F. Wood, D.B. Geobegan, J.M. Donato, K.R. Chen and A.A. Puretzky. Computational modeling of physical processes during laser ablation. *Materials Science and Engineering B*, 47:70-77, 1997.

[51] M.F. Modest. Laser throug-cutting and drilling models for ablating/decomposing materials. *Journal of Laser Applications*, 9:137-145, 1997.

[52] I. Black, S.A.J. Livingstone and K.L. Chua. A laser beam machining (LBM) database for the cutting of ceramic tile. *Journal of Materials Processing Technology*, 84:47-55, 1998.

[53] Shang-Liang Chen. The effects of gas composition on the CO_2 laser cutting of mild steel. *Journal of Materials Processing Technology*, 73:147-159, 1998.

[54] B.S. Yilas, M. Sami and H.I. AbuAlHamayel. 3-dimensional modeling of laser repetitive pulse heating: a phase change and a moving heat source considerations. *Applied Surface Science*, 134:159-178, 1998.

[55] B.S. Yilbas. Particle ejection during laser drilling of engineering metals. *Lasers in Engineering*, 7:57-67, 1998.

[56] Y. Zhang and A. Faghri. Vaporization, melting and heat conduction in the laser drilling process. *International Journal of Heat and Mass Transfer*, 42:1775-1790, 1999.

[57] P. Solana, P. Kapadia, J.M. Dowden and P.J. Marsden. An analytical model for the laser drilling of metals with absorption within the vapour. *Journal of Physics D : Applied Physics*, 32:942-952, 1999.

[58] B.S. Yilbas. Effect of process parameters on the kerf width during the laser cutting proess. *Proceedings of institution of Mechanical Engineers, Part B*, 215: , 2001.

[59] J. Kroos, U. Gratzke, M. Vicanek and G. Simon. Dynamic behaviour of the key hole in laser welding. *Journal of Physics D : Applied Physics*, 26:481-486, 1993.

[60] A. Matsunawa and V. Semak. The simulation of front keyhole wall dynamics during laser welding. *Journal of Physics D : Applied Physics*, 30:798-809, 1997.

[61] A.A. Rostami and A. Raisi. Temperature distribution and melt pool size in a semi-infinite body due to a moving laser heat source. *Numerical Heat Transfer, Part A*, 31:783-796, 1997.

[62] P. Solana and J.L. Ocana. A mathematical model for penetration laser welding as a free-boundary problem. *Journal of Physics D : Applied Physics*, 30:1300-1313, 1997.

[63] W.S. Kim and B.C. Sim. Study of thermalbehavior and fluid flow during laser surface heating of alloys. *Numerical Heat Transfer, Part A*, 31:703-723, 1997.

[64] U.C. Paek and F.P. Gagliano. Thermal analysis of laser drilling processes. *IEEE Journal of Quantum Electronics*, 8(2):112-119, 1972.

[65] H. Arnet and F. Vollersten. Extending laser bending for the generation of convex shapes. *Proceedings of institution of Mechanical Engineers, Part B*, 209:433-442, 1995.

[66] K. Li and P. Sheng. Plane stress model for fracture of ceramics during laser cutting. *International Journal of Machine Tools and Manufacture Design, Research and Application*, 35(11):1493-1506, 1995.

[67] T. Elperin and G. Rudin. Thermoelasticity problem for a multilayer coating-

substrate assembly irradiated by a laser beam. *International Communications of Heat and Mass Transfer*, 23(1):133-142, 1996.

[68] H.G. Wang, Y.H. Guan, T.L. Chen and J.T. Zhang. A study of thermal stresses during laser quenching. *Journal of Materials Processing Technology*, 63:550-553, 1997.

[69] C.L. Yau, K.C. Chan and W.B. Lee. Laser bending of leadframe materials. *Journal of Materials Processing Technology*, 82:117-121, 1998.

[70] B.S. Yilbas, M. Sami and S.Z. Shuja. Laser-induced thermal stresses on steel surface. *Optics and Lasers in Engineering*, 30:25-37, 1998.

[71] Y. Dain, P.D. Kapadia and J.M. Dowden. The distortion gap width and stresses in laser welding of thin elastic plates. *Journal of Physics D : Applied Physics*, 32:168-175, 1999.

[72] A.F.M. Arif, S.Z. Shuja and B.S. Yilbas. Gas-Assisted laser single-pulse heating: study of thermal stresses. *Proceedings of institution of Mechanical Engineers, Part C*, 215:291-306, 2001.

[73] B.S. Yilbas and S.Z. Shuja. Laser short-pulse heating of surfaces. *Journal of Physics D : Applied Physics*, 32:1947-1954, 1999.

[74] M.N. Ozisik. Heat Conduction, 2nd ed., John Wiley and Sons, 392-430, New York, 1993.

[75] S.P. Timenshenko and J.N. Goodier. Theory of Elasticity, 3rd ed., 476-484, McGraw-Hill Book Comp., Singapore, 1984.

[76] J.C. Strikwerda. Finite difference Schemes and Partial Differential Equations, Wardsworth & Brooks/Cole, 1989.

[77] S.V. Patankar. Numerical Heat Transfer and Fluid Flow, Hemisphere Publishing Corp., 1980.

[78] B.S. Yilbas, M. Sami and A. Al-Farayedhi. Closed-form and numerical solutions to the laser heating process. *Proceedings of institution of Mechanical Engineers, Part C*, 212:141-151, 1998.

VITA

Iftekhar Zaheer Naqavi		
B.E	1998	N.E.D University of Engineering & Technology
M.S	2001	King Fahd University of Petroleum & Minerals